# SYSTEMS PATHOLOGY: A BOTTOM-UP APPROACH FOR UNDERSTANDING FIBROBLAST-EPITHELIAL INTERACTIONS IN BREAST CANCER

BY

SARAH ELIZABETH HOLTON

DISSERTATION

Submitted in partial fulfillment of the requirements
for the degree of Doctor of Philosophy in Bioengineering
in the Graduate College of the
University of Illinois at Urbana-Champaign, 2013

Urbana, Illinois

Doctoral Committee:

Professor Rohit Bhargava, Chair
Professor Andre Kajdaçsy-Balla
Professor Benita S. Katzenellenbogen
Assistant Professor Jian Ma
Assistant Professor Kannanganattu V. Prasanth

**Abstract**

Breast cancer is prevalent both in the United States and worldwide. While both screening tests and targeted therapies are available, there are still challenges in the diagnosis, prognosis, and treatment of breast cancer. We were motivated to develop a new approach for both studying the etiology of heterogeneity in breast cancer phenotypes and predicting the course of disease in tumor biopsies using an emerging chemical imaging technology.

It has been described extensively that the tumor microenvironment, or stroma, can promote or suppress cancer phenotypes in many tissues. We hypothesized that interaction with fibroblasts, the predominant cell type found in the breast tumor stroma, is a critical regulatory step in the progression of breast cancer from confined to invasive disease. Hence, we developed a novel three-dimensional co-culture model to investigate this interaction. The development and validation of this model is described in chapter two. We used it first to determine how cancerous molecular signatures can propagate from cancerous to normal epithelium through the activation of fibroblasts. Changes in the architectural morphology of normal mammary acini were used as a metric to determine cancer progression, in addition to gene expression analysis and cell-based assays such as proliferation and migration assays. This system is a robust and easily applied tool for investigating fibroblast-epithelial communication in a physiologically-relevant context.

The 3D co-culture system was used to investigate how fibroblasts impact the growth of estrogen receptor-positive ($ER^+$) breast cancer cells and this is described in chapter three. $ER^+$ is the most common subtype of breast cancer (>75%) and while these patients are eligible to receive targeted endocrine therapies, up to 30% of patients will experience a recurrence. Others will fail to respond to front-line endocrine therapies, while more patients will become resistant to endocrine therapies over time. We aimed to understand how fibroblasts play a role in the progression from hormone-dependent to hormone-independent growth. The cell culture data was translated to patient samples using bioinformatics approaches and label-free chemical imaging. Further, we define one aspect of the interaction between breast cancer cells and fibroblasts through identifying secreted proteins that are involved in the stromal-epithelial communication. The 43-protein signature can be used to classify breast cancer patients based on their corresponding gene expression profile, and we found that the signature is significantly upregulated in patients with more invasive disease.

In order to continue translating our results from cell culture to patient samples, we describe the application of label-free Fourier transform infrared spectroscopic imaging to monitoring breast cancer cell phenotypes. Chapter four details how biological changes can be spatially resolved in heterogeneous samples while in chapter five an approach to determine estrogen receptor presence and function in cell culture samples and patient biopsies is discussed. We show how FT-IR imaging can be used to define label-free spectroscopic signatures that are consistent between cell culture and patients, and explore how this approach may be used in the future to add additional information to current pathology practice.

We have developed a method to both understand the molecular mechanisms involved in how the microenvironment regulates early breast cancer phenotypes and to detect altered cellular phenotypes using label-free FT-IR imaging. We aim to apply this systems pathology approach to the development of novel diagnostic and prognostic signatures for determining the trajectory of cancer progression at very early stages.

**Acknowledgements**

I would like to thank my parents and family for their unconditional support and love. Their tenacity, work ethic, and passion for everything they do will always be an inspiration to me.

Thank you to my friends always for thoughtful discussion, commiseration, and all the fun times we shared. You are, and always will be, a part of my family.

Very warm regards to my fellow researchers, both those within my research group and those I shared a bench with elsewhere. Brought together by science, we depart as close friends and colleagues. Special thanks to Professor Michael Walsh and Dr. Anna Bergamaschi for volunteering countless hours to my training.

Thank you to the Medical Scholars Program, the Department of Bioengineering, the College of Medicine, the Midwest Cancer Nanotechnology Center Training Grant, and the Beckman Institute for financial and administrative support.

Thank you to my advisor, for never doubting me, even when I doubted myself, for supporting me and letting me explore with very few bounds, and for frequent and thoughtful discussion.

Thank you also to my doctoral committee, for thoughtful guidance, constant support, and provocative discussion.

**TABLE OF CONTENTS**

CHAPTER ONE: INTRODUCTION ..... 1

CHAPTER TWO: THREE-DIMENSIONAL CELL CULTURE MODELS FOR STUDYING THE EFFECT OF FIBROBLASTS ON BREAST CANCER PHENOTYPES ..... 15

CHAPTER THREE: INTEGRATING MOLECULAR PROFILING AND CHEMICAL IMAGING TO UNDERSTAND HETEROTYPIC INTERACTIONS IN COMPLEX SAMPLES ..... 43

CHAPTER FOUR: DESCRIBING LABEL-FREE CHEMICAL SIGNATURES OF 3D BREAST CELL CULTURES USING FT-IR IMAGING ..... 74

CHAPTER FIVE: SPECTROSCOPIC SIGNATURE OF ERα PRESENCE, LOCALIZATION, AND FUNCTION IN BREAST CANCER CELLS ..... 104

CHAPTER SIX: SUMMARY, IMPLICATIONS, AND FUTURE DIRECTIONS ..... 123

## CHAPTER ONE: INTRODUCTION

*Motivation and Impact*

We recently passed the 40th year in the war against cancer. While breast cancer incidence and deaths have declined over the last decade in the United States, breast cancer remains the most common cancer site among women and the second leading cause of cancer-related death (1). Disease is increasingly being detected early in some populations, while screening fails to identify the most lethal subtypes of breast cancer that are more likely to be found in certain groups (African Americans, Hispanics, and women under the age of 50). In this emerging era of big data, novel diagnostic and prognostic markers are being evaluated for their efficacy in improving understanding of disease progression and providing opportunities for therapeutic intervention. Recently, the National Cancer Institute assembled a list of 24 provocative questions from the research community to focus the efforts of researchers on those ideas that have the greatest potential impact on patients. These questions were divided into four themes, one of which is tumor detection, diagnosis, and prognosis. The questions in this theme are (2):

1. *Can we determine why some tumors evolve to aggressive malignancy after years of indolence?*
2. *How can the physical properties of tumors, such as a cell's electrical, optical, or mechanical properties, be used to provide earlier or more reliable cancer detection, diagnosis, prognosis, or monitoring of drug response or tumor recurrence?*
3. *Are there definable properties of pre-malignant or other non-invasive lesions that predict the likelihood of progression to metastatic disease?*
4. *What molecular events establish tumor dormancy after treatment and what leads to recurrence?*

These questions summarize the motivation for our efforts. In this work, information is integrated from both molecular and optical approaches to investigate the progression of breast cancer from confined to invasive disease. Specifically, the ways in which fibroblasts, the predominant cell type found in the tumor microenvironment of the breast, alter breast cancer phenotypes is investigated. Further, label-

free spectroscopic signatures of cancerous phenotypes are described. We define this as a systems pathology approach for understanding cancer progression, in an effort to develop novel diagnostic and prognostic tools based on an understanding of the mechanism coupled with physical properties of cancer cells and tissues.

*Breast cancer prevalence and current clinical challenges*

Breast cancer is the second most common cancer site in women and carries an estimated 1 in 8 lifetime risk. It is estimated that 234,580 new cases of invasive breast cancer will be diagnosed and 40,030 men and women will die from the disease in the United States in 2013 (1). Further, while overall incidence of confined tumors has stabilized over the last decade, diagnosis of ductal carcinoma *in situ* (DCIS) is increasing in younger women, with approximately 57,650 cases diagnosed in 2011 (1). Although the overall five-year survival rate is 89% across all stages of disease, the relative survival rates are 99% for localized disease, 84% for regional disease (in which one or more lymph nodes is affected), and 23% for distant-stage disease (3). While cancer is increasingly being detected and treated at an early stage, there is a population of patients who do not respond to first-line therapies, and when their cancer recurs, it is often more invasive and resistant to therapy (4).

Molecular targeted therapies have shown clinical promise. The majority of breast cancers diagnosed are estrogen receptor positive ($ER^+$) (5). These tumors are associated with favorable prognosis because the presence of estrogen receptor α (ERα) and/or Progesterone receptor (PR) predicts a good response to endocrine therapy such as selective estrogen receptor modulators (SERMs) and aromatase inhibitors (AIs). However, because patients with the equivalent tumor stage and receptor status can have different responses to the same therapy (6), molecular subtyping by gene expression signatures in clinical samples and human breast cancer cell lines (7,8) has recently emerged as an exciting approach for determining personalized therapies. One clinical success story, Trastuzumab (Herceptin) is a monoclonal antibody that targets the HER-2/*neu* protein that is upregulated in 15-30% of breast tumors. Although molecular subtyping may improve targeted therapies, it is unclear what causes tumors to recur after treatments. Up to 30% of patients placed on endocrine therapy will experience a recurrence (9). It would be advantageous to understand molecular interactions at the time of first biopsy in order to guide breast cancer treatment.

*The microenvironment is a regulator of cancer phenotypes*

Cells are very sensitive to chemical and mechanical changes in their microenvironment, which can provide cues for developmental and other intracellular programs (10,11). Culturing epithelial cells in three-dimensional (3D) matrices leads to differential expression and localization of cell receptors (12). Gene expression profiling of breast cancer cell lines grown in 3D shows that this type of culture condition is more relevant for translating results to clinical samples (13). Similarly, tumor cells interact with the local microenvironment in what is now known to be a key regulatory step for cancer progression. Seminal work in this field has shown that cancerous phenotypes can be stimulated (14-16) or suppressed (17-19) simply by altering the tumor microenvironment. The tumor microenvironment, or stroma, in ductal carcinoma consists of extracellular matrix proteins (primarily fibrillar collagen) and a variety of cells including fibroblasts and macrophages. Cancer-activated stroma, characterized by the presence of cancer-activated fibroblasts (CAFs) that express α-smooth muscle (α-SMA) protein, is associated with poor prognosis in breast cancer (20-22). Although the heterotypic interactions between fibroblasts, extracellular matrix, and cancerous epithelial cells are being studied by our group and others, it is unclear how the sum of these interactions determines the tumor outcome.

While many stromal cell types have been implicated in disrupting tissue homeostasis and tumor progression, including immune cells, supporting cells, cells of the vasculature, and mesenchymal stem cells, we focused on the role of fibroblasts in particular. Fibroblasts maintain normal tissue homeostasis in many organs (23-24). Because of their important role in regulating breast epithelium during differentiation (25), we hypothesized that fibroblasts influence epithelial proliferation and invasion during the early stages of cancer progression. Specifically, the paracrine signaling that occurs between epithelial cells and fibroblasts was investigated, as this has the potential to provide novel therapeutic targets as well as an understanding of the basic mechanisms that drive tumor progression from confined to invasive disease.

Many three-dimensional culture models have been described to study breast cancer (26-30). Co-cultures have also been reported to study the interaction of cancer cells with fibroblasts (31,32), cancer-associated fibroblasts (33-35), macrophages (36), adipocytes (37), and normal epithelial cells (38). We combined a 3D model with both epithelial and stromal components in which the cells were grown in a

physiologically-representative context. Epithelial cells were grown in a recombinant basement membrane (Matrigel) model to support normal epithelial architecture (30). Nontumorigenic and normal epithelial cells formed growth-arrested acinar structures with established lumens while cancer cells formed spheroid structures without lumens. Fibroblasts were grown dispersed within type I collagen gels. These methods and the characterization of this 3D model are described in Chapter 2.

*Defining predictive signatures of breast cancer progression*

Many signatures of breast cancer have been reported that correlate expression levels of genes, proteins, or microRNAs in cells and tissues to patient outcome (39-44). However, only a few of these signatures have led to clinical utility, most notably the van't Veer 70-gene prognostic signature that led to the MammaPrint test (45,46), the Oncotype Dx system (47,48), and the PAM50 score (49-51). Although it is established that tumors are heterogeneous, the majority of molecular signatures defined in the literature are based on approaches that take the average expression of hundreds to thousands of cells. Hence, the true molecular portrait of the tumor is not described because contributions of various phenotypes are averaged. Further, recent reports have shown that the gene expression in the tumor stroma also has prognostic significance (43,44). These findings suggest that an approach that combines the spatial localization of immunohistochemistry, the computational approaches of gene signature classification, and the molecular mechanistic understanding of *in vitro* experiments would be an ideal diagnostic/prognostic strategy. We explore the use of such a strategy here, using three-dimensional models of breast cancer progression and Fourier transform infrared (FT-IR) spectroscopic imaging with an emphasis on the study of the behavior of $ER^+$ cancers.

*Fourier transform infrared spectroscopic imaging can be used to define label-free chemical signatures of disease progression*

We employed an emerging technology to translate results from cell culture to patient tissue specimens. Fourier transform infrared (FT-IR) spectroscopic imaging can be used to describe label-free molecular signatures of cellular transformation. FT-IR measures the absorption of energy by molecular bonds at characteristic wavelengths and can be used to quantify the relative amounts and distributions of chemical bonds present within a sample (52,53). Infrared radiation cannot be seen with the human

eye and consists of wavelengths between 0.7 and 300 μm. Wavelengths in the mid-infrared region, used for this work, are 2-14 μm (52). Many biomolecules of interest can be detected in this regime.

We and others have correlated cellular transformations with spectroscopic signatures. Our previous work shows that the activation of fibroblasts to myofibroblasts after treatment with TGF-β or co-culture with cancer cells can be monitored using IR imaging (54,55). Our lab has also shown that melanoma progression can be characterized in an engineered model of skin by studying the stromal changes around the cancer cell (56). We have demonstrated that chemical imaging is a powerful tool for studying biological phenomena at the bench and that these results can be translated to human tissue. Through the development of computational algorithms, we are able to classify cell types in patient biopsy specimens based on their spectroscopic profiles. Importantly, the sample processing for IR imaging is minimal. Formalin fixed and paraffin embedded (FFPE) tissues can be used and no stains are required. FT-IR imaging may be easily worked in with the current clinical workflow, providing additional information to the pathologist about the tissue characteristics.

A schematic of an FT-IR imaging instrument is shown in Figure 1.1 (57). Briefly, a heated filament infrared source is used and the energy is passed through a Michelson interferometer. This energy is broadband, consisting of all of the wavelengths to be measured. The energy is then directed through a microscope objective, where it interacts with the sample of interest. In a transmission measurement, the energy passes completely through both the sample and the substrate before it is detected. In a reflection measurement, as was used primarily in this work, the energy passes through the sample and is mostly reflected off of the substrate before passing through the sample again. The energy is detected with a liquid nitrogen-cooled mercury cadmium telluride (MCT) detector. Interaction with the sample has altered the characteristics of the energy, and this can be analyzed with a Fourier transform, which converts the absorption as a function of the position of the mirror in the interferometer to the absorption of each wavelength. Because molecular bonds vibrate at characteristic wavelengths, information about the quality of the sample can be assessed. In FT-IR imaging, the sample is placed on an x-y-z microscope stage and the absorption at each wavelength is measured for each pixel. The pixel size for both transmission and reflection modes is 6.25 μm x 6.25 μm, sufficient for looking at individual cells. Another mode used in this work is attenuated total reflectance (ATR) FT-IR imaging. This mode places a crystal made of a high refractive index material, in this case Germanium (refractive index = 4), directly in contact with the sample. The crystal acts as a solid immersion lens. This results in a four-fold

improvement of spatial resolution, reducing the pixel size to 1.56 x 1.56 μm. The signal-to-noise ratio is also improved because all of the light from the sample is directed back into the instrument and there are less optical aberrations due to scattering (58). The limitations of this mode are that contact from the crystal can be damaging to the sample and the total scanning area is limited by the size of the crystal (usually 500 μm x 500 μm to 1 mm x 1 mm).

With either mode, the resulting dataset is three-dimensional. Each pixel in the image represents the chemical spectrum of the corresponding sample area. A characteristic FT-IR spectrum is shown in Figure 1.2 and an example of an image is shown in Figure 1.3. The image is the distribution of the absorbance values for a particular peak. The peak shown in Figure 1.3 is 2960 $cm^{-1}$, which corresponds to the asymmetric vibrational mode of $CH_3$ stretching, associated with phospholipids, fatty acids, and triglycerides, and can be used as a marker of metabolism (56,59). Other peak assignments and their corresponding biomolecule signatures are described in Table 1.1. Using FT-IR imaging, the chemical nature of complex samples can be described with a spatial resolution that can identify subcellular changes. The investigation of FT-IR imaging as a tool to describe hormone response in cells and tissues is described in Chapters 3 and 4. We also correlate spectroscopic signatures with the expression, localization, and function of the ERα protein, a significant prognostic marker for breast cancer in Chapter 5.

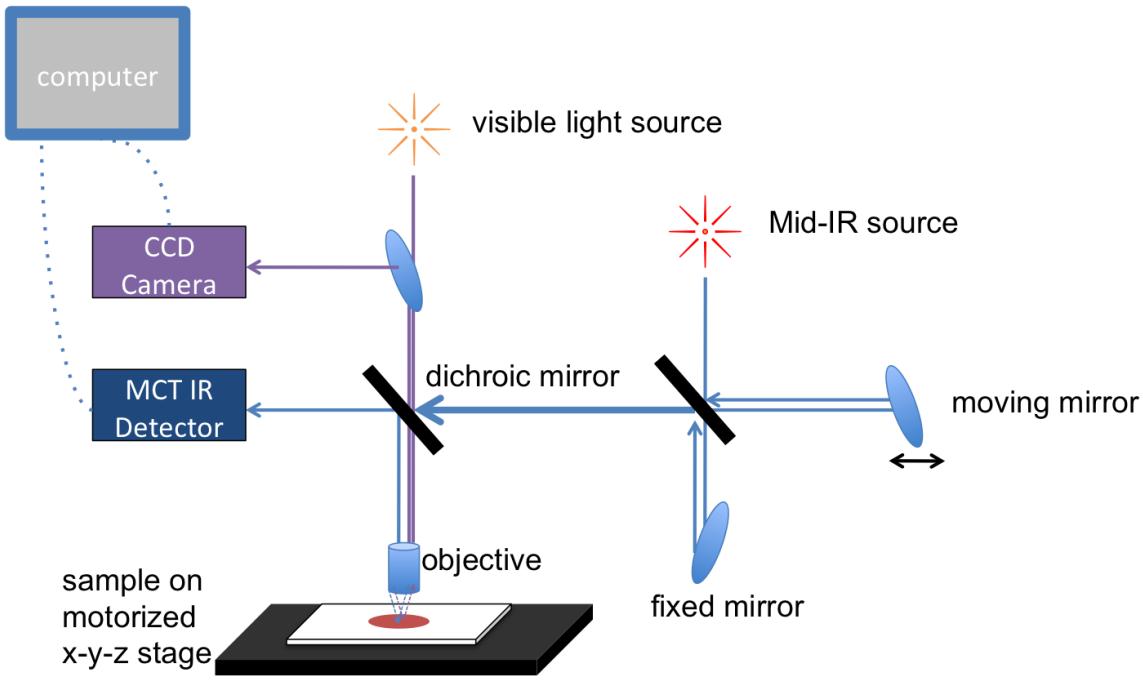


**Figure 1.1: Schematic of FT-IR imaging instrument used for this work.** Used with permission (57).

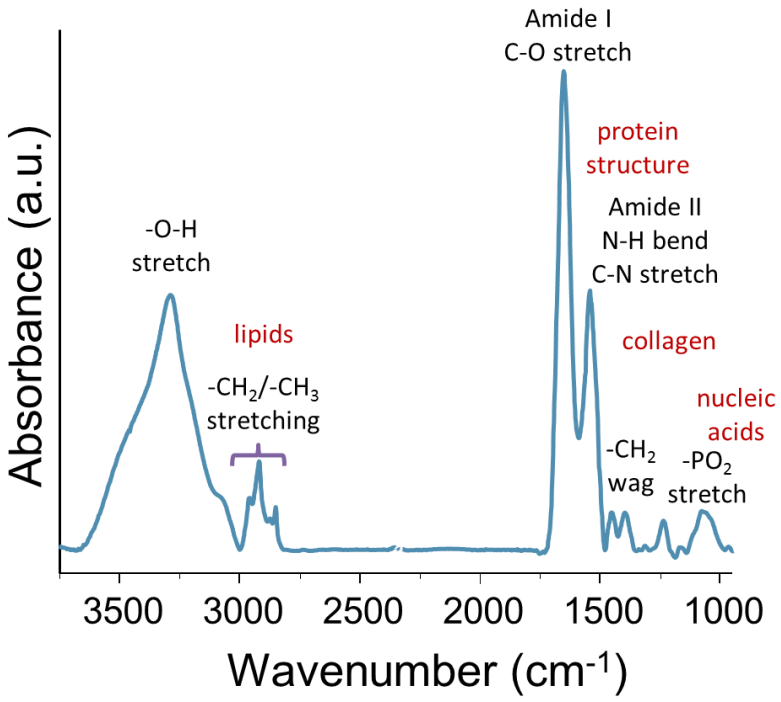


**Figure 1.2: Characteristic FT-IR absorbance spectrum with labeled peaks of interest.**

**Table 1.1: Bond assignments for peaks commonly used in biological studies.** Adapted from (56).

| Wavenumber ($cm^{-1}$) | Bond Assignment | Biomolecule Assignment | Reference |
|---|---|---|---|
| 3550-3000 | -OH | Water | (60,61) |
| 2960 | Asymmetric $CH_3$ stretching | Fatty acid (Saturated) | (61-63) |
| 2930 | Asymmetric $CH_2$ stretching | Fatty acid (Saturated) | (61-63) |
| 2870 | Symmetric $CH_3$ stretching | Fatty acid | (61-63) |
| 2850 | Symmetric $CH_2$ stretching | Fatty acid (Saturated) | (61-63) |
| 1656 | Amide I (80% C-O stretching) | Protein | (61) |
| 1550 | Amide II (60% N-H bending, 40% C-N stretching) | Protein | (61) |
| 1400 | C-O stretch of $COO^-$ | Fatty acid | (61) |
| 1284, 1240, 1203 | Amide III (40% C-N stretching, 30% N-H bending, 20% methyl stretching) | Collagen | (64) |
| 1224 | Asymmetric $PO_2^-$ stretching | nucleic acids, phospholipids | (61-63) |
| 1170 | C-O asymmetric stretching | esters | (61) |
| 1080 | Symmetric $PO_2^-$ stretching | nucleic acids, phospholipids | (61-63) |

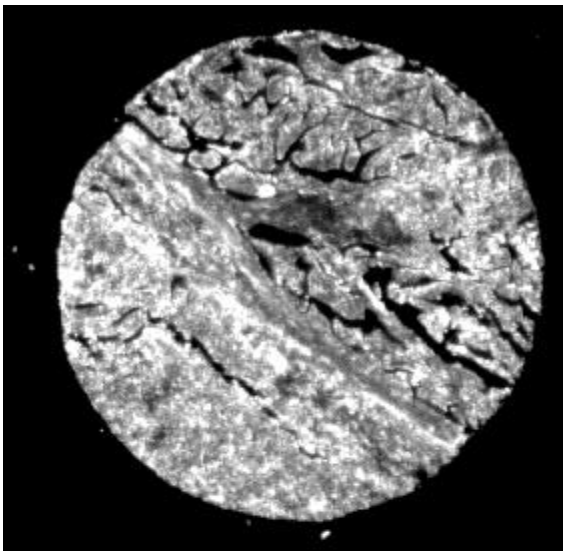

**Figure 1.3: Image of a 1.5 mm breast tissue core at 2960 $cm^{-1}$, showing distribution of -$CH_3$ bonds, corresponding to fatty acids.**

*Summary*

We were motivated to determine which factors determine the course of early breast cancer progression and hypothesized that interactions with the microenvironment, and in particular fibroblasts, are key regulators of cancerous phenotypes. Our model of tumor growth is based on a constantly evolving landscape that involves factors at many levels of regulation, length scales, and time scales. Here, we discuss the approaches and tools that can be used to study early fibroblast-tumor interactions. In particular, we describe how the microenvironment can alter breast cancer cell phenotypes from a systems pathology perspective – integrating molecular profiling with chemical imaging from cells to tissues.

**References**

1. U.S. Cancer Statistics Working Group. *United States Cancer Statistics: 1999-2009 Incidence and Mortality Web-based Report.* Atlanta (GA): Department of Health and Human Services, Centers for Disease Control and Prevention, and National Cancer Institute; 2013. Available at http://www.cdc.gov/uscs.
2. NIH National Cancer Institute. *Provocative Questions Initiative*, 2013. Web. 15 March 2013.
3. Breen N., Gentleman J.F., Schiller J.S. (2011) Update on mammography trends: comparisons of rates in 2000, 2005, and 2008. *Cancer* 117(10): 2209-2218.

4. DeSantis C., Siegel R., Jemal A., eds. (2011) Breast Cancer Facts and Figures 2011-2012. American Cancer Society, Inc.
5. Paik S., *et al*. (2004) A multigene assay to predict recurrence of tamoxifen-treated, node-negative breast cancer. *N Engl J Med* 351: 2817-2826.
6. Gonzalez-Angulo A.M., Morales-Vasquez F., Hortobaqyi G.N. (2007) Overview of resistance to systemic therapy in patients with breast cancer. *Adv Exp Med Biol* 608: 1-22.
7. Perou C.M., *et al*. (2000) Molecular portraits of human breast tumors. *Nature* 406: 747-752.
8. Barretina J., *et al.* (2012) The Cancer Cell Line Encyclopedia enables predictive modeling of anticancer drug sensitivity. *Nature* 483: 603-607.
9. Early Breast Cancer Triallists' Collaborative Group. (2005) Effects of chemotherapy and hormonal therapy for early breast cancer on recurrence and 15-year survival: an overview of the randomized trials. *Lancet* 365: 1687-1717.
10. Engler A.J., *et al*. (2006) Matrix elasticity directs stem cell lineage specification. *Cell* 126(4): 677-689.
11. Paszek M.J., *et al*. (2005) Tensional homeostasis and the malignant phenotype. *Cancer Cell* 8: 241-254.
12. Birgersdotter A., Sandberg R., and Ernberg I. (2005) Gene expression perturbation in vitro – A growing case for three-dimensional (3D) culture systems. *Semin Cancer Biol* **15**(5): 405-412.
13. Martin K.J., Patrick D.R., Bissell M.J., and Fournier M.V. (2008) Prognostic breast cancer signature identified from 3D culture model accurately predicts clinical outcome across independent datasets. *PLoS ONE* **3**(8): e2994.
14. Barcellos-Hoff M.H., Ravani S.A. (2000) Irradiated mammary gland stroma promotes the expression of tumorigenic potential by unirradiated epithelial cells. *Cancer Res* 60: 1254-1260.
15. Olumi A. *et al.* (1999) Carcinoma-associated fibroblasts direct tumor progression of initiated human prostate epithelium. *Cancer Res* 59:002-5011.
16. Hwang R.F., *et al*. (2008) Cancer-associated stromal fibroblasts promote pancreatic tumor progression. *Cancer Res* 68:918-926.
17. Mintz B., Illmensee K. (1975) Normal genetically mosaic mice produced from malignant teratocarcinoma cells. *Proc Natl Acad Sci USA* 72(9): 3585-3589.
18. Dolberg D.S., Bissell M.J. (1984) Inability of Rous sarcoma virus to cause sarcomas in the avian embryo. *Nature* 309: 552-556.
19. Weaver, V.M., *et al*. (1997) Reversion of the malignant phenotype of human breast cells in three-dimensional culture and *in vivo* by integrin blocking antibodies. *J Cell Biol* 137: 231-245.

20. Orimo A. and Weinberg R.A. (2006) Stromal fibroblasts in cancer: A novel tumor-promoting cell type. *Cell Cycle* **5**(15): 1597-1601
21. Liao D., *et al*. (2009) Cancer associated fibroblasts promote tumor growth and metastasis by modulating the tumor immune microenvironment in a 4T1 murine breast cancer model. *PLoS One* **4**(11): e7965.
22. Mercier I., *et al*. (2008) Human breast cancer-associated fibroblasts (CAFs) show caveolin-1 down-regulation and RB tumor suppressor functional inactivation: Implications for the response to hormonal therapy. *Cancer Biol Ther* **7**(8): 1212-1225.
23. Weigelt B. and Bissell M.J. (2008) Unraveling the microenvironmental influences on the normal mammary gland and breast cancer. *Semin Cancer Biol* **18**(5): 311-321.
24. Chiquet M., *et al*. (2003) How do fibroblasts translate mechanical signals into changes in extracellular matrix production? *Matrix Biol* **22**(1): 73-80.
25. Shekhar M.P.V., *et al*. (2001) Breast stroma plays a dominant regulatory role in breast epithelial growth and differentiation: Implications for tumor development and progression. *Cancer Res* **61**: 1320-1326.
26. Kaur P., *et al.* (2011) Human breast cancer histoid: an in vitro 3-dimensional co-culture model that mimics breast cancer tissue. *J Histochem Cytochem* **59**(12): 1087-1100.
27. Lee G.Y., Kenny P.A., Lee E.H., and Bissell M.J. (2007) Three-dimensional culture models of normal and malignant breast epithelial cells. *Nature Methods* **4**(4): 359-365.
28. Nelson, C.M. and Bissell M.J. (2005) Modeling dynamic reciprocity: Engineering three-dimensional culture models of breast architecture, function, and neoplastic transformation. *Semin Cancer Biol* **15**(5): 342-352.
29. Shaw K.R.M., Wrobel C.N., and Brugge J.S. (2004) Use of three-dimensional basement membrane cultures to model oncogene-induced changes in mammary epithelial morphogenesis. *J Mammary Gland Biol Neoplasia* **9**(4): 297-310.
30. Debnath J., Muthuswamy S.K., and Brugge J.S. (2003) Morphogenesis and oncogenesis of MCF-10A mammary epithelial acini grown in three-dimensional basement membrane cultures. *Methods* **30**(3): 256-268.
31. Okochi M., Matsumura T., and Honda H. (2013) Magnetic force-based cell patterning for evaluation of the effect of stromal fibroblasts on invasive capacity in 3D cultures. *Biosens Bioelectron* **42**: 300-307.

32. Chhetri R.K., Philips Z.F., Troester M.A., and Oldenburg A.L. (2012) Longitudinal study of mammary epithelial and fibroblast co-cultures using optical coherence tomography reveals morphological hallmarks of pre-malignancy. *PLoS One* **7**(11): e49148.
33. Su G., Sung K.E., Beebe D.J., and Friedl A. (2012) Functional screen of paracrine signals in breast carcinoma fibroblasts. *PloS One* **7**(10: e46685.
34. Sadlonova A., *et al*. (2005) Breast fibroblasts modulate epithelial cell proliferation in three-dimensional in vitro co-culture. *Breast Cancer Res* **7**(1): R46-59.
35. Gao M.Q., *et al*. (2010) Stromal fibroblasts from the interface zone of human breast carcinomas induce an epithelial-mesenchymal transition-like state in breast cancer cells in vitro. *J Cell Science* **123**(20): 3507-3514.
36. Dovas A., *et al*. (2012) Imaging interactions between macrophages and tumor cells that are involved in metastasis in vivo and in vitro. *J Microsc* doi: 10.1111/j.1365-2818.2012.03667.x
37. Delort L., *et al*. (2013) Reciprocal interactions between breast tumor and its adipose microenvironment based on a 3D adipose equivalent model. *PLoS One* **8**(6): e66284.
38. Nikkhah M., *et al*. (2011) MCF10A and MDA-MB-231 human breast basal epithelial cell co-culture in silicon micro-arrays. *Biomaterials* **32**(30): 7625-7632.
39. Volinia S., and Croce C.M. (2013) Prognostic microRNA/mRNA signature from the integrated analysis of patients with invasive breast cancer. *Proc Natl Acad Sci USA* **110**(18): 7413-7417
40. Wang Y., *et al*. (2005) Gene-expression profiles to predict distant metastasis of lymph-node-negative primary breast cancer. *Lancet* **365**(9460): 671-679.
41. Chang H.Y., *et al*. (2005) Robustness, scalability, and integration of a wound-response gene expression signature in predicting breast cancer survival. *Proc Natl Acad Sci USA* **102**(10): 3738-3743.
42. Liu R., *et al*. (2007) The prognostic role of a gene signature from tumorigenic breast-cancer cells. *N Engl J Med* **356**(3): 217-226.
43. Finak G., *et al*. (2008) Stromal gene expression predicts clinical outcome in breast cancer. *Nature Med* **14**(5): 518-527.
44. Chang H.Y., *et al*. (2004) Gene expression signature of fibroblast serum response predicts human cancer progression: Similarities between tumors and wounds. *PLoS Biology* **2**(2): e7.
45. Van't Veer L.J., *et al.* (2002) Gene expression profiling predicts clinical outcome of breast cancer. *Nature* **415**(6871): 530-536.

46. Van de Vijver M.J., *et al.* (2002) A gene-expression signature as a predictor of survival in breast cancer. *N Engl J Med* **347**(25): 1999-2009.
47. Cronin M., *et al*. (2004) Measurement of gene expression in archival paraffin-embedded tissues: development and performance of a 92-gene reverse transcriptase-polymerase chain reaction assay. *Am J Pathol*. **164**: 35-42
48. Cronin M. *et al.* (2007) Analytical validation of the Oncotype DX genomic diagnostic test for recurrence prognosis and therapeutic response prediction in node-negative, estrogen receptor-positive breast cancer. *Clin Chem* **53**: 1084-1091.
49. Perou C.M., *et al.* (2000) Molecular portraits of human breast tumors. *Nature* **406**: 747-752
50. Sørlie T., *et al*. (2001) Gene expression patterns of breast carcinomas distinguish tumor subclasses with clinical implications. *Proc Natl Acad Sci USA* **98**: 10869-10874.
51. Parker J.S., *et al*. (2009) Supervised risk predictor of breast cancer based on intrinsic subtypes. *J Clin Oncol* **27**(8): 1160-1167.
52. Bhargava R. (2013) Infrared spectroscopic imaging: The next generation. A*ppl Spectrosc* **67**(1): 93-105.
53. Matthäus C., *et al*. (2008) Chapter 10: Infrared and Raman microscopy in cell biology. *Methods Cell Biol* **89:** 275-308.
54. Holton S.E., Walsh M.J., Kajdaçsy-Balla A., and Bhargava R. (2010) Label-free characterization of cancer-activated fibroblasts using infrared spectroscopic imaging. *Biophysical Journal* **101**(6): 1513-1521.
55. Holton S.E., Walsh M.J., and Bhargava R. (2010) Subcellular localization of early biochemical transformations in cancer-activated fibroblasts using infrared spectroscopic imaging. *Analyst* **136**(14): 2953-2958.
56. Kong R., Reddy R.K., and Bhargava R. (2010) Characterization of tumor progression in engineered tissue using infrared spectroscopic imaging. *Analyst* **135**: 1569-1578.
57. Holton S.E. (2010) *Use of Fourier transform-infrared spectroscopic imaging as a tool for understanding earlier molecular events driving breast cancer progression*. (Unpublished master's thesis). University of Illinois at Urbana-Champaign. Urbana, IL.
58. Chan K.L.A. and Kazarian S.G. (2003) New opportunities in micro- and macro-attenuated total reflection infrared spectroscopic imaging: Spatial resolution and sampling versatility. *Appl Spectrosc* **57**(4): 381-389.

59. Gazi E., *et al* (2009) A FTIR microspectroscopic study of the uptake and metabolism of isotopically labeled fatty acids by metastatic prostate cancer. *Vib Spectrosc* **50**: 99-105.
60. Kondo T. (1997) The assignment of IR absorption bands due to free hydroxyl groups in cellulose. *Cellulose* **4(4):** 281-292.
61. Naumann D. (2001) FT-infrared and FT-raman spectroscopy in biomedical research. *Applied Spectroscopy Reviews*. **36**(2-3): 239-298.
62. Crowe J.H., *et al*. (1989) Lipid phase transitions measured in intact cells with Fourier transform infrared spectroscopy. *Cryobiology* **26**: 76-84.
63. Dreissig I., *et al*. (2009) Quantification of brain lipids by FTIR spectroscopy and partial least squares regression. *Spectrochimica Acta Part A: Molecular and Biomolecular Spectroscopy*. **71(5):** 2069-2075.
64. Belbachir K., *et al.* (2009) Collagen types analysis and differentiation by FTIR spectroscopy. *Anal Bioanal Chem* **395:** 829-837.

## CHAPTER TWO: THREE-DIMENSIONAL CELL CULTURE MODELS FOR STUDYING THE EFFECT OF FIBROBLASTS ON BREAST CANCER PHENOTYPES

**Abstract**

Approximately 232,340 women will be newly diagnosed with breast cancer in 2013. With advances in screening and diagnosis, confined disease is being detected earlier. Cancer management strategies would benefit greatly from an improved understanding of early molecular events that control cancer progression. In confined breast carcinomas, these events are driven by the reciprocal interaction between the cancerous epithelium and its microenvironment, the stroma. Sophisticated cell culture techniques have emerged as a way to study this interaction. Here, we report a novel three-dimensional co-culture model that combines the MCF10A mammary acinar model with a stroma simulated by primary human fibroblasts embedded in a type I collagen matrix. This layered model enabled the growth of two cell types in a complex environment while allowing for the easy mechanical separation of the two populations. The effects of propagating signals through the environment were studied by using a two-stage sandwich co-culture model. By first co-culturing the stroma with MCF-7 tumorigenic breast epithelial cells and allowing the fibroblasts to become activated, a cancerous molecular signature propagates through the stroma to affect the normal adjacent epithelium. The changes in the normal epithelium were assessed using proliferation and migration assays, morphology as determined through hematoxylin & eosin staining, quantitative real-time PCR for gene expression, and Fourier Transform Infrared (FT-IR) spectroscopic imaging. Label-free FT-IR can measure global chemical changes within a sample and can lead to better understanding of the early molecular events occurring between a tumor and its microenvironment.

**Introduction**

Carcinomas, including those arising from the epithelium of skin, breast, prostate, and colon, are the most common types of cancer and their worldwide incidence is increasing (1). While the global genomic and proteomic landscapes are being mapped, the dynamics of the etiology of most carcinomas are still not defined. Attention has shifted to so-called 'targetable' mutations, but the systematic study of both targets and potential therapies continues to be done with animal models and monolayer culture based approaches.

The importance of developing more physiological systems for studying cancer has been appreciated over the last decade (2-5). It is now understood that cells are extremely sensitive to their mechanical and chemical environments, both locally and globally (6-9). Both normal and cancer cells have different gene expression signatures when grown in three-dimensional (3D) culture compared to growth on tissue culture plastic. It has been shown that the genomic profile of breast cancer cells grown in a 3D matrix resembles that of human disease states (4), while the profile of cells grown in monolayer culture does not. Recently, advanced 3D culture models for studying breast cancer have been developed in which the normal breast epithelial architecture is maintained (2,10). These models can be used to study genetic influences on cancer progression (11-12) and can also be used to test novel therapeutic agents (13-14).

While consideration of the mechanical and chemical environment of breast cancer cells is important for relating *in vitro* studies to human disease, the tumor microenvironment has also been implicated in the progression of cancer and resistance to therapies (15-17). The tumor microenvironment is a complex milieu of mesenchymal and myeloid derived cells, extracellular matrix proteins, and chemical signals (Figure 2.1). Many cell types have been identified as potential drivers of tumor progression including macrophages (18), adipocytes (19), and fibroblasts (20). Co-culture models are used to study the interaction between tumor cells and other cells present in the environment. In the past, the cells are grown in two-dimensions either mixed together or separated by a membrane that allows soluble factors to be exchanged between the two cell types. More recently, microfluidic co-cultures have been developed that allow for the study of interaction dynamics (21). Although cancer cells are known to behave differently in 3D culture, there are few co-culture studies that combine 3D culture conditions with multiple cell types. Those that have been developed are limited by the fact that the cells are mixed together and must be separated before molecular analyses of single cell type

profiles. Studies to determine gene expression are extremely sensitive to the presence of other cells and the genetic changes determined with these methods will always be an average of the contributions of both cell types. Separation of mixed populations of cells is challenging due to the lack of robust cell surface markers for certain tumor cells, for example cancer stem cells (22). Thus, we were motivated to develop a three-dimensional co-culture environment in which the cells could be grown together for a prescribed amount of time before separating them without the use of antibody-dependent bead-based approaches.

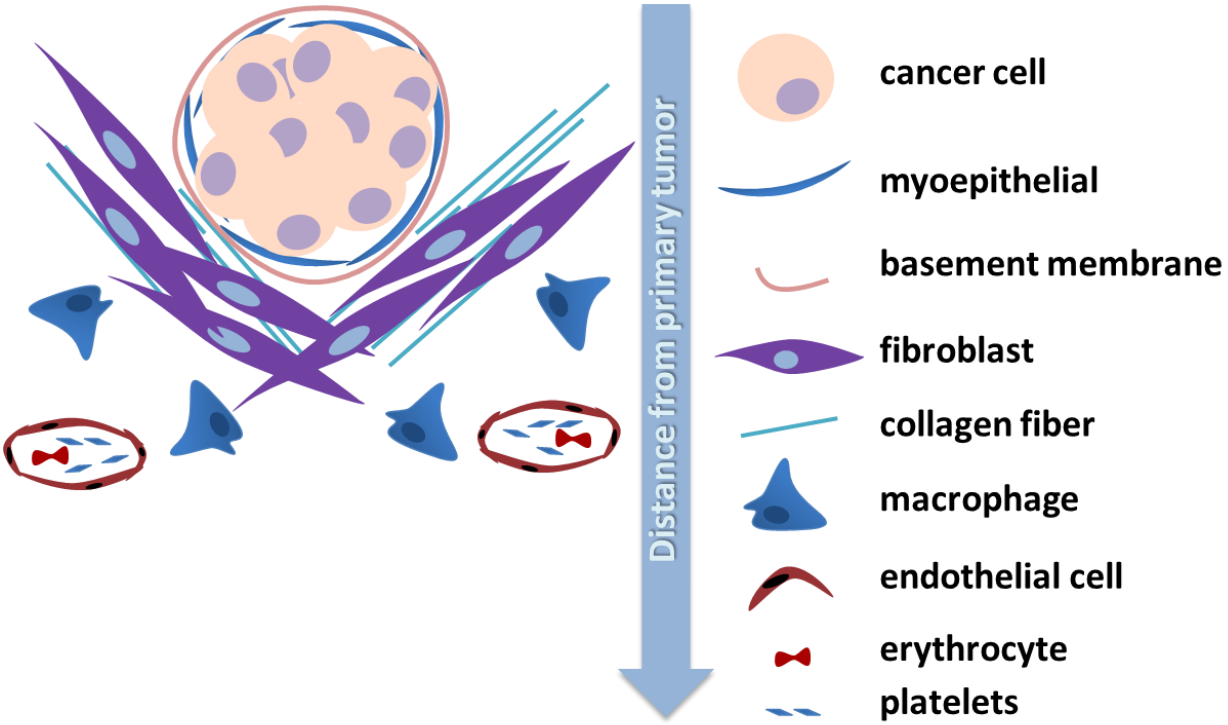


**Figure 2.1: The microenvironment milieu.** Fibroblasts are the first stromal cells to contact signals from the primary tumor**.**

While many cells have been implicated in affecting cancer cell phenotypes, we focused on fibroblast-epithelial interactions. When fibroblasts are co-cultured with breast cancer cells, they undergo a transformation and become more myofibroblast-like; this is characterized by the expression of α-smooth muscle actin protein (α-SMA). These cancer-activated fibroblasts (CAFs) are suggested to promote breast cancer progression (23). While the interaction between breast cancer cells and fibroblasts is well characterized in both cells (24-26) and tissues (27), how the presence of activated fibroblasts affects nearby normal epithelium is still unclear. We aimed to develop a model that could be used to study the propagation of cancerous molecular signatures from the tumor to nearby normal epithelium via the stroma, and in particular via fibroblast activation.

For this study, we developed a layered co-culture model in which breast cancer cells and primary fibroblasts were embedded within a type I collagen hydrogel. The layered model allowed for the communication between the two cell types via soluble factors in a more physiologically realistic system. After co-culture, the layers were peeled apart with forceps; each layer could be separately digested to isolate RNA from the individual cell types. To identify whether cancerous molecular signatures were propagated via the stroma, the layered model was used in a two-stage co-culture. Primary fibroblasts were first co-cultured with MCF-7 breast cancer cells in the layered model and, upon activation, that layer was peeled off and subsequently co-cultured with nontumorigenic MCF10A breast epithelial cells that were grown in 3D as growth-arrested acini. Phenotypes of cancerous transformation were monitored in MCF10A cells, including increased proliferation and increased migration, as well as expression of genes known to be altered in tumors.

While bulk measurements, including cell-based assays and gene expression profiling, are the gold-standard in determining cancerous phenotypes *in vitro*, it is known that cancer cells are comprised of heterogeneous populations with widely varied phenotypes (28-29). In order to address cellular heterogeneity, as well as to understand the dynamic and reciprocal interactions between cell types, we used Fourier transform infrared (FT-IR) spectroscopic imaging to monitor bio-molecular changes in our cell culture samples. This label-free imaging method measures the characteristic absorption of energy by molecular bonds within a sample, and this can be used to determine spectroscopic signatures of cellular transformations in heterogeneous samples (30). By combining a novel 3D cell co-culture system with label-free chemical imaging, we aimed to understand the dynamic and reciprocal interactions between fibroblasts, breast cancer cells, and normal breast epithelial cells and how this interaction influences cancer progression.

**Results**

*Development and Validation*

We were motivated to develop a three-dimensional cell co-culture model in which the cells could be grown together and separated easily. We came up with a layered model concept, referred to hereafter as the 'Sandwich,' where cells were embedded within hydrogels that were prepared sequentially such that a natural interface formed between the layers. This interface allows for the easy

separation of individual cell types because they are confined within the gel layer. Our other specifications for the model are outlined in Figure 2.2. Perhaps most importantly, the collagen gels are polymerized slowly by pre-incubating at 4°C for one hour prior to polymerization for one hour at 37°C. This controls the collagen fiber alignment and size as the hydrogel forms without any damage to the cells that are embedded within (31). These parameters are important to consider when culturing primary fibroblasts, as these cells are extremely sensitive to both local and global mechanical forces.

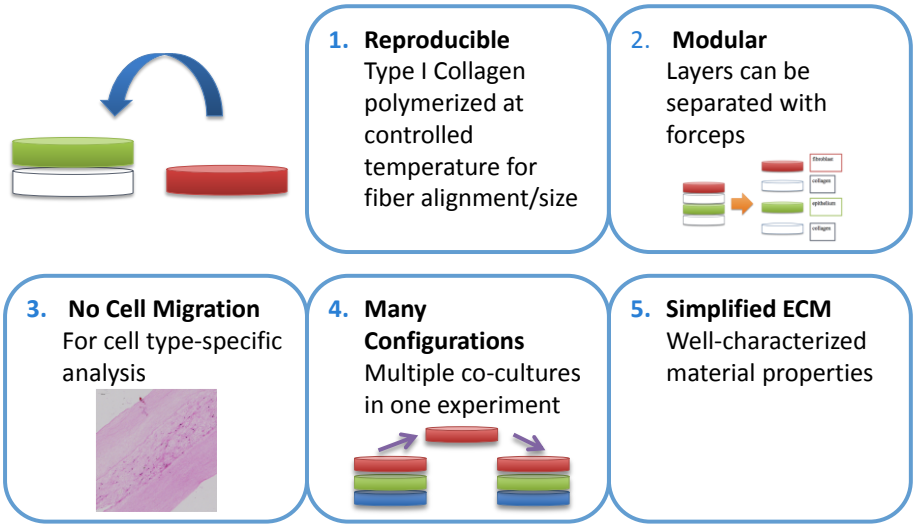


**Figure 2.2: Design considerations for 3D co-culture model.**

The cell interaction studied first was that between a widely-used breast cancer cell line, MCF-7, and primary normal dermal fibroblasts (NDF). Dermal fibroblasts were chosen for this initial study because mammary fibroblasts were not commercially available at the time, and NDF do not express high basal levels of α-SMA, the most widely used marker of the fibroblast-myofibroblast differentiation and cancer-activated fibroblasts (CAFs) (32). These cells had been used previously by our group and the dynamics of the interaction were characterized using immunofluorescence and FT-IR spectroscopic imaging (25-26). MCF-7 cells were able to activate NDF in the layered sandwich model after 12 hours of co-culture (Figure 2.3). As a positive control, NDF were treated with 1.5 ng/mL TGF-β1, a potent stimulator of the fibroblast-myofibroblast activation (33).

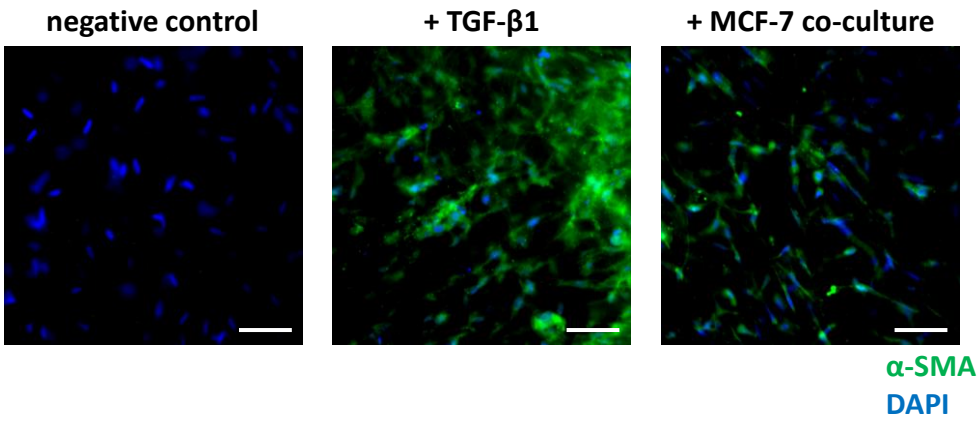


**Figure 2.3: 3D Fibroblast activation by 12h treatment with TGF-β1 or 12h co-culture with MCF-7.** Scale bar represents 50 μm.

The primary design consideration of the co-culture model was to ensure that there was no cell migration between the layers. This enables the facile separation of cell-containing layers by forceps, rather than separating the cells using magnetic bead pull-down or fluorescence assisted cell sorting (FACS). Although MCF-7 are not highly invasive in culture compared to other tumorigenic breast cancer cells (34), we wished to determine whether the cells were migrating between the layers in the sandwich model. A two-layered model was created in which MCF-7 and NDF were grown in separate layers. Samples were fixed at 6h, 12h, 24h, 48h, 96h, and 1 week, paraffin embedded, sectioned, and stained for the epithelial marker cytokeratin or mesenchymal marker vimentin. While the MCF-7 layers showed positive staining for cytokeratin, they were negative for vimentin staining, indicating the fibroblasts had not migrated into this layer. Conversely, the NDF layers showed positive staining for vimentin but were negative for cytokeratin, indicating that the MCF-7 also had not invaded (Figure 2.4).

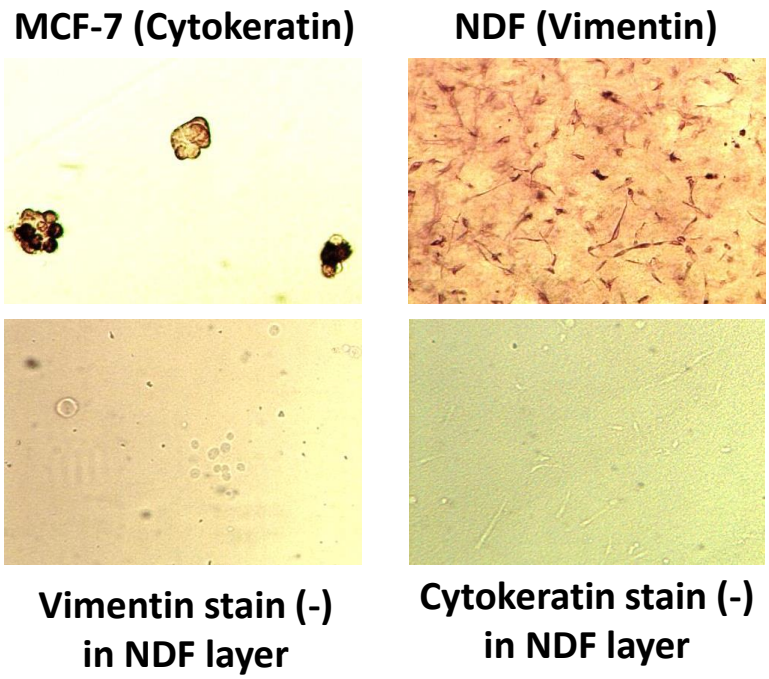


**Figure 2.4: Absence of cellular cross-migration was confirmed through immunohistochemical staining of individual cell layers for epithelial marker cytokeratin and mesenchymal marker vimentin.**

*A two-stage co-culture model*

After the sandwich culture was validated, we wanted to use the model to determine how cancerous signatures were propagated through the stroma, and in particular via activation of fibroblasts. A two-stage co-culture was developed in which NDF were first grown with MCF-7 and then, upon activation, co-cultured with MCF10A grown as growth-arrested acini. The schematic for setting up the experiment is depicted in Figure 2.5. MCF10A, a nontumorigenic breast epithelial line, has been widely used to understand the molecular drivers of breast tumors because it forms structures that have characteristically normal cellular architecture when grown in recombinant basement membrane gels (2). The cells become growth arrested spheroids after 8-10 days of culture and form normal cell-cell junctions with apical-basal polarity. Fibroblasts were activated after 12h co-culture with MCF-7 (Figure 2.3) prior to co-culture with MCF10A acini. After 6, 12, 24, 36, 48, 72, and 168h, the MCF10A were analyzed for cancerous cellular phenotypes including increased proliferation, increased invasive potential, and gross differences in cytoarchitecture and morphology. As a control, naïve NDF (cells not previously co-cultured) were also grown with MCF10A acini for the same lengths of time.

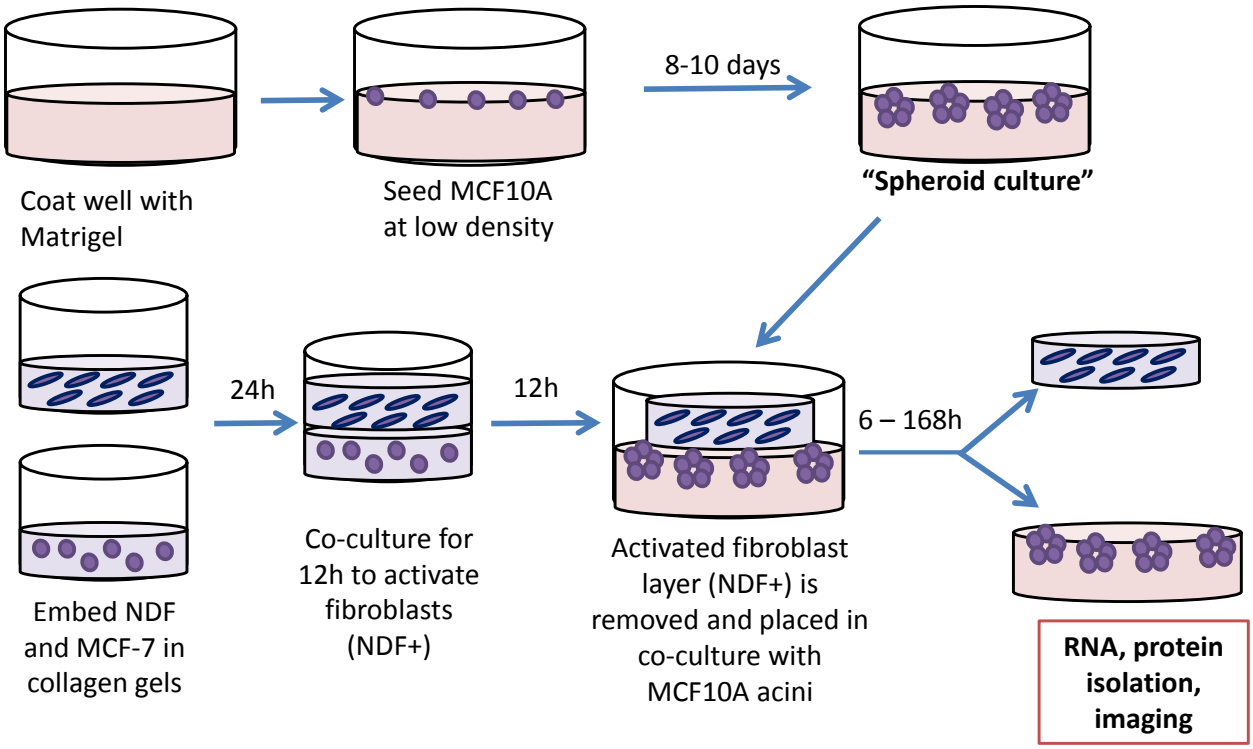


**Figure 2.5: Setting up the two-stage co-culture model.**

*MCF10A undergo morphological changes after co-culture with activated fibroblasts*

MCF10A form stable, growth-arrested acinar structures with clear lumens after 8 days in culture (2). Therefore, we used disruption of the acinar structure as a preliminary test of the capacity of activated fibroblasts to induce oncogenic changes in these previously nontumorigenic cells. Samples were sectioned and subsequently stained using hematoxylin and eosin (H&E), a commonly-used histologic stain that is used to distinguish nuclei (stained purple) from other eosinophilic structures (stained red or pink). While a section through MCF10A cells grown alone reveals a single layer of cells surrounding a clear, central lumen, co-culture induces morphological changes in the acinar structure. After co-culture with activated fibroblasts (referred to hereafter as NDF+), cells were seen invading into the luminal space (Figure 2.6). However, after 24h of co-culture with NDF+ the acinar structure is completely lost, as cells continue to proliferate into the luminal space. This is not seen in all acini on the slide, suggesting there may be heterogeneity in the MCF10A response to fibroblast co-culture.

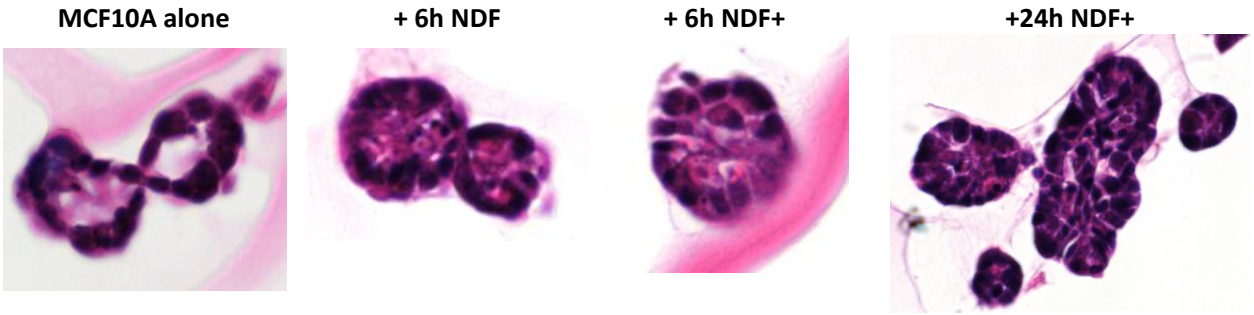


**Figure 2.6: Hematoxylin and eosin stained MCF10A acini after co-culture.** After only 6 hours of co-culture with activated NDF, there is invasion into the luminal space. After 24h, the cells are proliferating into the luminal space and the architecture is highly disrupted.

*MCF10A become more proliferative after co-culture with activated fibroblasts*

Three of the ten "hallmarks of cancer" are sustaining proliferative signaling, evading growth suppressors, and resisting cell death (35). It was important to assess whether MCF10A were in fact more proliferative after co-culture with NDF+. First, a proliferation assay was done in which cells were digested out of the basement membrane matrix and plated in monolayer culture. After 24, 48, or 72h, cells were trypsinized and counted (Figure 2.7). It appears that after 48h co-culture with NDF+, MCF10A have been transformed such that they proliferate at an increased rate even when the stimulus is removed. However, there is a large degree of error associated with this experiment. This is not an accurate representation of proliferation, as the cells may be responding to the changed environment rather than a fibroblast-induced transformation. Therefore, proliferative potential was measured by staining MCF10A acini *in situ* for the presence of Ki67 protein (Figure 2.8), a marker of entry into the active phase of cell cycle (36). In growth-arrested MCF10A cells, this protein is absent from the nucleus (2).

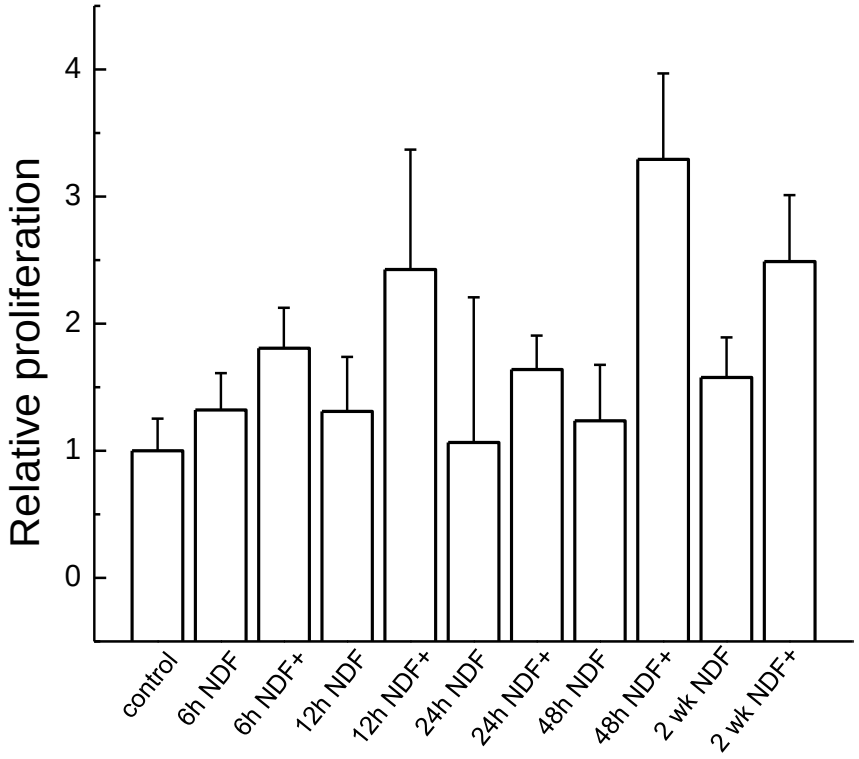


**Figure 2.7: Proliferation assay shows differences between MCF10A with and without co-culture.**

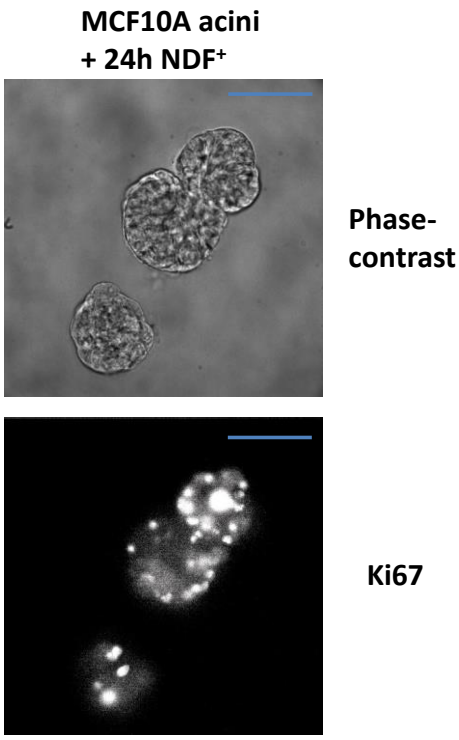


**Figure 2.8: Phase-contrast (top) and immunofluorescence imaging of MCF10A acini.** Upon co-culture with activated fibroblasts, previously growth-arrested cells begin to proliferate, expressing Ki67. Scale bar represents 50 µm.

*MCF10A become more invasive after co-culture with activated fibroblasts*

Although proliferation is a hallmark of tumorigenesis, confined carcinomas are rarely lethal. Rather, the mortality associated with cancer is the result of metastatic disease, after tumor cells invade the basement membrane and enter the bloodstream. Therefore, we aimed to measure the invasive potential of MCF10A cells after co-culture with normal or activated fibroblasts. We hypothesized that activated fibroblasts would transform the MCF10A such that they were more invasive in a standard wound healing assay. After co-culture with NDF or NDF+, MCF10A acini were digested from Matrigel and plated in monolayer culture. After a confluent monolayer formed, the plate was scratched and then images were taken every 6 hours for a total of 48 hours (Figure 2.9). While cells co-cultured with NDF+ for 6 hours were significantly more migratory than naïve MCF10A, co-culture with non-activated fibroblasts also induced a mild migratory phenotype. Interestingly, this trend was lost when the fibroblasts had been co-cultured for longer than 6 hours. This suggests either transience in the activated state of fibroblasts or in the interaction between fibroblasts and MCF10A cells.

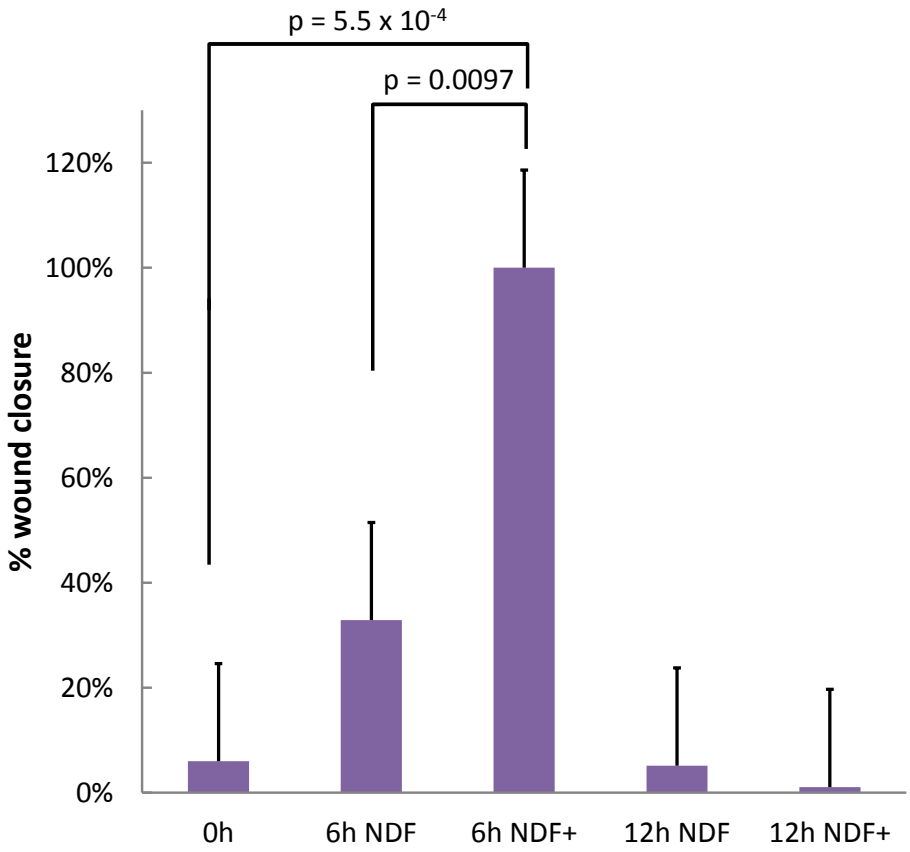


**Figure 2.9: Migration of MCF10A with and without co-culture as a fraction of wound closure.** MCF10A are significantly more invasive after co-culture with NDF+ for 6 hours. Interestingly, this property is lost at a sustained co-culture time.

*Co-culture with fibroblasts changes the gene expression of key genes in MCF10A acini*

Finally, we wished to determine what impact fibroblast co-culture has on the gene expression of MCF10A acini. Several key genes previously indicated in fibroblast-epithelial interactions were measured. IL-6 is known to be involved in the paracrine signaling between cancer cells and fibroblasts, and has been implicated in paracrine and autocrine networks that promote invasive phenotypes in prostate cancer (37). After co-culture with NDF+, IL-6 was upregulated compared to naïve MCF10A (Figure 2.10). Conversely, IL-6 is downregulated in MCF10A after co-culture with NDF. The paracrine signaling axis of NDF/MCF10A differs from that of NDF+/MCF10A, and is dynamic over time. In three independent replicates, the level of IL-6 mRNA in MCF10A after co-culture with NDF+ was highly variable, depicted by the large error bars in these samples. Because these are bulk measurements that take into account the mRNA levels of thousands of cells, this error could represent the heterogeneity induced in MCF10A acini upon co-culture with NDF+. After one week of co-culture, there may still be cells that are growth-arrested or undergoing apoptosis, which would reduce the overall mRNA

expression of IL-6 because these cells are not actively undergoing transcription of this gene. A more appropriate assay would be to check the IL-6 protein level using ELISA or western blot, to determine how much is being produced.

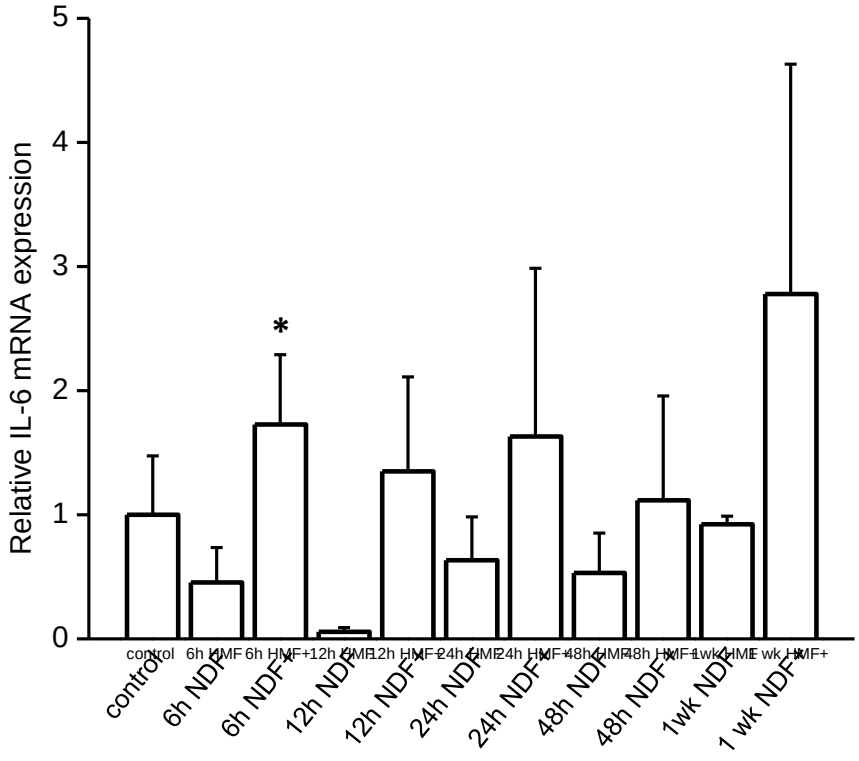


**Figure 2.10: Relative mRNA expression of IL-6.** Co-culture with NDF+ increases IL-6 expression and this trend is sustained at longer timepoints. Significance of $p < 0.05$ is marked by *.

Next, E-cadherin gene expression was measured (Figure 2.11). Loss of this protein, important for maintaining normal epithelial cell-cell junctions, is a hallmark of the epithelial-to-mesenchymal transition (EMT) and is associated with invasive phenotypes and metastatic disease (38-40). Fibroblasts have been previously shown to induce an EMT in breast cancer cells and this will be discussed more thoroughly in Chapter 3 (41). When NDF or NDF+ were co-cultured with MCF10A acini, mRNA levels of E-cadherin were quickly downregulated, after only 6 hours of co-culture. This early response was lost, however, after longer periods of co-culture. Again, this could indicate a transient phenotype in the fibroblast activation or in the response of MCF10A to stimuli secreted by NDF or NDF+. Interestingly, both normal and cancer-activated fibroblasts can induce this change.

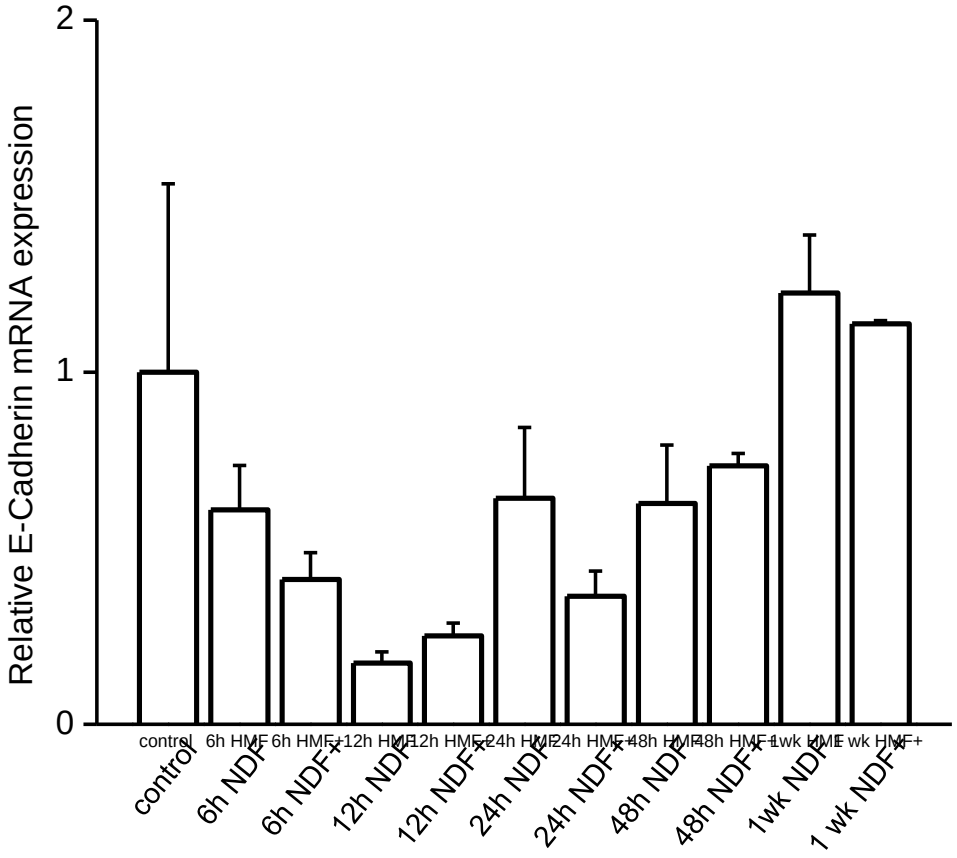


**Figure 2.11: Relative mRNA level of E-cadherin, a marker of normal epithelial cell-cell junctions.** E-cadherin is downregulated in both conditions but the levels are restored after 1 week of co-culture. There were no significant differences between conditions.

*Chemical imaging can be used to measure cellular transformations in MCF10A cells after co-culture*

Finally, we employed vibrational spectroscopy to determine global chemical changes occurring across MCF10A acini after co-culture with NDF and NDF+. We have used FT-IR spectroscopic imaging previously to monitor the fibroblast activation process in 3D co-culture with MCF-7 cells (25). Here, we aimed to understand the effect activated fibroblasts have on the spectral signatures of normal breast epithelial cells. Acini were paraffin embedded and sectioned onto IR-reflective substrates. Attenuated total reflectance (ATR) mode was used in order to obtain a pixel size of 1.56 x 1.56 µm. With this mode, the acinar structure can be seen, although individual cells cannot be discriminated (Figure 2.12). Individual acini were analyzed and the spectra from each condition were averaged. The average spectra for the 24h timepoint is shown in Figure 2.13. There are apparent differences in the peak at 3300 $cm^{-1}$, associated with the N-H bond of proteins, however this peak is not used in our analysis due to its large variability across samples from sample processing. This large peak is effectively masked out of our

analysis. There are two primary regions of interest on the IR spectrum for studying cell biology: the C-H stretching region (3000-2800 $cm^{-1}$), containing peaks from $CH_2$ and $CH_3$ stretching, and the so-called fingerprint region (1750-950 $cm^{-1}$). The C-H stretching region is associated with fatty acids, lipids, and general metabolism (42). Analysis of this region across the three samples displayed reveals striking differences between the three culture conditions (Figure 2.14). Co-culture with NDF for 24h induces a peak shift in all three peaks of the region. Co-culture with NDF+, however, reduces the absorbance at the 2956 $cm^{-1}$ peak and a shift at the 2850 $cm^{-1}$ peak. Importantly, the three co-culture conditions can be readily distinguished using FT-IR. In the fingerprint region, however, the peak most closely associated with the phosphate backbone of nucleic acids (1080 $cm^{-1}$) is greatly increased upon co-culture with NDF+ (Figure 2.15). This corresponds to NDF+ acting as a stimulant for MCF10A proliferation after 24 hours of co-culture.

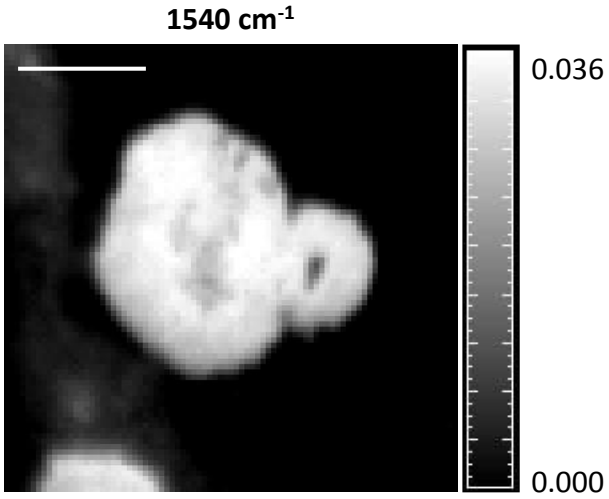


**Figure 2.12: MCF10A acinus after 24h co-culture with NDF.** Image is of the peak at 1540 $cm^{-1}$, corresponding to Amide II (N-H (40-60%) and C-N stretching (18-40%)). Scale bar represents 50 µm.

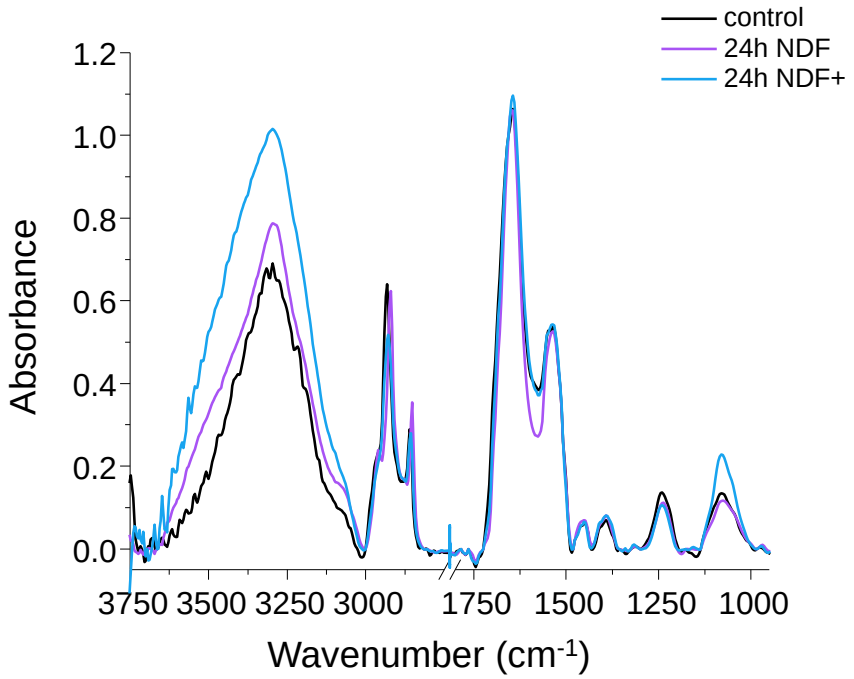


**Figure 2.13: There are spectroscopic differences in MCF10A after co-culture with NDF or NDF+.** The largest difference is seen at the 1080 $cm^{-1}$ peak, associated with nucleic acids.

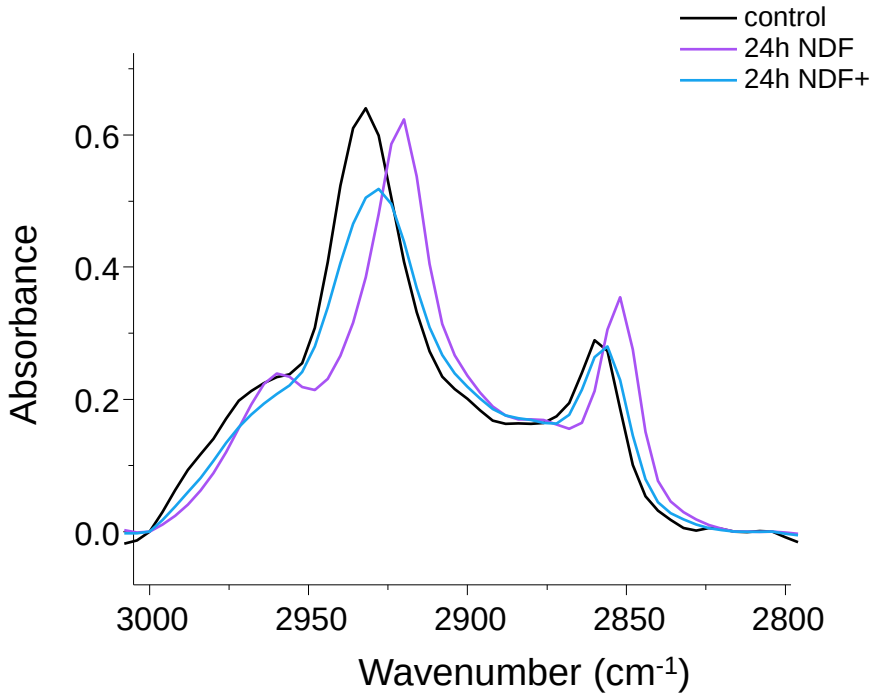


**Figure 2.14: Analysis of the C-H stretching region of the spectrum reveals peak shifts at three peaks associated with fatty acids and lipids after co-culture with NDF or NDF+.** NDF appear to induce the largest changes in this region.

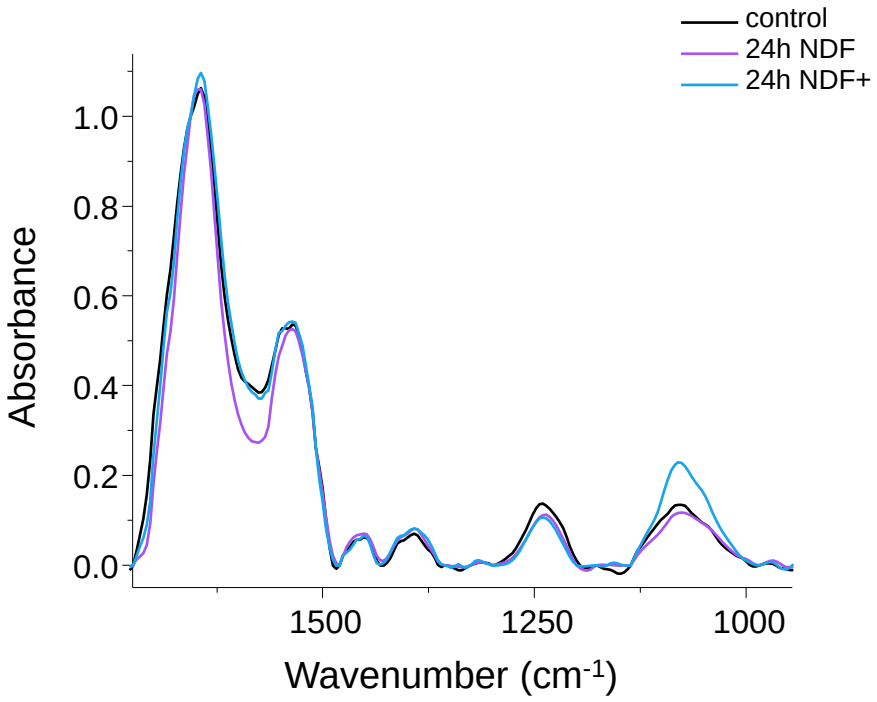


**Figure 2.15: The fingerprint region (1750-950 $cm^{-1}$) reveals a number of changes, including a peak shift at Amide II and a large increase in the peak at 1080 $cm^{-1}$, associated with nucleic acids, after co-culture with NDF+ but not NDF.**

**Discussion**

We have developed a novel 3D co-culture model for studying the interactions between fibroblasts and epithelial cells during early breast cancer progression. While there are many 3D culture platforms for studying cell cross-talk (10**,** 21, 43), our model has a number of unique features. The model uses a layered system that is reproducible and is modular, allowing for multiple co-culture configurations within a single experiment. We used the model in a two-stage co-culture experiment, in which primary fibroblasts were activated through co-culture with MCF-7 cells; these were subsequently co-cultured with growth-arrested MCF10A acini. We used this system to understand how cancerous molecular signatures propagate through the stroma and affect nearby epithelium. MCF10A acini were analyzed for various cancerous phenotypes, including proliferation, migration, and altered gene expression, as well as analysis of spectroscopic signatures associated with proliferation and metabolism.

We found that cancer-activated fibroblasts are sufficient for inducing cancerous phenotypes in growth-arrested mammary acini. The morphology of acini after co-culture with NDF+ was consistent with re-entry into the cell cycle and proliferation into the luminal space, forming a tumor-like structure. Although this type of morphology has been induced by the activation of oncogenes *in vitro* (11-12), this is the first time this has been shown to be the result of aberrant signaling between fibroblasts and a model of normal breast epithelium. Further, the MCF10A are transformed such that even after they are removed from the 3D matrix and seeded back onto tissue culture plastic, they are more proliferative. Fibroblast-activated MCF10A were also significantly more migratory in a wound healing assay. While the phenotype is transient in 3D co-culture, a combination of aberrant cellular signaling and the mechanical stress from the tissue culture plastic transform nontumorigenic epithelial cells into cancer-like cells. To further test the tumorigenic potential of these activated MCF10A cells, an animal model should be used.

Further evidence to support an MCF10A transformation was shown by measuring the expression of two genes associated with fibroblast-epithelial interactions in the tumor microenvironment. Co-culture with NDF+ induces IL-6 overexpression in MCF10A, which could indicate the beginnings of a paracrine signaling loop between transformed epithelial cells and other stromal cells. IL-6 secretion has been implicated in recruitment of inflammatory cells, which have been correlated with poor outcome in several cancer types (44-45). Further, high IL-6 serum levels detected in breast cancer patients is a prognostic indicator for poor prognosis (46-48). Our studies suggest that IL-6 may be released by transformed epithelial cells upon contact with activated fibroblasts, serving as a

marker for tumor progression even after the primary tumor has been removed. IL-6 expression is also associated with an EMT phenotype, characterized by loss of E-cadherin (49). Gene expression analysis shows that while both NDF and NDF+ reduce the levels of E-cadherin in MCF10A, E-cadherin levels are recovered after 1 week. The transience of the EMT phenotype may further indicate that a second 'hit' is necessary for them to become cancerous, or it is possible that fibroblasts lose their activation state after many days in co-culture with MCF10A. An experiment in which fibroblasts are continually activated by MCF-7, or in which activated fibroblasts are added every day to an MCF10A co-culture would determine if the limiting step in driving EMT is the activation state of the fibroblasts or the plasticity of MCF10A cells.

Although we hypothesized that co-culture with activated fibroblasts would alter MCF10A phenotypes, we found that normal fibroblasts can also induce some changes in normal epithelial cells. While normal fibroblasts have been indicated to be anti-proliferative to both breast cancer cells and normal epithelial cells in the literature (50), we show that MCF10A have a response to NDF within the first 6-12 hours of co-culture. This appears to be more transient than the effect of NDF+ on MCF10A, but it is worth noting. The phenotypic changes seen in MCF10A suggest that growing epithelial cells in either monolayer or 3D culture is very dissimilar to growing them in co-culture with fibroblasts, regardless of their activation state. These findings indicate that co-cultures should be used over monocultures in doing systematic analysis of factors that are implicated in driving tumor progression or in drug testing and development.

Finally, FT-IR imaging was used to differentiate between the effect of NDF and NDF+ co-culture on the chemical changes induced in normal epithelial cells. We found that label-free FT-IR imaging can differentiate between the co-culture conditions. Absorbance in a peak associated with nucleic acids is significantly increased after co-culture with NDF+ compared to NDF, corresponding to the ability of activated fibroblasts to stimulate proliferation in normal epithelial cells. We used this system as a proof-of-principle to show that label-free chemical imaging may be used to determine activation state in epithelial cells. We have previously shown that FT-IR can be used to characterize the dynamics of fibroblast activation in 3D culture (25), but this is the first time that the transition from normal to cancerous epithelium has been monitored using this technique.

In conclusion, we developed a novel three-dimensional co-culture model in which the cells could be grown together in a physiological context and then easily separated with no cell crossover. This layered system was used to study the role of fibroblasts in the propagation of cancerous signals from the primary tumor to nearby normal epithelium. Fibroblast-activated MCF10A showed the cancerous phenotypes of enhanced proliferation and migration as well as alterations in morphology and gene expression. We label this a transformation rather than a reaction because the MCF10A retained these hallmarks even after the fibroblast stimulus was removed and the environmental context was changed. An analysis of the chemical changes upon activation was also done, showing that activated MCF10A acini show chemical hallmarks of enhanced metabolism and proliferation. This system of an advanced cell culture model coupled with both molecular approaches and chemical imaging can reveal new insights into the dynamic and reciprocal interactions between cancer cells, fibroblasts, and normal epithelium.

**Materials and Methods**

*Cell Culture*

MCF10A cells (a gift from Senthil Muthuswamy, Cold Spring Harbor Laboratory) were maintained in monolayer culture with DMEM/F12 (Invitrogen, Life Technologies, Carlsbad, California, USA) supplemented with 5% Horse Serum (Sigma-Aldrich, St. Louis, Missouri, USA), 20 ng/mL Epidermal growth factor (EGF, Peprotech, Rocky Hill, New Jersey, USA), 0.5 μg/mL Hydrocortisone (Sigma-Aldrich), 0.1 μg/ml Cholera Toxin (Sigma-Aldrich), 0.01 mg/ml Insulin (Sigma-Aldrich), and 1% Pen/Strep (Gibco, Life Technologies). Cells were grown as previously described (2). Normal adult primary dermal fibroblasts (NDF, ScienCell Research Laboratories, Carlsbad, California, USA) were maintained in complete fibroblast medium (FM, basal medium supplemented with 2% Fetal Bovine Serum (FBS), 1% Fibroblast Growth Supplement (FGS), and 1% Pen/Strep). Fibroblasts were used prior to passage 7 to ensure that the fibroblasts were not entering senescence. MCF-7 cells (ATCC, Manassas, Virginia, USA) were maintained in Dulbecco's Modified Eagle Medium (DMEM) containing 10% FBS and 1% Pen/Strep.

*Preparation of 3D cultures*

For the 3D layered sandwich model ('Sandwich'), MCF-7 and HMF were embedded in a Type I collagen matrix, while MCF10A were grown as acinar structures in the Matrigel overlay culture. To prepare type I collagen gels with a final concentration of 2 mg/ml, pre-polymerized collagen (Type I collagen from rat tail tendon, BD Biosciences, San Jose, California, USA) was diluted 1:10 (v/v) with 10X

Phosphate-buffered saline (PBS). Cell suspension was added at a density of 1000 cells/µl for a total count of 300,000 cells/gel layer. 1N NaOH was added to the mix at a ratio of 0.023 µl NaOH/µl final volume in order to neutralize the acidic collagen and promote polymerization of the gel. The volume was brought up to the final volume (300 µl times the number of samples) in growth medium. After thorough pipetting with a P1000 micropipette, 300 µl of sample was dispensed into each well of a 48-well plate. The plate was then refrigerated at 4°C for 1 hour followed by polymerization at 37°C in a humidified, 5% $CO_2$ incubator for 45 minutes. After the gels were completely polymerized, 300 µl of fresh media was added to the top of the samples. Cells were equilibrated in the gels for 24 hours before setting up the experiment. This procedure was previously described in Holton *et al* (25).

3D acinar cultures were prepared by spreading a thin layer of growth factor-reduced Matrigel (BD Biosciences) in 24 -well plates and seeding a low density of MCF10A on top (4,000 cells/well). The cells were seeded in 0.5 ml of Assay Medium (Growth medium with 5 ng/ml EGF instead of 20 ng/ml) containing 2.5% dissolved Matrigel. Media was replaced every fourth day.

To prepare the Sandwich culture, NDF and MCF-7 gels were switched to low-serum (0.5% FBS) medium for 24 hours prior to co-culture. Then, NDF gels were layered on top of MCF-7 gels for 12 hours, allowing the NDF to become activated (NDF+), expressing α-SMA. As a control, some NDF samples were not co-cultured (labeled NDF). After the activation period, fibroblast gels were moved on top of MCF10A 3D cultures that had been growing for 12 days. The MCF10A cultures at this stage were growth-arrested, with normal cell-cell junctions and clear lumens. NDF/NDF+ and MCF10A acini were co-cultured for 6h, 12h, 24h, 72h, and 1 week prior to analysis.

*Proliferation Assay*

To perform the proliferation assay, MCF10A were removed from 3D matrices at prescribed timepoints by adding ice cold PBS until the Matrigel dissolved. MCF10A were then rescued in complete growth medium, centrifuged at 1000 rpm for 3 minutes, after which the pellet was resuspended in 9 mL complete growth medium. This was divided between three 5 cm petri dishes. Cells were allowed to adhere to the plates and grow for 24h, 48h, and 72h. At these timepoints, cells were trypsinized, rescued, centrifuged, and resuspended in 1 mL medium. Cells were counted twice and the cell counts averaged to get the total cell count per plate. To compare growth curves, cell counts for 48h and 72h were normalized to the 24h timepoint.

*Migration Assays*

A wound healing assay was set up in the same way as the proliferation assay in that MCF10A cells were digested out of the 3D matrix and re-plated in 3 plates containing equal numbers of cells. After 24 hours for the cells to form confluent monolayers, a P200 pipet was dragged in a straight line along the center of the dish to create a wound. At 0h and 48h pictures were taken to show the rate at which cells migrated to close the wound. Images were analyzed in ImageJ by measuring the distance across the wound at 3 points on each sample, prepared in triplicate. A student's two-tailed paired t-test was used to confirm significance of the migration assay data.

*Paraffin embedding*

For both immunohistochemistry and FT-IR imaging analysis, samples were fixed in freshly-prepared 4% paraformaldehyde for 1 h, mounted in Histogel (Thermo Fisher Scientific Inc., Waltham, Massachusetts, USA), and then paraffin-embedded. For paraffin embedding, samples mounted in Histogel were dehydrated with serial ethanol washes (50%, 70%, 80%, 95%, 100%, 100% for 3 h each) followed by three 2 h clearing steps in xylenes, and finally four 1 h paraffin infiltration steps (ParaPlast Plus, Sigma-Aldrich).

*Hematoxylin and Eosin Staining*

Hematoxylin and Eosin (H&E) staining was done on paraffin embedded 10 µm sections of MCF10A acini. In a glass staining dish, sections were deparaffinized and rehydrated with the following steps: 3 x 3 minutes in xylene, 3 x 3 minutes in 100% ethanol, 1 x 3 minutes in 95% ethanol, 1x 3 minutes in 80% ethanol, and 1 x 5 minutes in deionized water. Samples were then moved to hematoxylin (Sigma-Aldrich) for 3 minutes. Excess dye was removed by rinsing briefly in deionized water. Stain was developed by placing samples in tap water for 5 minutes and the samples were destained by dipping 8-12 times over 30 seconds in acid ethanol (70% ethanol containing 1% v/v HCl). The samples were further rinsed twice in tap water followed by a brief soak in deionized water. Excess water was blotted from the side holder before putting the samples in Eosin Y solution (Sigma-Aldrich) for 30 seconds. Samples were immediately moved to 95% ethanol for 5 minutes. Samples were dehydrated with the following steps: 2 x 5 minutes in 95% ethanol, 3 x 5 minutes in 100% ethanol, 3 x 15 minutes in xylene. Slides were hard mounted in Clarion Mounting Medium (Sigma-Aldrich, discontinued and replaced by Organo Limonene).

*Immunofluorescence*

Immunofluorescence on MCF-7 and NDF gels was done on the entire gel in order to preserve the cell structure. To do immunofluorescence on MCF10A gels *in situ*, Matrigel was spread on the glass window of 35 mm round glass bottomed dishes (MatTek, Ashland, Massachusetts, USA) before cultures were prepared as previously described. After washing media off with PBS, samples were fixed in cold, freshly-prepared 4% paraformaldehyde for one hour. Then, excess paraformaldehyde was removed by washing samples three times in ice cold PBS. 0.15 M glycine (in PBS) was added for 10 minutes at room temperature to quench the paraformaldehyde. Wash steps of 3 x 5 minutes in PBS were performed in between each step of the process. Cell membranes were permeabilized with 0.2% Triton X-100 (in PBS) for 15 minutes at room temperature. Samples were blocked in 5% non-fat dry milk or 5% bovine serum albumin (Sigma-Aldrich) in PBS overnight at 4°C or 3 hours at room temperature. After the blocking step, 3 x 5 minute washes were done in PBS containing 0.5% Tween-20 (PBS/T, Sigma-Aldrich). Primary antibodies were diluted 1:100-1:500 in PBS/T containing 1% BSA and samples were incubated for 1 hour at room temperature. Secondary antibodies were diluted 1:200-1:1000 in PBS/T containing 1% BSA for 1 hour at room temperature and were covered to prevent photobleaching. For nuclear staining, 300 nM DAPI (Invitrogen) in PBS/T was added for 10 minutes. After a final wash in PBS, samples were mounted with an anti-photobleaching agent (Vectashield H-100, Vector Laboratories, Burlingame, California, USA) and coverslipped before imaging. Primary antibodies used for this study were α-SMA (mouse anti-human IgG2, 1:100, Dako, Carpinteria, California, USA), Ki67 (rabbit anti-human IgG, 1:100, Invitrogen), E-cadherin (mouse monoclonal IgG1, clone 1.B.54, 1:100, santa cruz biotechnology, Dallas, Texas, USA). Secondary antibodies used were Goat anti-mouse IgG-FITC (1:500, Abcam, Cambridge, England, UK), Donkey anti-Rabbit IgG-AF546 (1:200, Invitrogen).

*Immunohistochemistry*

For IHC, samples were sectioned at 10 µm onto poly-L-lysine coated slides (Thermo Fisher Scientific, Waltham, Massachusetts, USA). Once dry, slides were deparaffinized (2 x 3 min xylene, 1 x 3 min 1:1 xylene/100% ethanol, 2 x 3 min 100% ethanol, 1 x 3 min 95% ethanol, 1 x 3 min 70% ethanol, 1 x 3 min 50% ethanol, cold tap water). Antigen retrieval was performed by boiling the samples in the microwave for 15 min in 10 mM sodium citrate buffer (pH 6.0). Slides were blocked in Tris-buffered saline (TBS) containing 10% FBS overnight at 4 °C. Primary antibody was added in TBS containing 1% BSA for one hour at room temperature. Monoclonal mouse anti-human Cytokeratin (Clone AE1/AE3, Dako), monoclonal mouse anti-Vimentin (Clone V9, Dako), and monoclonal mouse anti-αSMA (Clone 1A4,

Dako) antibodies were used at a dilution of 1:100 as per company specifications. The remainder of the protocol was performed as specified using a HRP/DAB detection kit (EXPOSE Mouse and Rabbit Specific HRP/DAB Detection IHC kit, Abcam, Cambridge, Massachusetts, USA).

*Quantitative Real-time PCR*

Total RNA was isolated from cells using TRIzol (Invitrogen). cDNA was prepared by reverse transcription with M-MuLV Reverse Transcriptase (New England Biolabs Inc, Ipswich, Massachusetts, USA). mRNA expression was measured using quantitative real-time PCR on a high-throughput ABI Prism 7900HT real-time instrument (Applied Biosystems, Life Technologies, Carlsbad, California, USA) using SYBR Green PCR Master Mix (Applied Biosystems) as described previously (51). A paired, two-tailed student's t-test was used to determine significance of changes compared with the control sample. Significance was set as $p < 0.05$.

*FT-IR imaging and data analysis*

Paraffin-embedded samples were sectioned at 5 µm onto MirrIR IR-reflective glass slides (Kevley Technologies, Chesterland, Ohio, USA). Once dry, samples were deparaffinized in hexanes for 24 h and then air-dried completely before imaging. For FT-IR imaging, a PerkinElmer Spotlight 400 (PerkinElmer, Waltham, Massachusetts, USA) equipped with a thermal source and a raster-scanning linear array detector was used with a Germanium ATR imaging accessory. An NB medium apodization was applied, a 1 cm $s^{-1}$ mirror speed was used for acquisition, and zeropadding was not used. Background scans were taken at 8 $cm^{-1}$ spectral resolution. 150 x 150 µm images were collected at 8 $cm^{-1}$ spectral resolution with 16 scans per pixel and a 1.56 x 1.56 µm pixel size. Data were atmospheric and ATR corrected on the Spotlight, and further processing was done using ENVI-IDL (Exelis Visual Information Solutions, Boulder, Colorado, USA). A minimum noise fraction (MNF) algorithm was applied on all images (52) to reduce noise in the data. Two regions were imaged per sample, and samples were prepared in duplicate (for a total of 4 data sets per condition).

**References**


1. Jemal A. *et al*. (2011) Global cancer statistics. *CA Cancer J Clin* **61**(2): 69-90.
2. Debnath J., Muthuswamy S.K., and Brugge J.S. (2003) Morphogenesis and oncogenesis of MCF-10A mammary epithelial acini grown in three-dimensional basement membrane cultures. *Methods* **30**(3): 256-268.

3. Birgersdotter A., Sandberg R., and Ernberg I. (2005) Gene expression perturbation in vitro – A growing case for three-dimensional (3D) culture systems. *Semin Cancer Biol* **15**(5): 405-412.
4. Martin K.J., Patrick D.R., Bissell M.J., and Fournier M.V. (2008) Prognostic breast cancer signature identified from 3D culture model accurately predicts clinical outcome across independent datasets. *PLoS ONE* **3**(8): e2994.
5. Fischbach C., *et al.*(2007) Engineering tumors with 3D scaffolds. *Nature Methods* **4**: 855-860.
6. Weaver V.M., *et al*. (1997) Reversion of the malignant phenotype of human breast cells in three-dimensional culture and in vivo by integrin blocking antibodies. *J Cell Biol* **137**(1): 231-245.
7. Wang F. *et al.* (1998) Reciprocal interactions between β1-integrin and epidermal growth factor receptor in three-dimensional basement membrane breast cultures: A different perspective in epithelial biology. *Proc Natl Acad Sci USA* **95**(25): 14821-14826.
8. Avvisato C.L., *et al*. (2007) Mechanical force modulates global gene expression and β-catenin signaling in colon cancer cells. *J Cell Sci* **120**: 2672-682.
9. Paszek M.J. *et al*. (2005) Tensional homeostasis and the malignant phenotype. *Cancer Cell* **8**(3): 241-254.
10. Krause S., Maffini M.V., Soto A.M., and Sonnenschein C. (2008) A novel 3D *in vitro* culture model to study stromal-epithelial interactions in the mammary gland. *Tissue Eng Part C Methods* **14**(3): 261-271.
11. Muthuswamy S.K., Li D., Lelievre S., Bissell M.J., and Brugge J.S. (2001) ErbB2, but not ErbB1, reinitiates proliferation and induces luminal repopulation in epithelial acini. *Nat Cell Biol* **3:** 785-792.
12. Anderson L.R., Sutherland R.L., and Butt A.J. (2010) BAG-1 overexpression attenuates luminal apoptosis in MCF-10A mammary epithelial cultures through enhanced RAF-1 activation. *Oncogene* **29**(4): 527-538.
13. Pickl M. and Ries C.H. (2009) Comparison of 3D and 2D tumor models reveals enhanced HER2 activation in 3D associated with an increased response to Trastuzumab. *Oncogene* **29**: 461-468.
14. Polo M.L., *et al*. (2010) Responsiveness to PI3K and MEK inhibitors in breast cancer. Use of a 3D culture system to study pathways related to hormone independence in mice. *PLoS One* **5**(5): e10786.
15. Liotta L.A., and Kohn E.C. (2001) The microenvironment of the tumor-host interface. *Nature* **411**: 375-379.

16. Allinen M., *et al*. (2004) Molecular characterization of the tumor microenvironment in breast cancer. *Cancer Cell* **6:** 17-32.
17. Ma, X., *et al*. (2009) Gene expression profiling of the tumor microenvironment during breast cancer progression. *Breast Cancer Res* **11**: R7.
18. Zian B.Z. and Pollard J.W. (2010) Macrophage diversity enhances tumor progression and metastasis. *Cell* **141**(1): 39-51.
19. Nieman K.M., Romero I.L., Van Houten B., and Lengyel E. (2013) Adipose tissue and adipocytes support tumorigenesis and metastasis. *Biochim Biophys Acta* http://dx.doi.org/10.1016/j.bbalip.2013.02.010.
20. Bhowmick N.A., Neilson E.G., and Moses H.L. (2004) Stromal fibroblasts in cancer initiation and progression. *Nature* **432**: 332-337.
21. Sung K.E., *et al*. (2011) Transition to invasion in breast cancer: a microfluidic *in vitro* model enables examination of spatial and temporal effects. *Integr Biol* **3:** 439-450.
22. Shipitsin M. and Polyak K. (2008) The cancer stem cell hypothesis: in search of definitions, markers, and relevance. *Laboratory Investigation* **88:** 459-463.
23. Rønnov-Jessen L., Peterson O.W., and Bissell M.J. (1996) Cellular changes involved in conversion of normal to malignant breast: importance of the stromal reaction. *Physiol Rev* **76**: 69-125.
24. Rønnov-Jessen L., *et al*. (1995) The origin of the myofibroblasts in breast cancer. Recapitulation of tumor environment in culture unravels diversity and implicates converted fibroblasts and recruited smooth muscle cells. *J Clin Invest* **95**: 859-873.
25. Holton S.E., Walsh M.J., Kajdacsy-Balla A., and Bhargava R. (2010) Label-free characterization of cancer-activated fibroblasts using infrared spectroscopic imaging. *Biophysical Journal* **101**(6): 1513-1521.
26. Holton S.E., Walsh M.J., and Bhargava R. (2010) Subcellular localization of early biochemical transformations in cancer-activated fibroblasts using infrared spectroscopic imaging. *Analyst* **136**(14): 2953-2958.
27. Lazard D., *et al* (1993) Expression of smooth muscle-specific proteins in myoepithelium and stromal myofibroblasts of normal and malignant human breast tissue. *Proc Natl Acad Sci USA* **90:** 999-1003.
28. Wood L.D., *et al* (2007) The genomic landscapes of human breast and colorectal cancers. *Science* **318**(5853): 1108-1113.

29. Kitano H. (2004) Cancer as a robust system: implications for anticancer therapy. *Nat Reviews Cancer* **4:** 227-235.
30. Bhargava, R. (2013) Infrared spectroscopic imaging: The next generation. *Appl Spectrosc* **66**(10): 1091-1120.
31. Sung K.E., *et al*. (2009) Control of 3-dimensional collagen matrix polymerization for reproducible human mammary fibroblast cell culture in microfluidic devices. *Biomaterials* **30:** 4833-4841.
32. Sappino A.P., Schruch W., and Gabbiani G. (1990) Differentiation repertoire of fibroblastic cells: Expression of cytoskeletal proteins as a marker of phenotypic modulations. *Lab Invest* **63**: 144-161.
33. Desmoulière A., Geinoz A., Gabbiani F., and Gabbiani G. (1993) Transforming growth factor-beta 1 induces alpha-smooth muscle actin expression in granulation tissue myofibroblasts and in quiescent and growing cultured fibroblasts. *J Cell Biol* **122**(1): 103-111.
34. Ruohola J.K., *et al*. Enhanced invasion and tumor growth of fibroblast growth factor 8b-overexpressing MCF-7 human breast cancer cells. *Cancer Res* **61**: 4229-4237.
35. Hanahan D. and Weinberg R.A. (2011) Hallmarks of cancer: the next generation. *Cell* **144**(5): 646-674.
36. Gerdes J., *et al* (1984) Cell cycle analysis of a cell proliferation associated human nuclear antigen defined by the monoclonal antibody Ki67. *J Immunol* **133**: 1710-1715.
37. Rojas A., *et al* (2011) IL-6 promotes prostate tumorigenesis and progression through autocrine cross-activation of IGF-IR. *Oncogene* **30**: 2345-2355.
38. Onder T.T., *et al*. (2008) Loss of E-cadherin promotes metastasis via multiple downstream transcriptional pathways. *Cancer Res* **68**: 3645-3654.
39. Huber M.A., Kraut N., and Beug H. (2005) Molecular requirements for epithelial-mesenchymal transition during tumor progression. *Curr Opin Cell Biol* **17**(5): 548-558.
40. Cano A., *et al*. (2000) The transcription factor Snail controls epithelial-mesenchymal transitions by repressing E-cadherin expression. *Nature Cell Biol* **2**76-83.
41. Holton S.E. and Bergamaschi A., *et al*. (2013) Integrating molecular profiling and chemical imaging to elucidate fibroblast-epithelial interactions and therapy resistance in breast cancer. *Submitted to Integrative Biology July 2013*.
42. Gazi E. *et al.* (2009) A FTIR microspectroscopic study of the uptake ane metabolism of isotopically labelled fatty acids by metastatic prostate cancer. *Vib Spectrosc* **50**(1): 99-105.

43. Adam L., *et al*. (1994) Selective interactions between mammary epithelial cells and fibroblasts in co-culture. *Int J Cancer* **59**(2): 262-268.
44. Shimazaki J., *et al*. (2013) In patients with colorectal cancer, preoperative serum interleukin-6 level and granulocyte/lymphocyte ratio are clinically relevant biomarkers of long-term cancer progression. *Oncology* **84**(6): 356-361.
45. Chang C.H., *et al*. (2013) Circulating interleukin-6 level is a prognostic marker for survival in advanced nonsmall cell lung cancer patients treated with chemotherapy. *Int J Cancer* **132**(9): 1977-1985.
46. Yokoe T., Iino Y., and Morishita Y. (2000) Trends of IL-6 and IL-8 levels in patients with recurrent breast cancer: preliminary report. Breast Cancer **7**(3): 187-190.
47. Salgado R., *et al*. (2003) Circulating interleukin-6 predicts survival in patients with metastatic breast cancer. *Int J Cancer* **103**(5): 642-646.
48. Zhang G.J. and Adachi I. (1999) Serum interleukin-6 levels correlate to tumor progression and prognosis in metastatic breast carcinoma. *Anticancer Res* **19**(2B): 1427-1432.
49. Sullivan N.J., *et al*. (2009) Interleukin-6 induces an epithelial-mesenchymal transition phenotype in human breast cancer cells. *Oncogene* **28**: 2940-2947.
50. Bourhis, X.D., *et al*. (1997) Effect of stromal and epithelial cells derived from normal and tumorous breast tissue on the proliferation of human breast cancer cell lines in co-culture. *Int J Cancer* **71**(1): 42-48.
51. Frasor J*., et al.* Gene expression preferentially regulated by tamoxifen in breast cancer cells and correlations with clinical outcome. *Cancer Res* **66**(14), 7334-7340 (2006).
52. Reddy R.K. & Bhargava R. Accurate histopathology from low signal-to-noise ratio spectroscopic imaging data. *Analyst* **135**(11), 2818-2825 (2010).

## CHAPTER THREE: INTEGRATING MOLECULAR PROFILING AND CHEMICAL IMAGING TO UNDERSTAND HETEROTYPIC INTERACTIONS IN COMPLEX SAMPLES


### Abstract

The tumor microenvironment is known to play a role in promoting cancer phenotypes and has been suggested as a potential therapeutic target. Its influence on therapeutic resistance and cancer relapse, however, is poorly understood. Here we investigate the interaction of mammary fibroblasts and estrogen receptor-positive breast cancer cells in a three-dimensional culture model and characterize the secreted protein factors involved in the cellular cross-talk. We show that fibroblasts induce an epithelial-to-mesenchymal transition in the cancer cells, leading to hormone-independent growth, invasive phenotypes, and resistance to endocrine therapy. We use two technologies that may translate these conclusions from cell culture to patient samples: a secreted protein signature to stratify patient populations and label-free chemical imaging to study cellular hormone response. Our findings underscore the role of fibroblasts in promoting therapeutic resistance and highlight the use of novel approaches for the dynamic molecular subtyping of breast cancer.

**Introduction**

More than 70% of breast cancers diagnosed in the US are estrogen receptor positive ($ER^+$) (1, 2). $ER^+$ tumors generally have more favorable prognoses compared to other subtypes and can be treated with targeted endocrine therapies, for example, with tamoxifen (3). Though most $ER^+$ patients respond favorably to targeted therapy, up to 30% of treated cancers recur (3, 4). For patients with recurrent systemic disease, the five-year survival rate drops to 20%, with a median survival of 12-24 months (5). The factors underlying recurrence arising from endocrine resistance are not fully understood, but it is increasingly appreciated that the microenvironment of the tumor cells can play a critical role in impacting their behavior (6, 7).

To gain a fundamental understanding of the molecular factors driving endocrine resistance and tumor recurrence, which cannot be fully elucidated *in situ* in humans, we have developed and employed cell culture models described herein. We hypothesized that normal fibroblasts serve at the frontline of heterotypic interactions experienced by cancer cells; not only are they the first line of defense presented by the body to dysplasia, they are also encountered in the microenvironment during every stage of disease progression. It is also now clear that three-dimensional (3D) cultures represent a more realistic model for tumors (8). While excellent 3D tumor models have been proposed (9, 10), 3D co-cultures to study heterotypic interactions are less widely used (11, 12). Hence, we developed and employed a series of 3D co-culture systems to specifically and comprehensively investigate molecular epithelial-fibroblast interactions. In particular, we examined the impact of fibroblasts on tumor cell phenotypes and endocrine therapy responsiveness. We sought to obtain a molecular interaction signature (iSig) of differential epithelial-stromal interactions that characterizes the microenvironment-influenced cancerous phenotype. The iSig is not only important for mechanistic insight into tumor progression but may provide an immediate route to characterizing the dynamics of tumor behavior. The efficacy of our dynamic iSig approach in predicting patient breast cancer outcome was compared to available gene expression profiling studies.

In addition to examining cell phenotype using several molecular approaches, we incorporated a comprehensive profiling approach based on chemical imaging. As opposed to molecular imaging that measures only a few epitopes, emerging chemical imaging technologies use spectroscopy to provide functional and molecular information within cells and tissues without requiring staining or *a priori*

knowledge of molecular transformations. Here we employ Fourier Transform infrared (FT-IR) spectroscopic imaging (13) for rapid and label-free profiling of co-culture samples. By visualizing the inherent chemistry within a sample, cell activity changes and disease states *in vitro* (14, 15) and cell types within complex tissues (16-18) can be monitored. Although a number of studies have reported the development of high performance imaging, rapid data processing and classification algorithms, as well as applications to histologic analyses of tissues (19-22), few studies have related spectral data to underlying molecular transformations. To our knowledge, no studies have related the spectroscopic monitoring of tissues to underlying biological processes that drive tumor behavior – a concept that is developed here.

In summary, we have monitored changes in gene expression and phenotypes arising from epithelial-fibroblast interactions and included FT-IR spectroscopy in a "bottom up" approach to understand the specific influence of stromal fibroblasts on breast cancer phenotypes. The first part of this study reports the step-wise validated development of the 3D co-culture model and the molecular and spatial information that is available from it. The second set of results focuses on molecular transformations and describes a secreted protein interaction signature that effectively predicts patient clinical outcomes. In the third set of results, we develop the chemical imaging signature of the underlying genomic states in endocrine responsive breast cancer. Together, these approaches provide a toolbox for understanding key aspects of breast cancer evolution and highlight a pivotal role for mammary fibroblasts in the tumor cell microenvironment in determining endocrine sensitivity or loss of response in breast cancer cells.

**Results**

*3D culture systems were engineered to simulate epithelial-fibroblast interactions*

The four models shown schematically in Figure 3.1*A* and 3.1*B* allowed us to systematically simulate the microenvironmental influence on cancer cells as well as easily obtain material to analyze for the molecular signature of this interaction (Fig. 3.1*C* and 3.1*D*). MCF-7 breast cancer cells were grown in 3D on Matrigel, which is denoted hereon simply as MCF-7. The influence of fibroblasts was varied by geometry. A sandwich culture (MCF-7$^{S}$) represents the compartmentalization of cancer cells and fibroblast-rich stroma, as may be observed in confined human tumors. Fibroblasts are embedded in a type I collagen matrix and grown in a separate layer. Cells are able to communicate continuously via

molecular diffusion of soluble factors but do not migrate out of their respective layers (14). After a prescribed co-culture time, the layers are easily separated, and molecular analyses can be performed without any cell crossover. The mixed culture (MCF-$7^{M}$) has cells mixed together before they are plated, allowing for cell-cell interactions arising from direct contact. Finally, to understand the transient influence of soluble factors, the conditioned medium (CM) culture consists of medium from MCF-$7^{M}$ added to the MCF-7 cells. This medium is also analyzed separately for soluble factors. In all situations, MCF-7 cells grew as spheroids. A combination of these models comprehensively interrogates the differential fibroblast-cancer cell interactions that influence cancer progression.

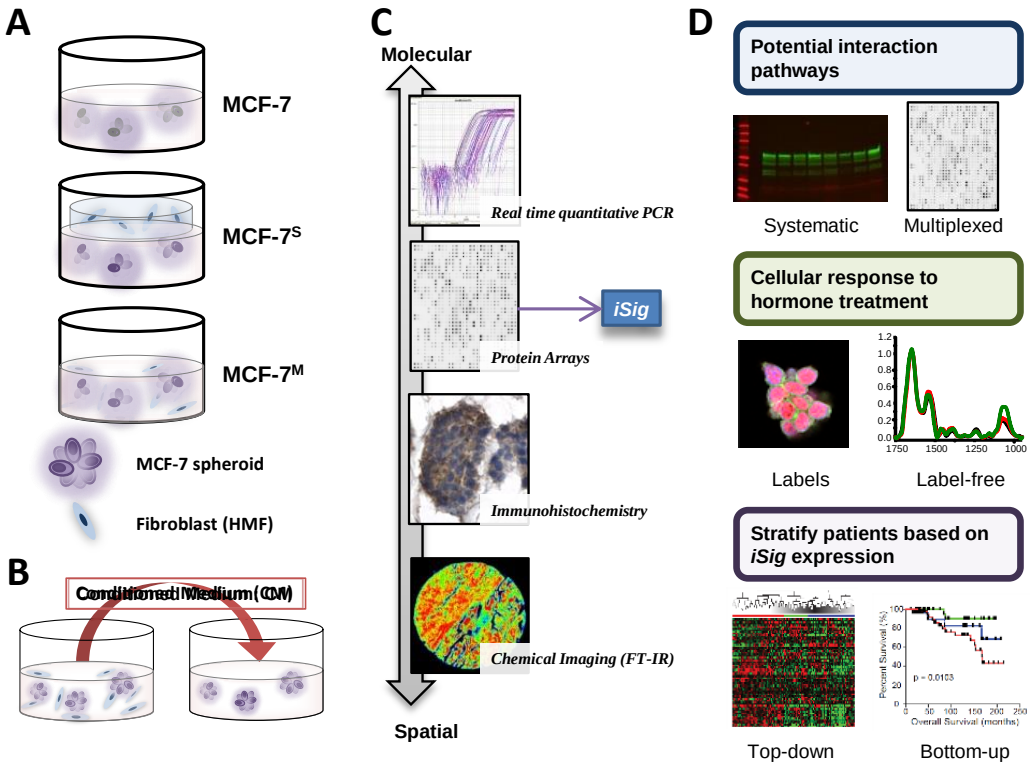


**Figure 3.1: Three-dimensional co-culture models and analytical approaches in this study.**

We utilized several three-dimensional co-culture models to study the interactions between MCF-7 breast cancer cells and primary mammary fibroblasts. The MCF-7 were grown as spheroids in a Matrigel overlay culture. Fibroblasts were incorporated either in a direct-contact mixed culture (MCF-$7^{M}$) or in a separate collagen layer in a sandwich culture (MCF-$7^{S}$). To study the effects of paracrine signaling, conditioned medium (CM) studies were done in which CM was taken from the mixed culture and used to treat MCF-7 or normal mammary epithelial cells (HMEC) grown alone. The CM was also profiled using protein arrays. We used gene expression and phenotypic assays to study response to hormone and the expression of markers of EMT. This molecular profiling approach was correlated to label-free FT-IR spectroscopic imaging and also gene expression from patient samples.

*Fibroblasts induce an EMT in cancer cells*

Because the epithelial-to-mesenchymal transition (EMT) in breast cancer cells has been associated with a loss of $E_2$/ERα signaling and insensitivity to endocrine therapies (23, 24), we hypothesized that co-culture with HMF might induce an EMT phenotype. Epithelial cells from MCF-$7^S$ displayed increased levels of SNAIL (7-fold) and SLUG (25-fold) mRNA that were correlated with a 4-fold decrease of E-Cadherin mRNA (Fig. 3.2), all characteristic of the mesenchymal cell phenotype and hallmarks of EMT (25). These effects observed at 3 days were sustained at longer times, indicating that the induced EMT phenotype is not transient. The observed phenotype was accompanied by an increase in mRNA levels for growth factors, including amphiregulin (Figure 3.3), which is associated with a loss of ER and increased inflammatory signaling in breast cancers (26, 27). These data suggest that EMT is observed and that hormone-independent proliferation of $ER^+$ cells may be linked to EMT.

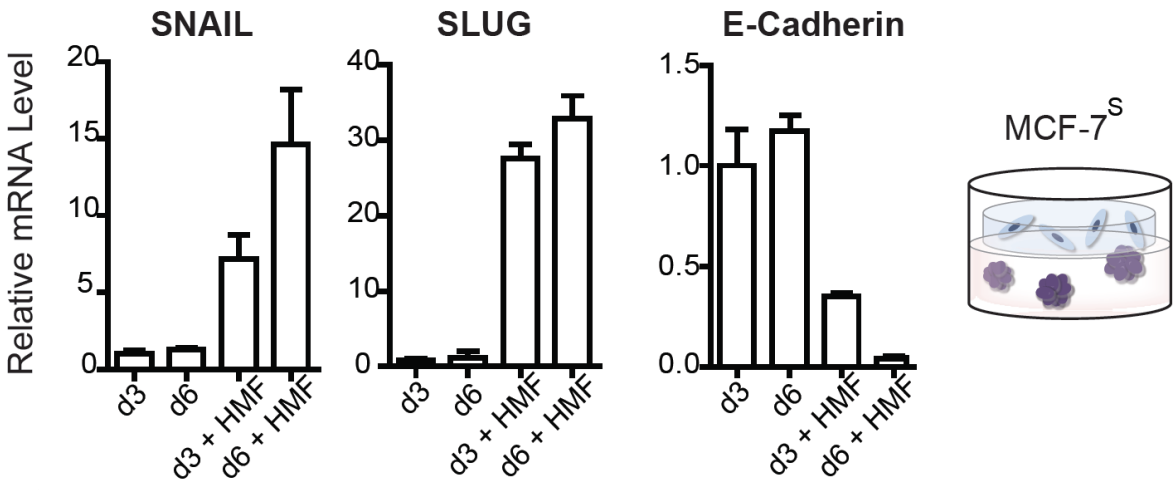


**Figure 3.2: Mammary fibroblasts induce an epithelial-to-mesenchymal transition in $ER^+$ breast cancer cells in 3D culture.** Over the course of 6 days in the sandwich co-culture, MCF-$7^S$ display increased mRNA levels of EMT markers SNAIL and SLUG with a downstream decrease in E-cadherin mRNA

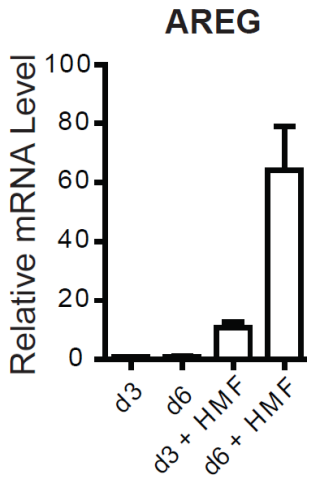


**Figure 3.3: Amphiregulin mRNA expression is increased in MCF-7 breast cancer cells in the sandwich co-culture.**

To confirm that the phenotypic changes in MCF-7$^{S}$ were due to fibroblast signaling and not dependent on the sandwich geometry, we employed the MCF-7$^{M}$ culture. Similar to MCF-7 and MCF-7$^{S}$, spheroids were still obtained in MCF-7$^{M}$, with fibroblasts at spheroid perimeters but not inside the spheroids (Figure 3.4). Two seeding compositions were utilized for MCF-7$^{M}$, consisting of fibroblast:epithelial cell ratios of 1:5 (indicating a 'low density' of fibroblasts) and 1:3 (indicating a 'high density' of fibroblasts). Although in these MCF-7$^{M}$ cultures SNAIL and SLUG mRNAs were expressed at a much higher levels and E-cadherin levels were decreased 2-fold or more compared to MCF-7$^{S}$ (Figure 3.5), a density-dependent level is observed between the low and high fibroblast ratios. Because RNA was extracted for both cell types in the mixed co-culture, mRNA levels for these markers from HMF grown alone are also displayed. HMF basal mRNA levels of SNAIL and SLUG were elevated compared to MCF-7, but this basal level is only approximately 30% the level observed in the co-culture, suggesting that regulation of the EMT phenotype is synergistic and not dominated by one cell type. Reduction in E-cadherin mRNA levels was also confirmed for the protein using immunohistochemical staining (Figure 3.6). Demonstrating that the presence of HMF also alters the behavior of cancer cells, MCF-7 grown in a Transwell co-culture with HMF were found to be significantly ($p=0.0045$) more invasive compared to naïve MCF-7 (Figure 3.7). Comparing the mixed and sandwich culture models, we observed that increasing both the co-culture time and increasing the relative number of fibroblasts in the co-culture induced similar trends in the gene expression of EMT markers in the cancer cells. These results indicate that paracrine signaling is sufficient for normal mammary fibroblasts to induce EMT and increase invasiveness in epithelial cells.

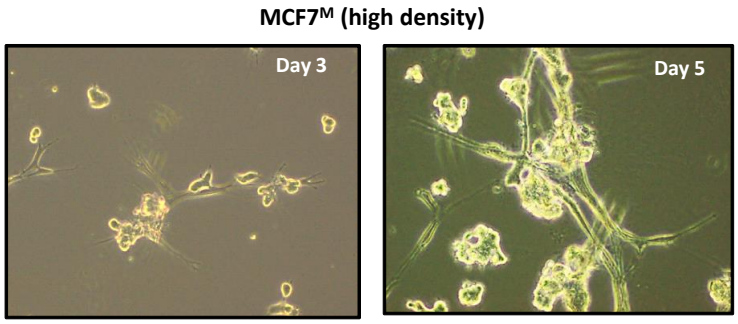


**Figure 3.4: Light microscopy image showing fibroblasts recruited to MCF-7 spheroids after 3 and 5 days in culture.**

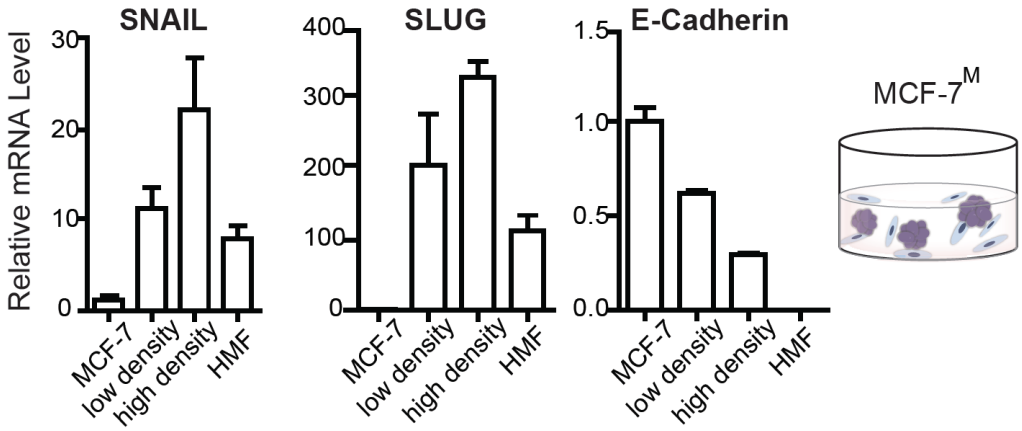


**Figure 3.5: A mixed co-culture was prepared at two fibroblast seeding densities, low- and high-density (relative to MCF-7).** EMT markers are seen as with the sandwich co-culture, and there is a dose-dependent response to the fibroblast presence.

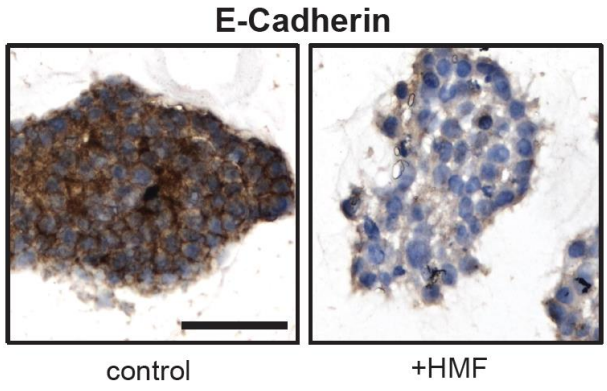


**Figure 3.6: Immunohistochemistry was used to confirm decrease in overall E-cadherin protein level and a dissociation of MCF-7M**

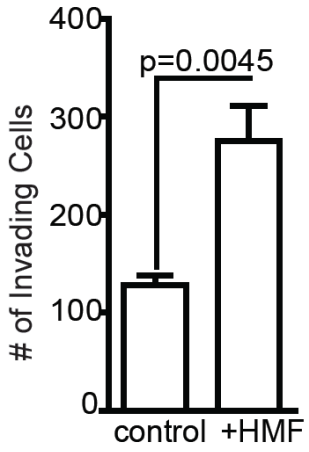


**Figure 3.7: co-culture with HMF significantly increases the invasive potential of MCF-7**

*Co-culture with mammary fibroblasts down-regulates cancer cell ERα and drives hormone-independent proliferation*

Due to the known correlation between EMT and insensitivity to endocrine therapy, we hypothesized that co-culture with fibroblasts might also alter response to hormones. Our model system presents an opportunity to understand how EMT affects endocrine sensitivity and how the microenvironment influences this phenomenon. As a prelude to using the culture systems for this effort, estrogen response in monolayer and 3D culture was confirmed to be similar although there are gross morphological differences between the different culture systems (Figure 3.8). A sustained and marked reduction in the mRNA level of ERα in MCF-$7^S$ was observed in co-culture (Figure 3.9). Though reduced in abundance, the remaining ERα in MCF-$7^S$ cells was functional, as shown by the induction of the $E_2$-responsive genes progesterone receptor (PR) and Ki67 mRNA after treatment with this hormone (Figure 3.10). However, while basal levels of Ki67 mRNA and cellular proliferation were increased in both co-cultures, after 6 days of co-culture response to $E_2$ was substantially diminished, suggesting that MCF-$7^S$/MCF-$7^M$ proliferation becomes increasingly hormone-independent (Figure 3.11). Accompanying this hormone-independent growth, tamoxifen (Tam) was no longer effective in inhibiting the growth of MCF-$7^M$ (Figure 3.12), implying that patients with specific stromal characteristics might not respond to these therapies, regardless of ER status.

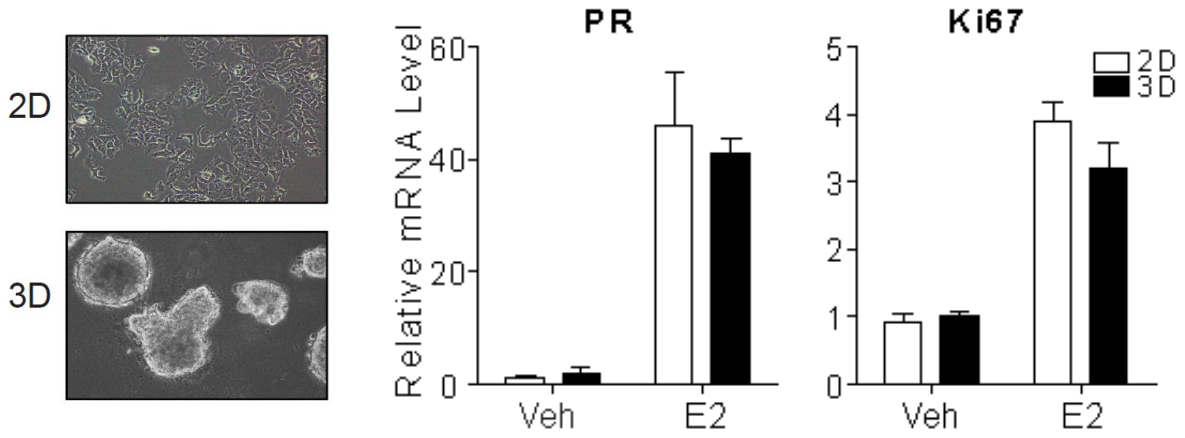


**Figure 3.8: Comparison of morphology and response to $E_2$ in 2D and 3D MCF-7 models.** Response of MCF-7 cells to $E_2$ stimulation is similar in 2D and 3D cultures as monitored by induction of $E_2$-response genes progesterone receptor (PR) and proliferation marker Ki67.

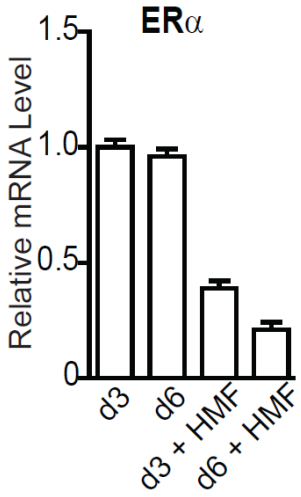


**Figure 3.9: Co-culture with human mammary fibroblasts down-regulates ERα and fosters hormone-independent growth of breast cancer cells.** Fibroblasts down-regulate ERα mRNA levels at 3 and 6 days and this effect increases with longer co-culture time

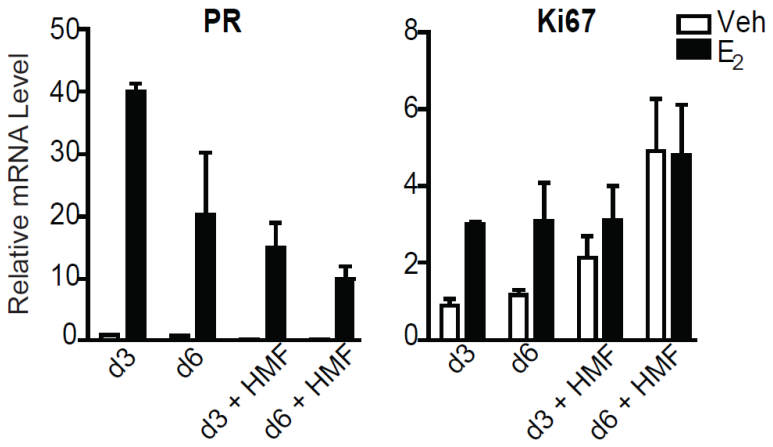


**Figure 3.10: HMF reduce the response of MCF-7 cells to $E_2$, as measured by PR and Ki67 mRNA levels at 3 and 6 days.**

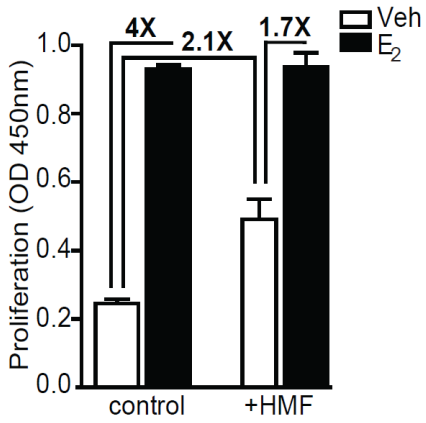


**Figure 3.11: Co-culture with HMF increases the basal proliferation rate of MCF-7, and decreases the effect of $E_2$ stimulation on proliferation monitored at 3 days.**

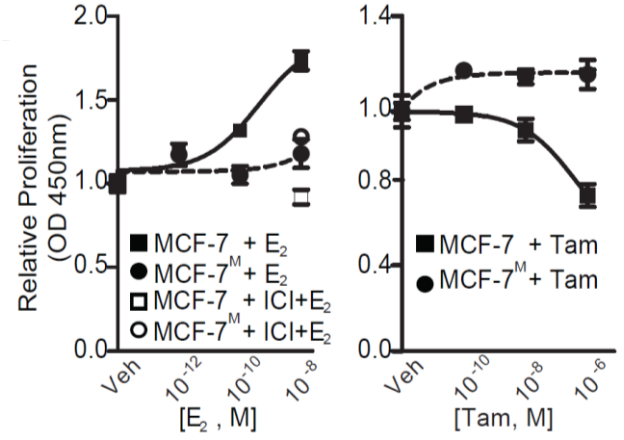


**Figure 3.12: MCF-$7^M$ proliferation fails to respond to increasing concentrations of $E_2$ (left panel) and MCF-$7^M$ growth is not inhibited by treatment with tamoxifen (right).** Response in MCF-7 cells alone is shown for comparison.

*Conditioned medium from 3D co-cultures induces EMT in breast cancer cells and also normal mammary epithelial cells*

After establishing above that fibroblast-epithelial interactions occur via paracrine signaling, we sought to elucidate the molecular components involved in greater detail by examining the culture medium. Conditioned medium (CM) was profiled using a protein array. Of the measured 507 proteins, 46 were found to be upregulated five-fold or greater compared to control (Table 3.1). Notably, many of the upregulated proteins were members of the matrix metalloproteinase family (MMPs), which has been previously implicated in aggressiveness of breast cancer cells (28) and in human tumor samples (29). Other identified proteins included growth factors and cytokines that play a role in recruiting cells involved in the inflammatory response. This finding implies that fibroblasts may serve to enhance the systemic response involving other cell types found at the periphery of and within tumors. Functional classification of the secreted proteins also showed enrichment in components of chemotaxis and ECM remodeling (Table 3.2). To further validate the sufficiency of soluble proteins in driving phenotypic changes, we examined gene expression changes in MCF-7 cells treated with CM (Figure 3.13). ERα levels were halved in treated samples, while EMT markers SNAIL and SLUG were highly upregulated with an almost complete loss of E-Cadherin mRNA, confirming that the changes observed are due to secreted factors.

**Table 3.1: Secreted proteins identified as being increased 5-fold or higher in CM derived from co-culture compared to medium from MCF-7 cells alone**

| Protein Name | |
|---|---|
| CCL14 / HCC-1 / HCC-3 | Musk |
| EDA-A2 | NAP-2 |
| ENA-78 | NOV / CCN3 |
| Endoglin / CD105 | Orexin B |
| FGF-8 | Osteoactivin / GPNMB |
| GCP-2 / CXCL6 | PD-ECGF |
| GRO | PDGF R alpha |
| IGF-I | PDGF R beta |
| IGF-I SR | PDGF – BB |
| IL-1 beta | RELM beta |
| IL-2 R gamma | SDF-1 / CXCL12 |
| Lck | Sgp130 |
| Latent TGF-beta bp1 | TGF-beta RII |
| Lymphotoxin beta R / TNFRSF3 | Thrombospondin-4 |
| M-CSF R | Thymopoietin |
| MFG-E8 | TIMP-3 |
| MIP 2 | TIMP-4 |
| MMP-1 | TRAIL R1 / DR4 / TNFRSF10A |
| MMP-3 | Trail R3 / TNFRSF10C |
| MMP-13 | VEGF R2 (KDR) |
| MMP-14 | VEGF-D |
| MMP-19 | WIF-1 |
| MMP-25 / MT6-MMP | XEDAR |

**Table 3.2: DAVID pathway association based on secreted protein signature**

| Networks | pValue | Genes from Active Data |
|---|---|---|
| Chemotaxis | 7.991E-11 | IL-1 beta, CCR2, GRO-3, Lck, CCL13, Galpha(q)-specific peptide GPCRs, Galpha(i)-specific peptide GPCRs, SDF-1, IL-16, CCL7, GRO-2, PD-ECGF (TdRPase), GCP2 |
| Proteolysis_ECM remodeling | 1.820E-09 | MMP-13, MMP-14, TIMP3, MMP-1, TIMP4, MMP-15, MMP-24, MMP-1, MMP-25, Stromelysin-1 |
| Inflammation_Jak-STAT pathway | 4.161E-09 | IL21R, CCR2, PDGF-R-beta, IL5RA, CCL13, PDGF receptor, IL-2R gamma chain, IL-21 receptor, SDF-1, IL10RA, IGF-1, CCL14, IL-20 |
| Proteolysis_Connective tissue degradation | 4.951E-08 | MMP-13, MMP-14, TIMP3, MMP-19, TIMP4, MMP-15, MMP-24, MMP-1, MMP-25, Stromelysin-1 |
| Cell adhesion_leukocyte chemotaxis | 9.863E-07 | CCR2, GRO-3, Lck, CCL13, Galpha(q)-specific peptide GPCRs, Galpha(i)-specific peptide GPCRs, SDF-1, CCL14, CCL7, GRO-2, GCP2 |
| Immune response_Th17-derived cytokines | 1.520E-06 | IL-1 beta, MMP-13, SDF-1, CCL7, RANKL(TNFSF11), GCP2, MMP-1, Stromelysin-1 |
| Development_Blood vessel morphogenesis | 2.810E-06 | IL-1beta, FGF8, Galpha(q)-specific peptide GPCRs, Galpha(i)-specific peptide GPCRs, MMP-19, SDF-1, ALK-2, VEGFR-2, TIE, PD-ECGF (TdRPase), VEGF-D |
| Cell adhesion_Platelet-endothelium-leukocyte interactions | 1.497E-05 | IL-1 beta, MMP-13, PDGF-R-beta, Endoglin, PDGF receptor, VEGFR-2, Thrombospondin 4, TGF-beta receptor type II, PDGF-R-alpha |
| Apoptosis_Anti-Apoptosis mediated by external signals via PI3K/AKT | 2.345E-05 | IL-1 beta, FGF8, PDGF-R-beta, PDGF receptor, GFRalpha1, IGF-1, VEGFR-2, NT-3, VEGF-D, PDGF-R-alpha |

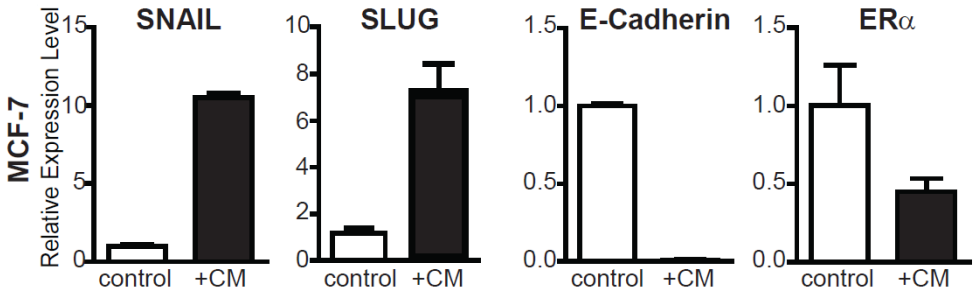


**Figure 3.13: Treatment of cancerous and normal primary mammary epithelial cells with conditioned medium (CM) promotes more aggressive phenotypes and reveals a mechanism of paracrine signaling.** Gene expression changes in MCF-7 cells treated with CM reveal a 10-fold increase in SNAIL, a 7-fold increase in SLUG, and elimination of detectable E-cadherin mRNA. The increase in EMT markers is accompanied by a down-regulation of ERα mRNA.

To examine whether the cancer cell-fibroblast interaction might also affect adjacent normal epithelium, we grew normal primary human mammary epithelial cells (HMEC) with CM before measuring gene expression changes. Strikingly, the same EMT phenotype was observed although changes in cell markers of EMT were less dramatically altered in these cells compared with MCF-7 (Figure 3.14). Based on these results, we propose that fibroblast-cancer cell interactions can induce an

EMT in nearby normal breast epithelial as well as cancer cells via soluble protein signaling. These novel observations imply that the fibroblast-cancer cell environment can impact the behavior of normal epithelium that may act in concert with other stimuli to initiate tumors or induce progression of both early and later stage epithelial tumor cells toward a more aggressive state.

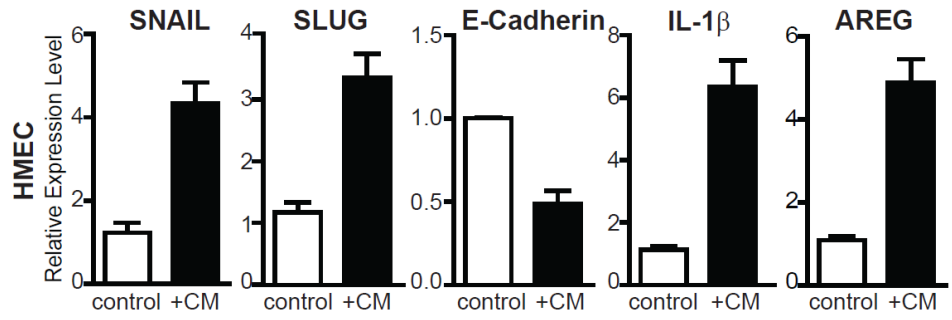


**Figure 3.14: After treatment of HMEC grown in monolayer culture with CM, there is an increase in gene expression related to EMT and growth factor release.** This suggests that paracrine effects of tumor cells can impact the phenotype of nearby normal mammary epithelial cells.

*Patients with high expression of the secreted protein signature are more likely to have poor clinical outcomes*

We hypothesized that our *in vitro* secreted protein signature may be correlated with poor outcome in breast cancer patients. We utilized a publicly available dataset (30) comprised of 109 patients diagnosed with Invasive Breast Cancer (IDC), pure Ductal Carcinoma *in Situ* (DCIS) or mixed diagnosis (IDC with a DCIS component) based on histology. Using the genes that code for the proteins identified to be upregulated on our screen, we clustered microarray data from primary tumors. Three primary patient clusters were found (Figure 3.15). The red cluster, characterized by elevated levels of MMPs and TGFβ, showed a significantly worse prognosis. Patients with high levels of the signature not only had a poor clinical outcome, but were also significantly more likely to be given an invasive ductal carcinoma (IDC) or 'mixed' histologic classification compared to DCIS. Further, we used ONCOMINE analysis to validate results across additional breast cancer datasets (31-34). This CM protein-derived signature was strongly correlated with invasion and poor prognosis, and was associated with the stroma in microdissected samples (Figures 3.16 and 3.17). The utility of this signature derived from cell culture models to stratify patient data based on gene expression suggests that after further work and validation, bottom-up protein signatures may prove useful for monitoring the dynamic states of tumor progression.

To our knowledge, this is the first study that utilizes a secreted protein signature to stratify breast cancer patient outcome.

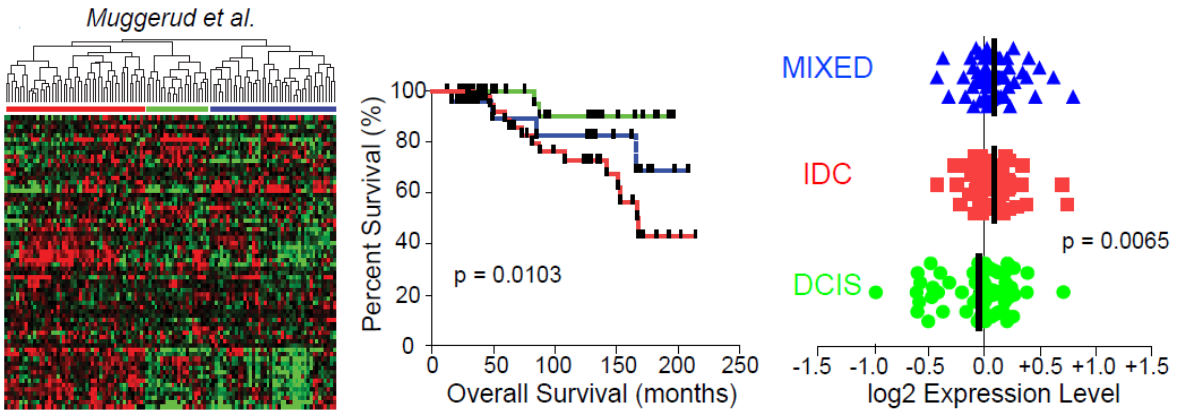


**Figure 3.15: Hierarchical clustering of breast cancer patient samples based on the secreted protein signature reveals novel subgroups.** Three classes can be distinguished, and survival analysis shows that patients in the red class (i.e. with higher gene expression of the signature secreted proteins) are significantly more likely to have poor outcomes, and are more likely to receive a diagnosis of invasive ductal carcinoma (IDC) compared to a mixed or ductal carcinoma *in situ* (DCIS) histological classification.

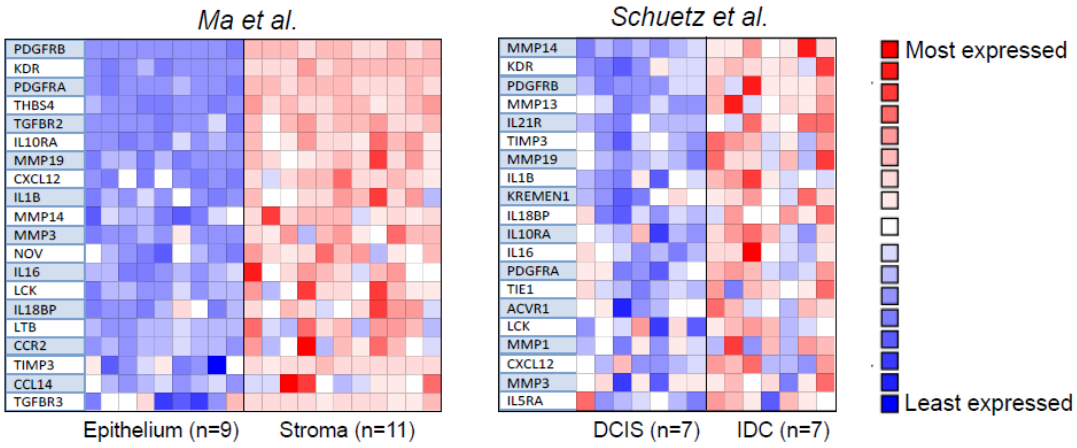


**Figure 3.16: ONCOMINE™ analysis shows that the protein signature is also overexpressed in IDC compared with DCIS in an independent dataset.** The protein signature is also significantly correlated with the stroma of breast tumors.

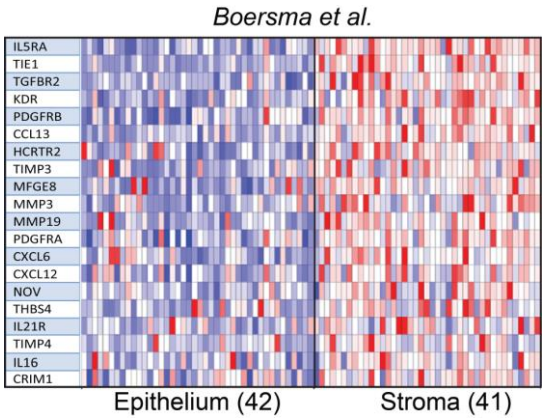


**Figure 3.17: Analysis of an independent dataset shows that high expression of the protein signature is correlated with the stroma.**

*Hormone response can be monitored using FT-IR spectroscopic imaging*

Our data show that ER function is dynamic and ER-positive cells may not respond to endocrine therapies if they have undergone EMT. Given the spatially-heterogeneous nature of tumors, an imaging technique to record this condition is needed. While IHC techniques can provide information about the presence of particular proteins, they do not reveal the function of these proteins. Further, antibody-based techniques are slow and not highly reproducible (35). Hence, we sought to apply a label-free imaging technique to our model 3D culture system. We used FT-IR imaging which combines microscopy to provide spatial information with spectral data that reveals a chemical measure of response of breast cancer cells to hormone or therapy. In MCF-7 cells after $E_2$ treatment, we observed a large increase in the C-H vibrational region of the spectrum (Figure 3.18), commonly associated with the $CH_2$ bending of fatty acids and lipids (36). These three bands (2960 $cm^{-1}$, 2930 $cm^{-1}$, and 2850 $cm^{-1}$) are also correlated with fatty acyl chain peroxidation (37). Similarly, the peak at 1080 $cm^{-1}$, associated with the phosphate backbone of nucleic acids and altered metabolic activity, is increased upon $E_2$ treatment. Thus, we have directly correlated absorption pattern changes with biological changes occurring in MCF-7 cells in response to treatment with $E_2$, a potent stimulator of proliferation in $ER^+$ cells. To our knowledge, the label-free imaging of this type of induced change in breast cancer has not been previously shown.

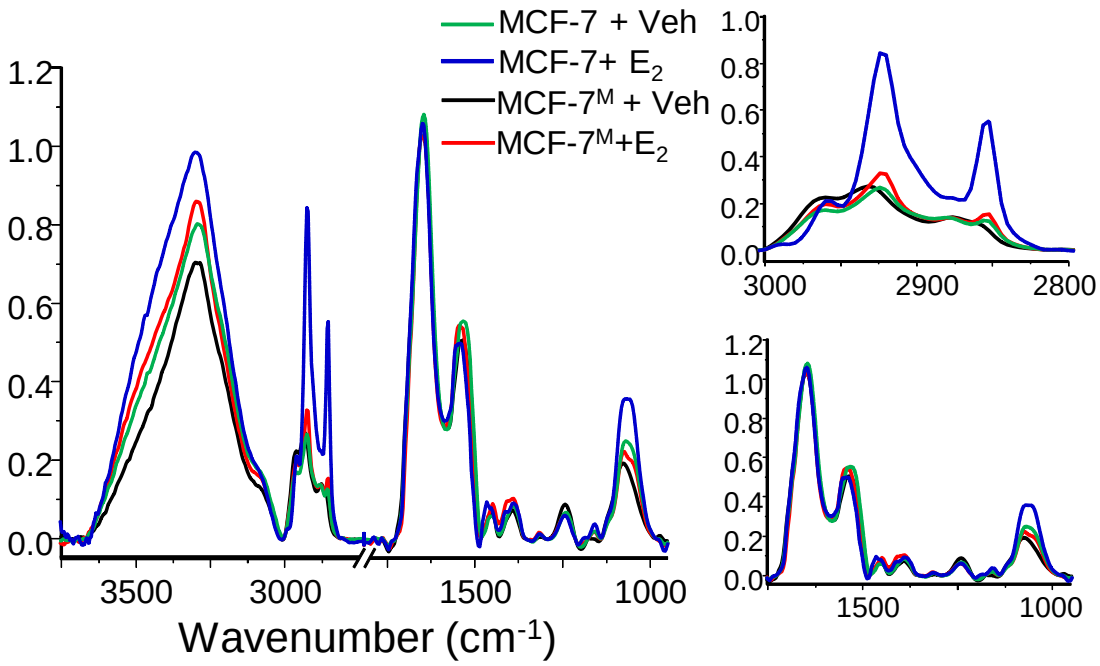


**Figure 3.18: Fourier transform-infrared (FT-IR) spectroscopic imaging can be used to monitor hormone response in ER$^+$ breast cancer cells.** A change in FT-IR spectroscopic imaging is seen in MCF-7 cells treated with estradiol ($E_2$), particularly in the C-H stretching region (3000 – 2750 cm$^{-1}$) and in the peak associated with nucleic acids (1080 cm$^{-1}$). However, when cells are co-cultured with HMF, the response to hormone is lost.

Next we sought to differentiate between cells having functionally active ER and those that do not. Samples from the mixed co-culture were imaged, and the average spectra upon treatment with $E_2$ were compared (Figure 3.18). Analysis of the spectra revealed that there was a loss of the chemical signature associated with $E_2$ response in the co-cultured samples, corresponding to the loss of ERα and ERα-mediated response in MCF-7$^M$. The fibroblast dose-response seen in mRNA levels was also apparent in IR spectra (Figure 3.19). The loss of $E_2$ response is also seen in the IR spectra of CM-treated samples, but to a lesser extent than with the direct co-culture (Figure 3.20). The chemical signature of $E_2$ treatment and its loss after co-culture with HMF in 3D culture reveals that FT-IR imaging may be useful in determining ER function in cells *in vitro*.

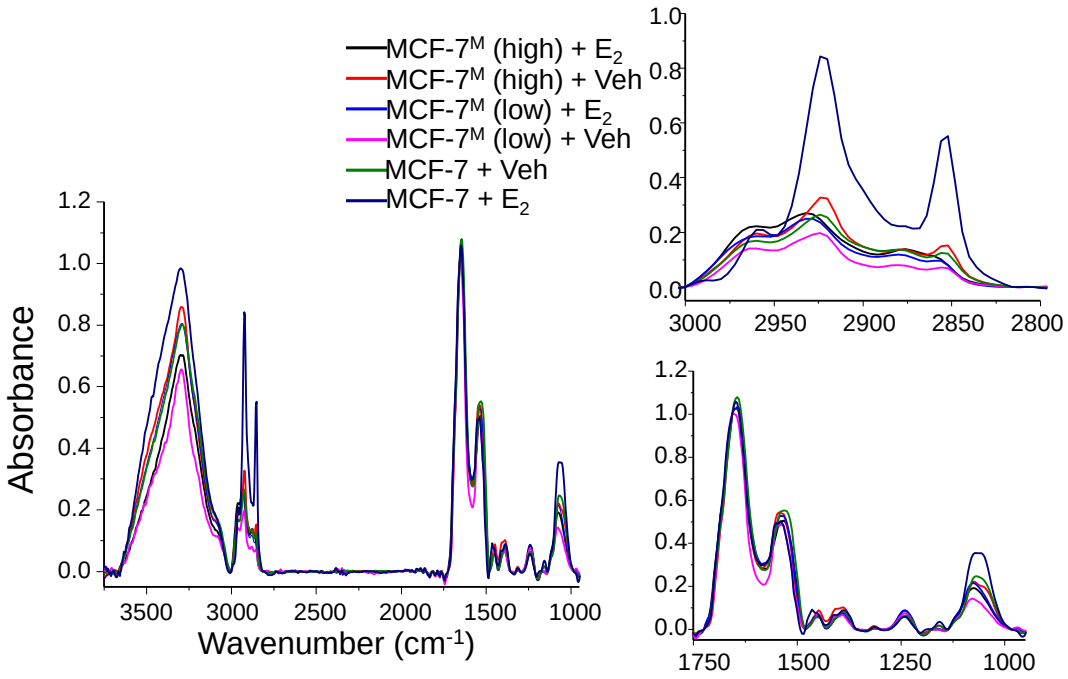


**Figure 3.19: The spectroscopic signature of $E_2$ response of MCF-7 cells is based on fibroblast density.**

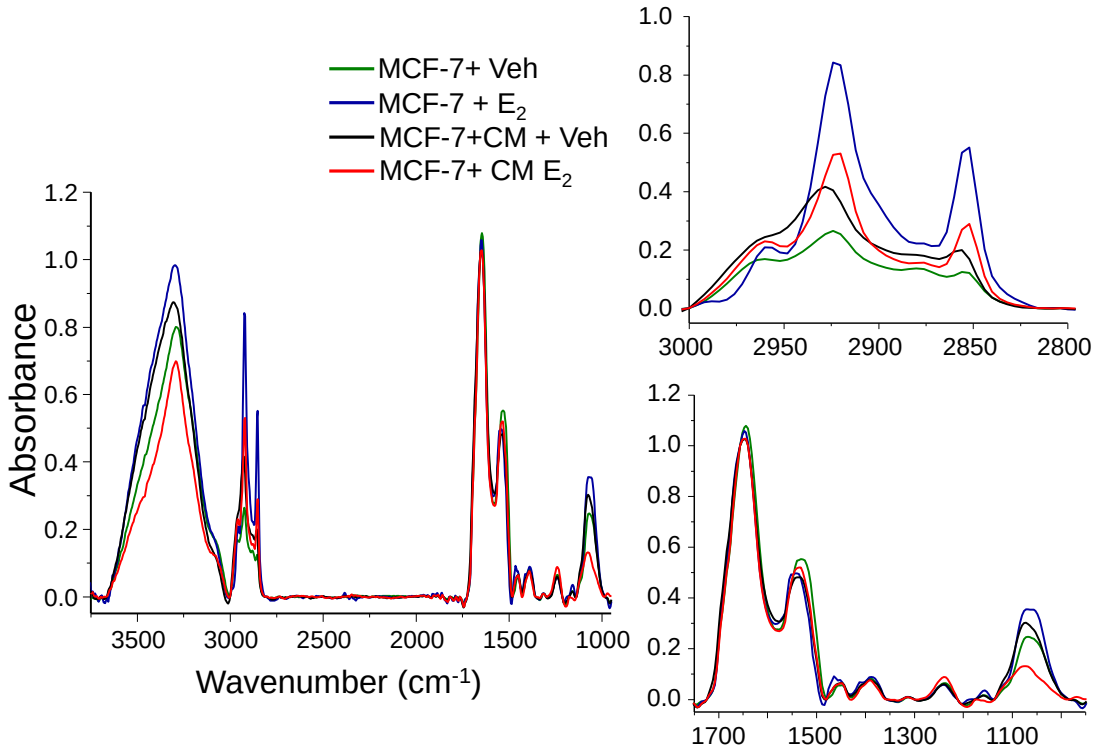


**Figure 3.20: The spectroscopic signature of $E_2$ response of MCF-7 cells is affected by treatment with CM, signifying that secreted factors can induce a similar change but this effect is reduced compared to co-culture.**

A spectral signature was also associated with response to tamoxifen (Tam) (Figure 3.21). There is a change in peaks in the C-H stretching region of the spectrum in MCF-7 after treatment with Tam, but the anti-proliferative effects of Tam are specifically seen at the 1080 $cm^{-1}$ peak. We have shown that the proliferation of MCF-$7^M$ is not inhibited by treatment with Tam using a cell-based proliferation assay, and here we correlate that specific phenotype to a spectral signature. While the 1080 $cm^{-1}$ peak is significantly decreased in MCF-7 after Tam treatment, the peak is unchanged in MCF-$7^M$. This label-free approach can be used to discriminate between cells that are responsive and those that are resistant to tamoxifen treatment.

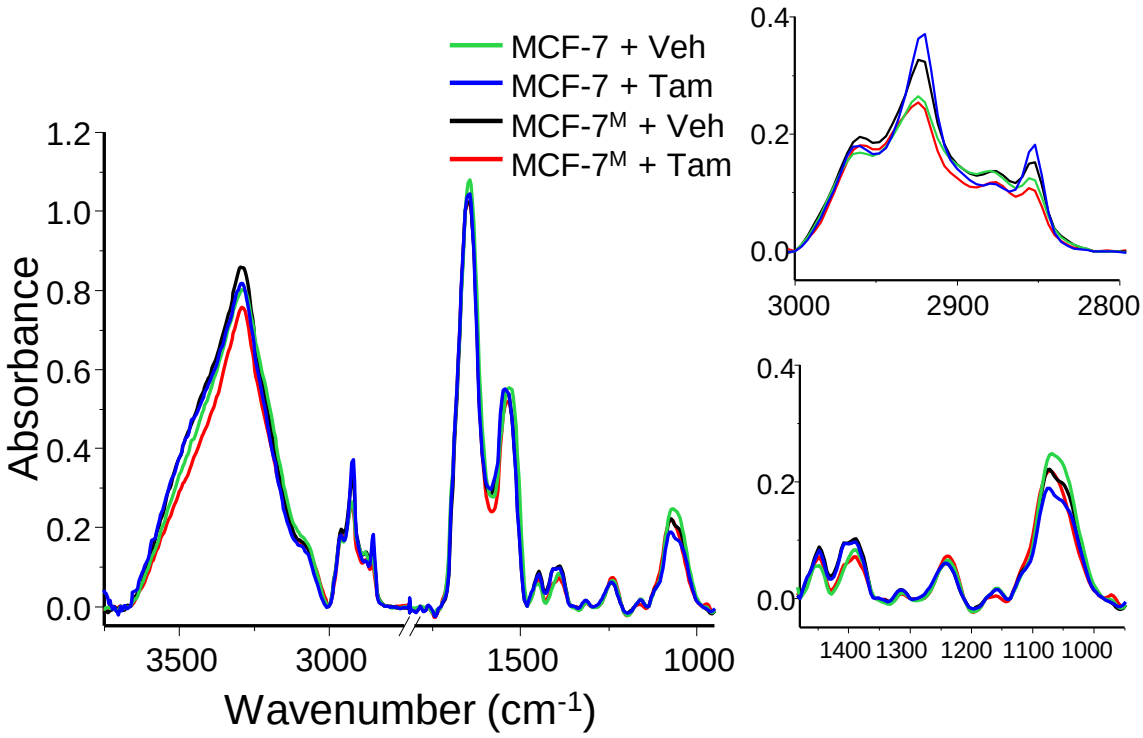


**Figure 3.21: FT-IR spectroscopic imaging can be used to monitor response to the endocrine therapy tamoxifen (Tam) in $ER^+$ breast cancer cells.** While there is a slight induction in peaks associated with the C-H stretching region upon treatment with Tam, the peak associated with nucleic acids, and therefore proliferation, is decreased in MCF-7 cells. This is correlated with the anti-proliferative effects of tamoxifen on $ER^+$ cells. In samples that have been co-cultured with HMF, this change is not seen at the 1080 $cm^{-1}$ peak, corresponding to the endocrine-resistant growth that was seen using proliferation assays.

Finally, we imaged human breast tissue microarrays (TMAs) containing samples from 148 patients in order to establish whether differences in ER status are apparent in clinical samples. Spectra

from the epithelium of IDC samples with high expression of ER (>80% of cells $ER^+$) were extracted and compared to IDC samples with low expression of ER (<20% of cells $ER^+$) (Figure 3.22). A Bayesian-type classifier was developed for the histologic discrimination of breast tissue using previously reported methods (16). The classifier was used to extract pixels corresponding to epithelium or fibroblast regions from breast cancer samples with varying levels of ER for this study and compared to determine signatures based on different cell types. Similar to the results observed for cellular changes in culture compared to tissues, several spectral markers can be translated from these 3D culture models to human tissue. In the epithelium (Figure 3.23), spectra from samples with high ER expression demonstrated similar absorbance in the C-H stretching region (3000 – 2825 $cm^{-1}$) to MCF-7 3D spheroid cultures and the overall absorbance in this region was higher than samples with low ER expression. Strikingly, significant spectral differences were observed in fibroblasts from tumors with different epithelial characteristics (Figure 3.24). These results suggest that IR may be used to identify features in the stromal compartment that are associated with long-term endocrine response. Spectroscopic differences between human breast tumor samples with varying levels of ER expression suggest that FT-IR spectroscopic imaging can complement IHC analysis by providing additional chemical information about the function of this nuclear hormone receptor in breast tumors.

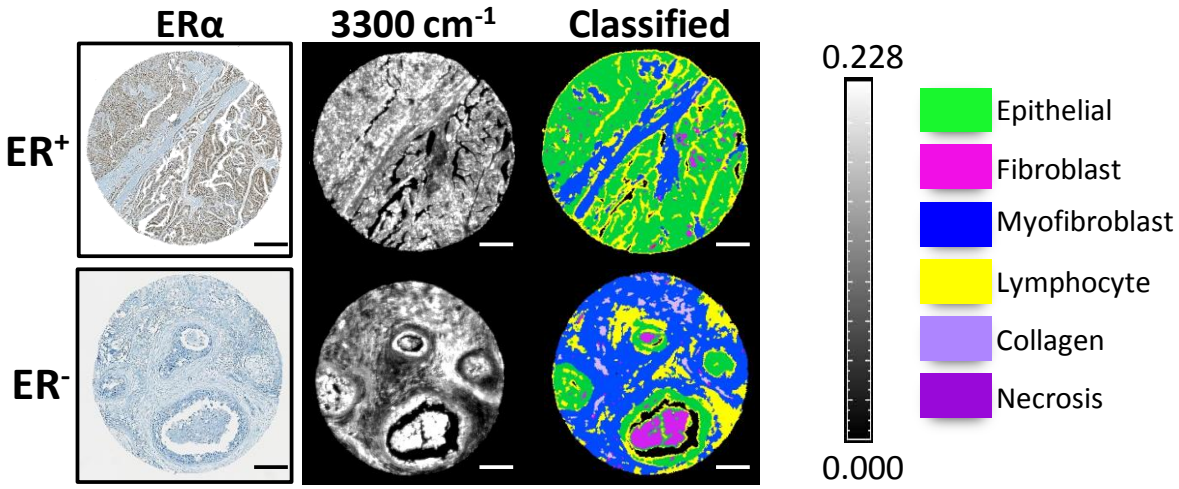


**Figure 3.22: Spectroscopic signatures determined using 3D co-culture models can be translated to human breast tissue samples.** Tissue microarray (TMA) biopsy cores (1.5 mm core diameter) were IHC stained for ERα and also imaged using FT-IR imaging (N-H/O-H band at 3300 $cm^{-1}$ visualized here for clarity). Images classified using Bayesian classifier are displayed as well to highlight the ability of FT-IR to discriminate between cell types in complex samples. Scale bar represents 250 µm.

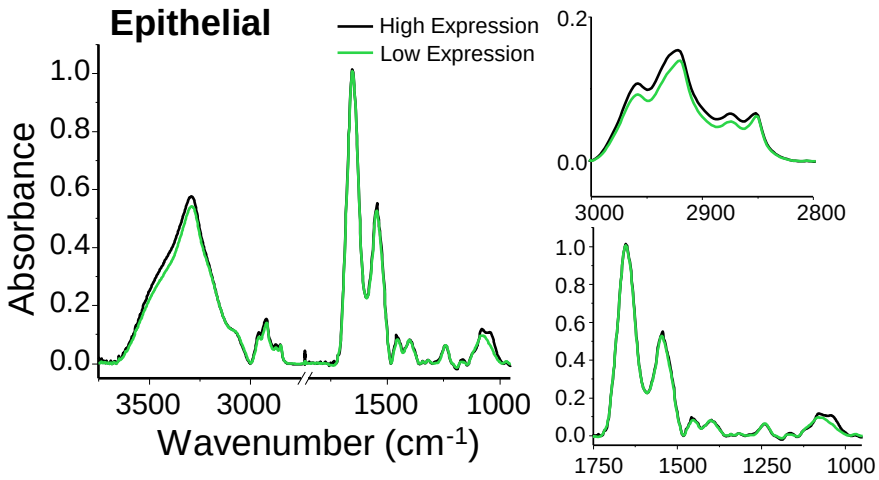


**Figure 3.23: Differences between epithelial pixels in patient samples with high (>80%) and low (<20%) expression of ERα can be seen in peaks at 1080 cm$^{-1}$ (phosphate) and 1030 cm$^{-1}$ (glycosidic bonds).** Full spectrum (3800 – 950 cm$^{-1}$), C-H stretching region (3000 – 2750 cm$^{-1}$), and biochemical fingerprint region (1750 – 950 cm$^{-1}$) are shown.

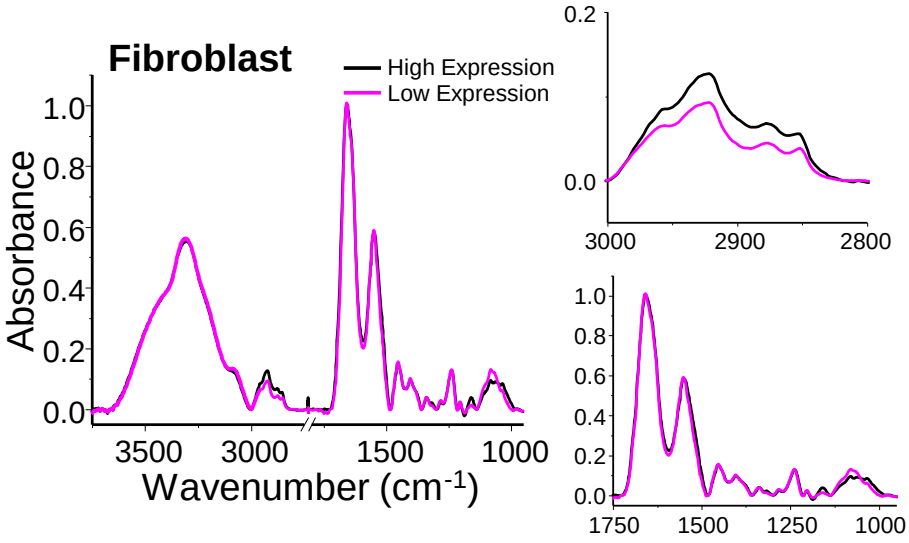


**Figure 3.24: Interestingly, in fibroblast-labeled pixels from patients with high or low ERα expression there are more apparent spectroscopic differences in the same regions.**

## Discussion

Our findings reveal that interactions of cancer cells with normal mammary fibroblasts induce hormone-independent growth and promote a more aggressive and invasive phenotype in breast cancer cells. Thus, fibroblasts alter the manner in which ER$^+$ cancer cells respond to hormones by reducing the role of estrogen in controlling proliferation and promoting a more rapidly proliferating hormone-

independent state. Importantly, the cross-over to hormone-independent growth is associated with an EMT phenotype, which has been previously correlated to invasive disease and poor prognosis (38-40). EMT was concurrent with the disruption of $E_2$/ERα signaling and the appearance of more aggressive and invasive phenotypes. We also find ERα to be down-regulated such that it is no longer the prime determinant of tumor growth, underscoring this as a potential mechanism by which tumors become resistant to endocrine therapy. Of interest, a recent report has shown association between low ERα and EMT and poor prognosis in human endometrial carcinoma (41). The therapeutic implication is that although women may be diagnosed as $ER^+$, some will not respond favorably to endocrine therapies because growth of their tumor is hormone-independent based on the nature of their tissue microenvironment. Therefore, it may be advantageous to simultaneously inhibit pro-inflammatory molecules in a fibroblast-enriched tumor microenvironment in combination with the use of anti-estrogen or other endocrine therapies.

At this stage, two directions were apparent to us – first, providing a set of molecular targets that could be used for diagnostic assays or drug targets, and, second, the need for a convenient method that can assess the entire tumor despite spatial heterogeneity found in the tumor and its microenvironment. In analyzing fibroblast-epithelial cell interactions for molecular targets using protein microarrays, we found this interaction to result in expression of a set of regulatory proteins, including M-CSF, SDF-1, and MMP family proteins that have been individually associated with cancer-activated fibroblasts and invasive disease (28, 29, 38, 42). Our time-course experiments show that these represent early signaling events in the fibroblast-cancer cell relationship and suggest that it is the combined external signaling of both fibroblasts and cancer cells that contributes to the extracellular milieu that drives an EMT phenotype in the cancer cells. Notably, while the presence of fibroblasts increased tumor cell invasiveness, the proteins secreted into conditioned medium upon interactions with cancer cells also greatly affected the properties of normal mammary epithelial cells. These observations imply that fibroblast-cancer cell interactions may put at risk nearby normal mammary epithelial cells, initiating early cancer-like phenotypic changes that may be relevant to indolence vs. acceleration of early stages of breast tumorigenesis. Our observations are supported by work in mouse mammary gland showing the impact of mammary stromal cells in promoting the initiation of cancer-like properties of normal mammary epithelial cells (43). Further, fibroblasts may be implicated in the etiology of diseases such as benign prostatic hyperplasia that have been associated with EMT (44).

Because the secreted proteins identified in these experiments are potentially clinically actionable, we used the protein expression data to obtain a corresponding panel of genes (iSig). Since the protein expression is assured, this approach helps narrow the gene signature to a functionally-relevant and likely more effective, smaller biomarker set. We determined that this *in vitro* signature could be used to cluster patient samples and predict prognosis. Several signatures of breast cancer invasiveness and poor prognosis have been reported (45, 46). These, however, come from a top-down approach utilizing statistical patterns found in the gene expression profiles of patient tumors. By taking the results of controlled *in vitro* experiments and comparing the data to patient genome-wide expression, this 'bottom up' approach can be used to provide mechanistic insight into tumor progression. Moreover, this approach relies on the ability of the tumor to interact with the microenvironment and, is therefore not an inherent property of the tumor cells alone. Our developed approach is complementary to existing subtyping and can be employed to broaden and enhance the present system.

Finally, we utilized the novel approach of FT-IR spectroscopic imaging for determining hormone sensitivity in biological samples in a facile and expeditious manner. This label-free and non-destructive technique was able to provide chemical signatures of disease progression. We correlated gene expression and a loss of $E_2$/ERα signaling with decreases in peak height in the C-H stretching region of the spectrum in 3D culture cell samples. These results are validated by prior observations that EMT is associated with changes in lipid profiles in epithelial cells (47). We also confirm that MCF-7 cells become resistant to tamoxifen using spectral features, primarily in the peaks associated with nucleic acids. These results directly correlate optical profiles to cellular behaviors and genomics. Translating the cell culture results to patient samples, the *in vitro* chemical signature was also found in invasive breast cancer biopsies with differing levels of ER expression. These results indicate that FT-IR imaging can potentially be useful, alongside IHC and molecular marker analyses, to determine ERα functionality in tissue. Though other imaging techniques such as positron emission tomography (PET) have been used for functional imaging studies before and after therapy (48), development of a similar approach at the microscopic scale is complicated by the need to also appreciate the morphology and spatial heterogeneity of cell types present in the tumor and its microenvironment. FT-IR imaging can provide microscopic evidence rapidly and is applicable at the time of usual post-biopsy diagnoses in pathology.

In conclusion, using novel approaches, we have demonstrated that mammary tissue fibroblasts can alter therapeutic response to anticancer agents and play a crucial role in controlling whether $ER^+$ breast cancer cells respond to hormone or become resistant to endocrine therapies. Thus, the tumor microenvironment can result in deregulation of estrogen receptor signaling and alterations in cell survival signaling molecules that provide tumors with alternative proliferative and survival stimuli (49-52). The pro-inflammatory microenvironment that is generated as a result of epithelial-fibroblast interactions is sufficient to stimulate EMT in breast cancer cells and, also strikingly, in normal mammary epithelium. Notably, the molecules identified from this interaction are also upregulated in breast cancers from patients with invasive disease and predict a less good clinical outcome (26-29, 42, 54-55). Our findings provide new molecular insights into the microenvironment regulation of tumor behavior via interaction between cancer cells, fibroblasts, and nearby normal epithelial cells, and should aid in the development of specific inhibitors of molecular species in this cross-talk that promote early stages in tumorigenesis as well as cancer growth and progression to a more aggressive, therapy-resistant state.

**Materials and Methods**

*Cell Culture*

MCF-7 cells were grown as previously described (27). Primary normal human mammary fibroblasts (HMF) were purchased from ScienCell and cultured according to their specifications (ScienCell Research Laboratories, Carlsbad, California, USA). Fibroblasts were used prior to passage 8 to ensure phenotype stability. Primary normal human mammary epithelial cells (HMEC) were also purchased from ScienCell and cultured according to their specifications. HMEC were used prior to passage 3 to ensure phenotype stability. For sandwich (non-contact) co-culture, MCF-7 cells were cultured in hormone-depleted medium (TM, comprised of phenol red-free basal MEM containing 5% charcoal-dextran stripped calf serum). 3D cultures were prepared by spreading a thin layer of growth factor-reduced phenol red-free Matrigel (BD Biosciences, San Jose, California, USA) in multi-well plates and seeding a low density of MCF-7 on top (for a 12-well plate, 100 µl of Matrigel was used and 8,000 cells were seeded per well). The cells were seeded in 1 ml of TM containing 2.5% dissolved Matrigel. Fibroblasts were embedded in 600 µl of a 2 mg/ml type I collagen gel (Type I collagen from rat tail tendon, BD Biosciences, San Jose, California, USA) at a density of 350,000 cells/ml and prepared in 24-well plates as previously described (14). MCF-7 cells were grown in 3D for 5-7 days in TM before adding fibroblast layer. Fibroblasts were grown for two days in 3D gels before co-culture. Co-culture ranged from 3-6 days before analysis. For

the 'direct' co-culture, 100 µl of Matrigel was spread in each well of a 12-well plate and 8,000 MCF-7 cells were seeded as before. After 5-7 days of growth in TM, HMF were seeded at a ratio of 3:1 or 5:1 (2,700 or 1,600 HMF per well respectively). The medium was then switched to a 3:1 or 5:1 ratio of TM: complete FM medium (ScienCell Research Laboratories) for the duration of the co-culture. MCF-7 cells were grown alone as a control, and their medium was the 1:1 mix for these experiments.

*Proliferation Assays*

All proliferation assays were performed using the WST-1 reagent (Roche Applied Science, Indianapolis, Indiana, USA) as described (56). For each time-point, the medium was replaced with fresh TM:FM containing 10% v/v fresh thawed WST-1 reagent. After 30 min of incubation, absorbance was read at 450 nm on a PerkinElmer Victor X Multilabel Plate Reader (PerkinElmer, Waltham, Massachusetts, USA). Data were normalized to the vehicle control based on cell type (for example, MCF-7 treatments were normalized to MCF-7 vehicle control, while 3:1 treatments were normalized to the 3:1 vehicle control) in Excel and plotted in GraphPad. All samples were prepared in duplicate.

*Invasion assays*

HMF ($1x10^4$) were seeded on the bottom of modified Boyden chambers while MCF-7 ($3x10^4$) were seeded on precoated filters (8 µm pore size) after membrane rehydration (BD Biosciences). Following incubation for 48 h at 37 °C, cells were fixed in 10 % formalin buffer and stained using crystal violet. Non-invaded cells on the surface of the filter were removed using a cotton swab. Invasion was quantified as described (56) by counting the percentage of cells that had invaded the filter compared to the total seeded number.

*Quantitative Real-time PCR*

Total RNA was isolated from cells using TRIzol (Invitrogen, Life Technologies, Carlsbad, California, USA). cDNA was prepared by reverse transcription with M-MuLV Reverse Transcriptase (New England Biolabs Inc, Ipswich, Massachusetts, USA). mRNA expression was measured using quantitative real-time PCR on a high-throughput ABI Prism 7900HT real-time instrument (Applied Biosystems, Life Technologies, Carlsbad, California, USA) using SYBR Green PCR Master Mix (Applied Biosystems) as described previously (57).

*Immunohistochemistry*

For both immunohistochemistry and FT-IR imaging analysis, samples were fixed in freshly-prepared 4% paraformaldehyde for 1 h, mounted in Histogel (Thermo Fisher Scientific Inc., Waltham, Massachusetts, USA), and then paraffin-embedded. For paraffin embedding, samples mounted in Histogel were dehydrated with serial ethanol washes (50%, 70%, 80%, 95%, 100%, 100% for 3 h each) followed by three 2 h clearing steps in xylenes, and finally four 1 h paraffin infiltration steps (ParaPlast Plus, Sigma-Aldrich, St. Louis, Missouri, USA).

For IHC, samples were sectioned at 10 µm onto poly-L-lysine coated slides (Thermo Fisher Scientific, Waltham, Massachusetts, USA). Once dry, slides were deparaffinized (2 x 3 min xylene, 1 x 3 min 1:1 xylene/100% ethanol, 2 x 3 min 100% ethanol, 1 x 3 min 95% ethanol, 1 x 3 min 70% ethanol, 1 x 3 min 50% ethanol, cold tap water). Antigen retrieval was performed by boiling the samples in the microwave for 15 min in 10 mM sodium citrate buffer (pH 6.0). Slides were blocked in Tris-buffered saline (TBS) containing 10% FBS overnight at 4 °C. Primary antibody was added in TBS containing 1% BSA for one hour at room temperature. The remainder of the protocol was performed as specified using a HRP/DAB detection kit (EXPOSE Mouse and Rabbit Specific HRP/DAB Detection IHC kit, Abcam, Cambridge, Massachusetts, USA). E-cadherin antibody was used at a dilution of 1:400 (E-cadherin 24E10 Rabbit mAb, Cell Signaling Technology, Danvers, Massachusetts, USA).

*Antibody Arrays and Classification of the Protein Signature*

Antibody Array was from RayBiotech, Inc. (L-Series 507: RayBio® Label-based Human Antibody Array 1-Membrane). Array analyzes 507 human proteins simultaneously in two samples to examine differential expression. Conditioned medium was obtained from mixed (direct contact) co-cultures after 3 days and this was compared with conditioned medium from MCF-7 cells grown in 3D for the same length of time. Samples were prepared according to the manufacturer's specifications. Protein array membrane was imaged with an Image Quant LAS 4010 Luminescent image analyzer (GE Healthcare, Waukesha, Wisconsin, USA). GO and pathway classifications of the protein signature were conducted using web-based DAVID Bioinformatics Resources database (58) and MetaCore™ (Thomson Reuters, New York, NY, USA).

*FT-IR Imaging and Image Classification*

For cell culture samples, paraffin embedded samples were sectioned at 5 µm onto MirrIR IR-reflective glass slides (Kevley Technologies, Chesterland, Ohio, USA). Once dry, samples were deparaffinized in

hexanes for 24 h and then dried before imaging. For FT-IR imaging, a PerkinElmer Spotlight 400 (PerkinElmer, Waltham, Massachusetts, USA) equipped with a thermal source and a raster-scanning linear array detector was used with a Germanium ATR imaging accessory. An NB medium apodization was applied, a 1 cm $s^{-1}$ mirror speed was used for acquisition, and zeropadding was not used.

Background scans were taken at 8 $cm^{-1}$ spectral resolution. 150 x 150 µm images were collected at 8 $cm^{-1}$ spectral resolution with 16 scans per pixel and a 1.56 x 1.56 µm pixel size. Data were atmospheric and ATR corrected on the Spotlight, and further processing was done using ENVI-IDL. A minimum noise fraction (MNF) algorithm was applied on all images (59) to reduce noise in the data. Two regions were imaged per sample, and samples were prepared in duplicate (for a total of 4 data sets per condition). Because each image represented a combination of cells, Matrigel, and Histogel, a Bayesian-type classifier was developed as before (13) that labeled spectral contributions from cells within the image. Only cell spectra were plotted and compared, to reduce the influence of chemical contributions from the extracellular matrix and embedding material. Once spectra were classified and extracted, a baseline correction was applied and spectra were further normalized to the Amide I peak (1656 $cm^{-1}$) for comparison. Spectra were plotted using OriginPro software.

*Data Analysis of Microarrays*

A publicly-available microarray dataset was downloaded from GEO (GSE26304) and included 31 pure DCIS patients, 36 IDC patients, and 42 patients with 'Mixed' histology (30). Data were transformed into GeneSpring GX 7.3 and chips and genes were median normalized and median polished. Hierarchical clustering of the genes matching the 46-protein secreted signature was performed and displayed using Eisen Cluster and TreeView software for analysis and visualization. The 46-protein signature was uploaded in ONCOMINE™ (Compendia Bioscience, Ann Arbor, Michigan, USA), using the following filters: odds ratio >2, and P-value <0.001, epithelial versus stroma or invasive cancer versus ductal-carcinoma *in situ* and cancer type (breast cancer). The Oncomine database was also used for visualization of significantly associated datasets.

**References**


1. Clark G.M., Osborne C.K., and McGuire W.L. (1984) Correlations between estrogen receptor, progesterone receptor, and patient characteristics in human breast cancer. *J Clin Oncol* **2**(10): 1102-1109.
2. Harvey J.M., Clark G.M., Osborne C.K., and Allred D.C. (1999) Estrogen receptor status by immunohistochemistry is superior to the ligand-binding assay for predicting response to adjuvant endocrine therapy in breast cancer. *J Clin Oncol* **17**(5): 1474-1481.
3. Collaborative EBCT. (1998) Tamoxifen for early breast cancer: an overview of the randomised trials. *Lancet* **351**(9114): 1451-1467.
4. Collaborative EBCT. (2005) Effects of chemotherapy and hormonal therapy for early breast cancer on recurrence and 15-year survival: an overview of the randomised trials. *Lancet* **365**(9472): 1687-1717.
5. Gonzalez-Angulo A.M., Morales-Vasquez F., and Hortobagyi G.N. (2007) Overview of resistance to systemic therapy in patients with breast cancer. *Adv Exp Med Biol* **608**: 1-22.
6. Osborne C.K. and Schiff R. (2011) Mechanisms of endocrine resistance in breast cancer. *Annual review of medicine* **62**: 233-247.
7. Musgrove E.A. and Sutherland R.L. (2009) Biological determinants of endocrine resistance in breast cancer. *Nature Reviews Cancer* **9**(9): 631-643.
8. Fischbach C*., et al.* (2007) Engineering tumors with 3D scaffolds. *Nat Methods* **4**(10): 855-860.
9. Debnath J., Muthuswamy S.K., and Brugge J.S. (2003) Morphogenesis and oncogenesis of MCF-10A mammary epithelial acini grown in three-dimensional basement membrane cultures. *Methods* **30**(3): 256-268.
10. Nelson C.M., Inman J.L., and Bissell M.J. (2008) Three-dimensional lithographically defined organotypic tissue arrays for quantitative analysis of morphogenesis and neoplastic progression. *Nat Protoc* **3**(4): 674-678.
11. Bauer M., Su G., Beebe D.J., and Friedl A. (2010) 3D microchannel co-culture: method and biological validation. *Integr Biol (Camb)* **2**(7-8): 371-378.
12. Kimlin L.C., Casagrande G., and Virador V.M. (2013) In vitro three-dimensional (3D) models in cancer research: an update. *Mol Carcinog* **52**(3): 167-182.
13. Bhargava R. (2012) Infrared spectroscopic imaging: the next generation. *Appl Spectrosc* **66**(10): 1091-1120.

14. Holton S.E., Walsh M.J., Kajdaçsy-Balla A., and Bhargava R. (2011) Label-free characterization of cancer-activated fibroblasts using infrared spectroscopic imaging. *Biophys J* **101**(6): 1513-1521.
15. Mourant J.R., Yamada Y.R., Carpenter S., Dominique L.R., and Freyer J.P. (2003) FTIR spectroscopy demonstrates biochemical differences in mammalian cell cultures at different growth stages. *Biophys J* **85**(3): 1938-1947.
16. Fernandez D.C., Bhargava R., Hewitt S.M., and Levin I.W. (2005) Infrared spectroscopic imaging for histopathologic recognition. *Nat Biotechnol* **23**(4): 469-474.
17. Gazi E.*, et al.*(2009) A FTIR microspectroscopic study of the uptake and metabolism of isotopically labelled fatty acids by metastatic prostate cancer. *Vib Spectrosc* **50**(1): 99-105.
18. Walsh M.J.*, et al.* (2008) Fourier transform infrared microspectroscopy identifies symmetric $PO_2^-$ modifications as a marker of the putative stem cell region of human intestinal crypts. *Stem Cells* **26**(1): 108-118.
19. Bhargava R. (2007) Towards a practical Fourier transform infrared chemical imaging protocol for cancer histopathology. *Anal Bioanal Chem* **389**(4): 1155-1169.
20. Bhargava R., Fernandez D.C., Hewitt S.M., and Levin I.W. (2006) High throughput assessment of cells and tissues: Bayesian classification of spectral metrics from infrared vibrational spectroscopic imaging data. *Biochim Biophys Acta* **1758**(7): 830-845.
21. Reddy R.K., Walsh M.J., Schulmerich M.V., Carney P.S., and Bhargava R. (2013) High-definition infrared spectroscopic imaging. *Appl Spectrosc* **67**(1): 93-105.
22. Steiner G.*, et al.* (2002) Detection and grading of human gliomas by FTIR spectroscopy and a genetic classification algorithm. *Proc. SPIE 4614, Biomedical Vibrational Spectroscopy II* **4614**: 127-133.
23. Cardamone M.D., *et al.* (2009) ERα as ligand-independent activator of CDH-1 regulates determination and maintenance of epithelial morphology in breast cancer cells. *Proc Natl Acad Sci USA* **106**(18): 7420-7425.
24. Ward A.*, et al.* (2013) Re-expression of microRNA-375 reverses both tamoxifen resistance and accompanying EMT-like properties in breast cancer. *Oncogene* **32**(9): 1173-1182.
25. Yang J. and Weinberg R.A. (2008) Epithelial-mesenchymal transition: at the crossroads of development and tumor metastasis. *Dev Cell* **14**(6): 818-829.
26. Ma L.*, et al.* (2001) Expression of amphiregulin and epidermal growth factor receptor in human breast cancer: analysis of autocriny and stromal-epithelial interactions. *J Pathol* **194**(4): 413-419.

27. Stossi F., Madak-Erdogan Z., and Katzenellenbogen B.S. (2012) Macrophage-elicited loss of estrogen receptor-alpha in breast cancer cells via involvement of MAPK and c-Jun at the ESR1 genomic locus. *Oncogene* **31**(14): 1825-1834.

28. Balduyck M.*, et al.* (2000) Specific expression of matrix metalloproteinases 1, 3, 9 and 13 associated with invasiveness of breast cancer cells in vitro. *Clin Exp Metastasis* **18**(2): 171-178.

29. Vizoso F.J.*, et al.* (2007) Study of matrix metalloproteinases and their inhibitors in breast cancer. *Br J Cancer* **96**(6): 903-911.

30. Muggerud A.A.*, et al.* (2010) Molecular diversity in ductal carcinoma in situ (DCIS) and early invasive breast cancer. *Mol Oncol* **4**(4): 357-368.

31. Boersma B.J.*, et al.* (2008) A stromal gene signature associated with inflammatory breast cancer. *Int J Cancer* **122**(6): 1324-1332.

32. Ma X.J., Dahiya S., Richardson E., Erlander M., and Sgroi D.C. (2009) Gene expression profiling of the tumor microenvironment during breast cancer progression. *Breast Cancer Res* **11**(1): R7.

33. Rhodes D.R.*, et al.* (2004) ONCOMINE: a cancer microarray database and integrated data-mining platform. *Neoplasia* **6**(1): 1-6.

34. Schuetz C.S.*, et al.* (2006) Progression-specific genes identified by expression profiling of matched ductal carcinomas in situ and invasive breast tumors, combining laser capture microdissection and oligonucleotide microarray analysis. *Cancer Res* **66**(10): 5278-5286.

35. Bhargava R. and Dabbs D.J. (2007) Use of immunohistochemistry in diagnosis of breast epithelial lesions. *Adv Anat Pathol* **14**(2): 93-107.

36. Casal H.L. and Mantsch H.H. (1984) Polymorphic phase behaviour of phospholipid membranes studied by infrared spectroscopy. *Biochim Biophys Acta* **779**(4): 381-401.

37. Petibois C. and Deleris G. (2005) Evidence that erythrocytes are highly susceptible to exercise oxidative stress: FT-IR spectrometric studies at the molecular level. *Cell Biol Int* **29**(8): 709-716.

38. Jahkola T., Toivonen T., Nordling S., von Smitten K., and Virtanen I. (1998) Expression of tenascin-C in intraductal carcinoma of human breast: relationship to invasion. *Eur J Cancer* **34**(11): 1687-1692.

39. Tse J.C. and Kalluri R. (2007) Mechanisms of metastasis: epithelial-to-mesenchymal transition and contribution of tumor microenvironment. *J Cell Biochem* **101**(4): 816-829.

40. Taube J.H., *et al.* (2010) Core epithelial-to-mesenchymal transition interactome gene-expression signature is associated with claudin-low and metaplastic breast cancer subtypes. *Proc Natl Acad Sci USA* **107**(35): 15449-15454.

41. Wik E*., et al.* (2013) Lack of estrogen receptor-alpha is associated with epithelial-mesenchymal transition and PI3K alterations in endometrial carcinoma. *Clin Cancer Res* **19**(5): 1094-1105.
42. Kojima Y*., et al.* (2010) Autocrine TGF-beta and stromal cell-derived factor-1 (SDF-1) signaling drives the evolution of tumor-promoting mammary stromal myofibroblasts. *Proc Natl Acad Sci USA* **107**(46): 20009-20014.
43. Casbas-Hernandez P., Fleming J.M., and Troester M.A. (2011) Gene expression analysis of in vitro cocultures to study interactions between breast epithelium and stroma. *Journal of biomedicine & biotechnology* **2011**: 520987.
44. Alonso-Magdalena P., *et al*. (2008) A role for epithelial-mesenchymal transition in the etiology of benign prostatic hyperplasia. *Proc Natl Acad Sci USA* **106**(8): 2859-2863.
45. Filipits M*., et al.* (2011) A new molecular predictor of distant recurrence in ER-positive, HER2-negative breast cancer adds independent information to conventional clinical risk factors. *Clin Cancer Res* **17**(18): 6012-6020.
46. Ma X.J*., et al.* (2004) A two-gene expression ratio predicts clinical outcome in breast cancer patients treated with tamoxifen. *Cancer Cell* **5**(6): 607-616.
47. Sampaio J.L., *et al.* (2010) Membrane lipidome of an epithelial cell line. *Proc Natl Acad Sci USA* **108**(5): 1903-1907.
48. Dehdashti F*., et al.* (2009) PET-based estradiol challenge as a predictive biomarker of response to endocrine therapy in women with estrogen-receptor-positive breast cancer. *Breast Cancer Res Treat* **113**(3): 509-517.
49. Hutcheson I.R*., et al.* (2003) Oestrogen receptor-mediated modulation of the EGFR/MAPK pathway in tamoxifen-resistant MCF-7 cells. *Breast Cancer Res Treat* **81**(1): 81-93.
50. Iorio M.V*., et al.* (2005) MicroRNA gene expression deregulation in human breast cancer. *Cancer Res* **65**(16): 7065-7070.
51. McCubrey J.A*., et al.* (2006) Roles of the RAF/MEK/ERK and PI3K/PTEN/AKT pathways in malignant transformation and drug resistance. *Adv Enzyme Regul* **46**: 249-279.
52. Ring A. and Dowsett M. (2004) Mechanisms of tamoxifen resistance. *Endocr Relat Cancer* **11**(4): 643-658.
53. Zhou Y*., et al.* (2007) Enhanced NF kappa B and AP-1 transcriptional activity associated with antiestrogen resistant breast cancer. *BMC Cancer* **7**: 59.

54. Tang R.*, et al.* (1992) M-CSF (monocyte colony stimulating factor) and M-CSF receptor expression by breast tumour cells: M-CSF mediated recruitment of tumour infiltrating monocytes? *J Cell Biochem* **50**(4): 350-356.

55. Pontiggia O.*, et al.* (2012) The tumor microenvironment modulates tamoxifen resistance in breast cancer: a role for soluble stromal factors and fibronectin through beta1 integrin. *Breast Cancer Res Treat* **133**(2): 459-471.

56. Bergamaschi A., Christensen B.L., and Katzenellenbogen B.S. (2011) Reversal of endocrine resistance in breast cancer: interrelationships among 14-3-3zeta, FOXM1, and a gene signature associated with mitosis. *Breast Cancer Res* **13**(3)**:** R70.

57. Frasor J.*, et al.* (2006) Gene expression preferentially regulated by tamoxifen in breast cancer cells and correlations with clinical outcome. *Cancer Res* **66**(14): 7334-7340.

58. Dennis G., *et al*. (2003) DAVID: Database for Annotation, Visualization, and Integrated Discovery. *Genome Biology* **4**(5): P3.

59. Reddy R.K. and Bhargava R. (2010) Accurate histopathology from low signal-to-noise ratio spectroscopic imaging data. *Analyst* **135**(11): 2818-2825.

# CHAPTER FOUR: DESCRIBING LABEL-FREE CHEMICAL SIGNATURES OF 3D BREAST CELL CULTURES USING FT-IR IMAGING


## Abstract

The determination of label-free optical signatures of disease progression may improve diagnostic and prognostic assessment of human tumors. We used Fourier transform infrared spectroscopic imaging and computational methods to correlate cancerous phenotypes to label-free optical signatures in three-dimensional culture models of breast cancer. Using a set of cell lines that mimic disease progression from confined to metastatic breast cancer, we identify spectroscopic signatures that correspond to each stage. We also discriminate between cells that are tamoxifen sensitive and tamoxifen resistant, and show how fibroblasts alter this signature. Finally, we determine the degree of heterogeneity between cells found in the same tumor spheroid and how this determines response to hormones and the presence of fibroblasts in 3D culture. Our findings highlight the use of FT-IR imaging and multivariate analysis for the understanding of advanced and heterotypic *in vitro* models of disease.

**Introduction**

Recently, the National Cancer Institute asked the question: How can the physical properties of tumors, such as a cell's electrical, optical or mechanical properties, be used to provide earlier or more reliable cancer detection, diagnosis, prognosis, or monitoring of drug response or tumor recurrence? This question was raised in response to the three decades of work that has shown that it is not only the genetic nature of a cancer cell that determines its outcome but rather the intricate balance between genetics and environment (1-5). With the goal of developing novel diagnostic tools or prognostic markers, recent efforts have highlighted the correlation of optical signatures to cancer progression (6-8). An emerging technique in this field is the use of vibrational spectroscopy coupled with microscopy, or microspectroscopy (9-11). Using Fourier transform infrared (FT-IR) or Raman imaging is advantageous over other imaging methods because label-free optical signatures that contain chemical information at each pixel can be determined. Here, we explore the use of FT-IR to identify signatures of cancerous phenotypes in advanced cell culture models.

Both tumors and normal tissues are known to be heterogeneous in gene expression and phenotype (12). However, most molecular methods including the '-omics are bulk measurements—a population average of hundreds to millions of cells. Imaging can be used to determine the degree of heterogeneity of *in vitro* models of disease or in human tissues. The most common approach is to look at the distribution of one or more markers of disease phenotype, either expression of a protein, DNA, or RNA. These approaches are limited because markers must be profiled individually. Multiplexing is available with immunofluorescence but the number of markers is constrained to the microscope setup, the availability of different flavors of fluorophores, and cross-reactivity of antibody-based labels. Thus, using label-free imaging based on the inherent chemical differences is advantageous for working with heterogeneous samples. FT-IR spectroscopic imaging was used here to put bulk molecular measurements in the context of cellular heterogeneity.

There are some challenges associated with the analysis of FT-IR images. This approach generates a three-dimensional dataset in which an image is formed where each pixel contains a spectrum of chemical information (Chapter 1). Further, FT-IR is extremely sensitive to chemical changes. Parsing out spectroscopic signatures of cancerous phenotypes is alleviated by good experimental design, consistent sample preparation, and data processing techniques that can reduce the dimensionality of the dataset

and classify or cluster samples based on spectral similarities. Here, we combine these approaches to correlate cellular phenotypes to label-free chemical signatures.

Consistent sample preparation is essential for describing chemical signatures of disease because IR detects changes in molecular bonds. Cell cultures are typically fixed physically or chemically to retain structural and molecular information. However, fixation by drying or freezing can destroy cellular architecture while chemical fixation can alter molecular components. Previous studies have pelleted cells to avoid this problem, but in this instance spatial information is lost (13). Recently, it has been shown that formalin fixation and paraffin embedding does maintain the lipid, phosphate, and protein profiles of cells (14). Because this is the standard sample preparation used in hospital pathology laboratories, this procedure was used for experiments described herein.

Spectral features identified in cells with increasingly cancerous phenotypes can be correlated to changes in proteins, lipids, and nucleic acids. The most prominent features related to proteins are the bands at amide II (1545 $cm^{-1}$) and amide I (1650 $cm^{-1}$), corresponding to amide groups (CO-NH) (15). Alterations in these peaks have also been associated with changes in protein conformation or secondary structure (16). Proteins may also contribute to the absorbance in bands in the 2850 - 2960 $cm^{-1}$ region due to the presence of methylene ($CH_2$) and methyl ($CH_3$) groups found in both proteins and lipids (17). The $PO_2^-$ phosphodiester group of nucleic acids has vibrational modes at 1220 $cm^{-1}$ (symmetric) and 1080 $cm^{-1}$ (asymmetric). Although this functional group is also present in phospholipids, the carbonyl group of phospholipids should also be observed at 1740 $cm^{-1}$ if these are abundant in the sample of interest (18). Peaks corresponding to lipids cannot be unambiguously designated as there are spectral contributions from proteins in the same region (2850 – 2960 $cm^{-1}$). Therefore, the spatial distribution of peaks in this region should be assessed using imaging (19). Information about chemical changes in heterogeneous can be accomplished by performing controlled experiments thereby directly correlating cellular phenotype and molecular profiling with spectral profiles.

Further, it is important to identify spectroscopic changes associated with cancerous phenotypes in an unbiased manner. Data processing strategies that have been used for other large datasets such as genome-wide studies can be used. Reducing the dimensionality of FT-IR data and finding associations between and within heterogeneous samples can lead to the determination of label-free spectroscopic signatures associated with biological changes and corresponding to disease states. Bayesian classifiers

have been used by our group and others for the unbiased recognition of different cellular or extracellular component classes in heterogeneous samples (11, 20, 21). Here, we develop a classifier to use with 3D cell culture samples. Principal component analysis (PCA) and unsupervised hierarchical clustering have also been efficacious in the determination of spectroscopic signatures of biological processes (22, 23).

In this study, we define label-free spectroscopic signatures of cancerous phenotypes in heterogeneous 3D culture models of breast cancer progression. We used several approaches including Bayesian classification, second derivative analysis, unsupervised hierarchical clustering, and image analysis to differentiate between different cancerous phenotypes. Here, we highlight the use of FT-IR imaging for studying cancer disease progression in cell culture models.

**Results**

*Development of a Bayesian classifier to extract cell spectra from ECM components*

Three-dimensional cultures are heterogeneous, including one or more cell types and a hydrogel platform that consists of a mixture of carbohydrates and proteins. The 3D cultures used in this study contain either epithelial cells or epithelial cells and fibroblasts and are grown in Matrigel. Matrigel is derived from the Engelbreth-Holm-Swarm (EHS) tumor of the mouse and has been shown to contain type IV collagen, laminin, heparin sulfate proteoglycan, entactin, nidogen, and fibronectin (24-28). The relative concentrations of laminin, type IV collagen, and heparin sulfate proteoglycan were determined to be 1: 0.6: 0.03 (29). Further, the 3D culture is processed by embedding first in a compound called Histogel before it is paraffin-embedded (30). Histogel is an inert compound similar to agarose and does not retain histological stains. Due to the sensitivity of FT-IR to chemical changes, both the presence of Histogel and Matrigel can make the analysis of heterogeneous samples complicated. Because we are interested in spectral contributions from the cells only, a Bayesian classifier was developed to computationally identify pixels that are cells compared to Matrigel or Histogel. This 3-class classifier was trained by labeling several thousand pixels from each class. Labeling was done manually by comparing visible images to IR images. A total of 45 metrics were used and these metrics were primarily based on ratios of peak height, peak area to height, peak area to area, and peak center of gravity. The 45 metrics optimized by the classifier were from an original set of 144 metrics, developed for work with breast tissue (31). The utility of the classifier is shown in Figure 4.1. An IR image of an acinus was taken. While the shape of the acinus can clearly be seen with the 1656 $cm^{-1}$ peak (center panel), the classifier easily

identifies the cell pixels. This allows the user to quickly identify cell pixels and extract their signature in an unbiased way-- regions of interest (ROIs) do not need to be drawn by hand. While the classifier was excellent at identifying cell pixels, it performed poorly in differentiating between Matrigel and Histogel (Figure 4.2). However, upon inspection of the classified images as well as spectroscopic signatures of the individual classes (Figure 4.3), it is clear that the Matrigel and Histogel pixels are being mislabeled as each other. The pixels of interest are those from cells, and the classifier performs well in this case.

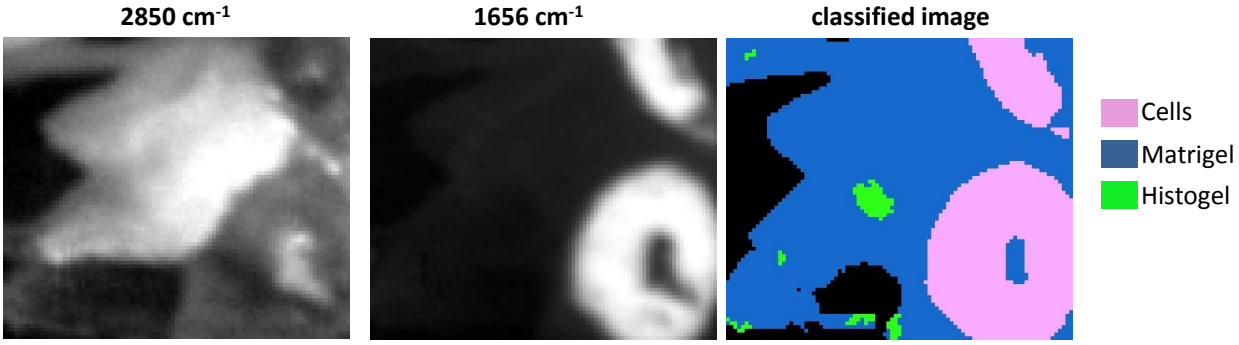


**Figure 4.1: Use of the Bayesian classifier to identify pixels from cells.**

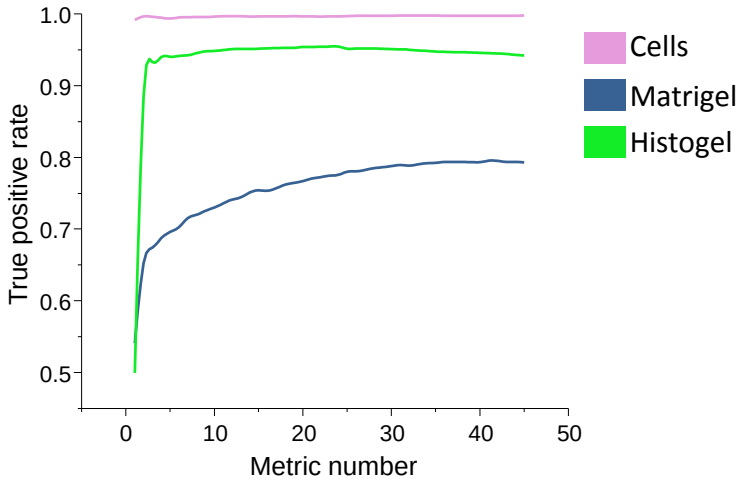


**Figure 4.2: Receiver operating characteristic (ROC) curve identifying the performance of the 3D cell classifier.** Cells were the most accurately classified with 97% accuracy with the first metric.

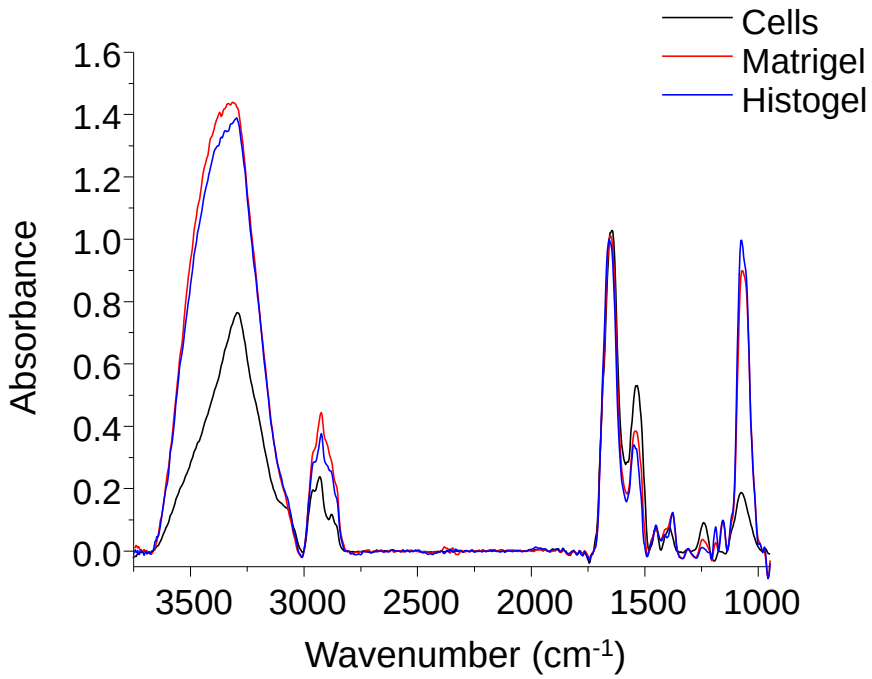


**Figure 4.3: Comparison of cell, Matrigel, and Histogel spectra**

*Increasingly transformed breast epithelial cells show progressive activation in spectral signatures and can be used as a standard to test cellular phenotype after experimental treatment*

The MCF10A cell line is widely used as a model of normal breast epithelium due to its ability to form growth-arrested and polarized acini in 3D reconstituted basement membrane/Matrigel culture (32). These cells form structures with a cytoarchitecture very similar to that found in normal breast epithelium and therefore are used as a comparison to determine the effects of oncogenes or environmental factors on the progression of breast cancer (33, 34). We have used MCF10A cells grown in 3D culture to understand the interaction between breast cancer cells, fibroblasts, and normal epithelium during breast cancer progression from confined to invasive disease. We previously identified a label-free spectroscopic signature of fibroblast-activated MCF10A using FT-IR imaging (Chapter 2). We followed up on this study by determining signatures of controlled disease progression using a system based on MCF10A cells. The M1-M4 cell lines are derived from the MCF10A cell line but become increasingly tumorigenic and eventually metastatic. M1 are MCF10A wild-type cells, while M2 have been stably transfected with T24 *Ha-Ras*. M3 are derived from xenograft-passaged M2 cells, and these cells are able to generate tumors in approximately 25% of xenografts. Finally, M4 are fully tumorigenic and metastatic (35). The benefit of using these cells is that they all have the same genetic background—only

the environmental context has changed. We aimed to use these as a spectroscopic library of phenotypes of cancer progression.

First, the cells were grown on IR-reflective slides and imaged in the Attenuated Total Reflectance (ATR) mode. This was done to determine any basal spectroscopic differences between the cells when grown in monolayer culture. Upon comparison of several hundred cells for each cell line, spectroscopic differences can be seen (Figure 4.4). In particular, the C-H stretching region is notable (Figure 4.5). There is a gradual increase in the absorbance of the peaks in this region as the cells become more tumorigenic. The peaks in this region correspond to the stretching modes of $CH_2$- and $CH_3$ bonds and are associated with changes in fatty acid metabolism (36). We have previously shown these peaks to be relevant in the response of $ER^+$ breast cancer cells to hormone (37). Differences in M1-M4 cell spectra were also seen in the fingerprint region (Figure 4.6), although these changes are more subtle. Importantly, the cell lines have distinct spectroscopic signatures.

Distribution of one peak in the C-H stretching region was analyzed and compared across the cell lines (Figure 4.7). We found that the absorbance at 2930 $cm^{-1}$ is increasingly distributed in the cytoplasm at the edges of the invasive cell line M3 and the metastatic line M4, compared with the less invasive M2 and non-tumorigenic M1. These images correspond to metabolic activity at the leading edges of invasive cells, and suggests that distribution of this peak may be used to assess invasive potential in more physiologically-representative systems.

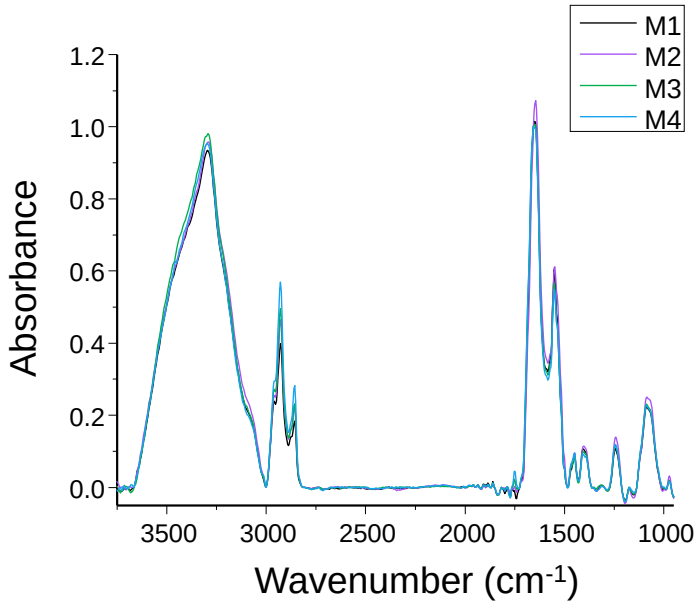


**Figure 4.4: Spectroscopic differences between M1, M2, M3, and M4 cells grown in monolayer culture.**

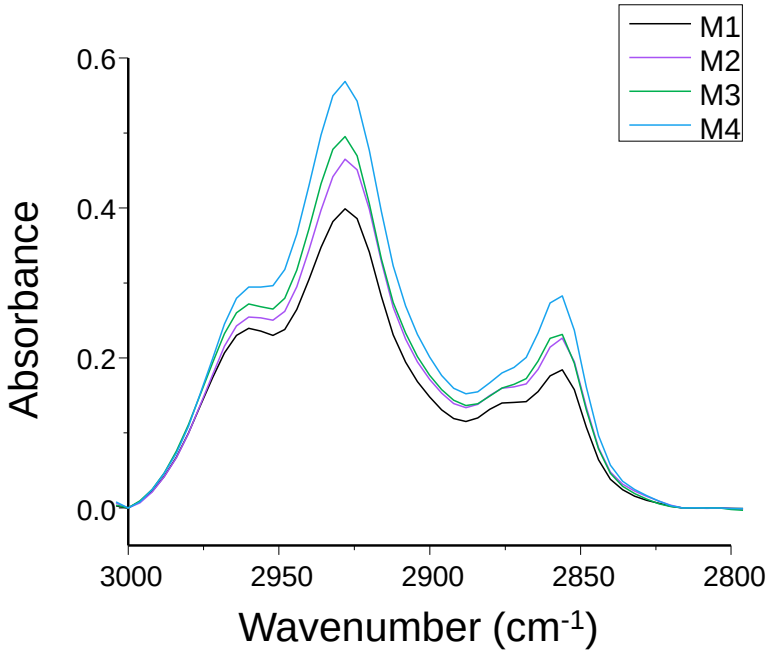


**Figure 4.5: Investigation of the C-H stretching region reveals a distinct pattern in transformation state.** Increases in absorbance at the three peaks in this region is correlated to cells that are more invasive and metastatic.

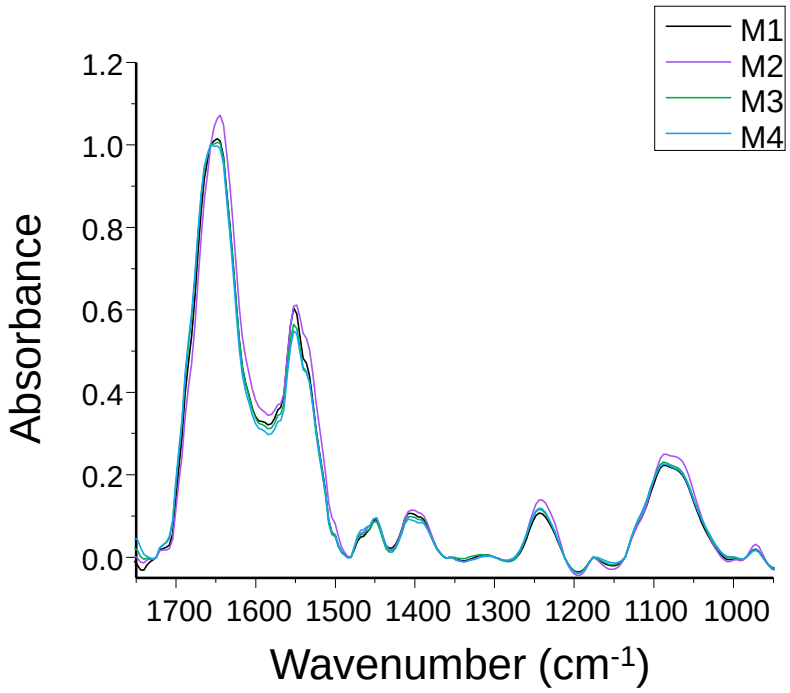


**Figure 4.6: In the fingerprint region, spectral differences are more subtle.**

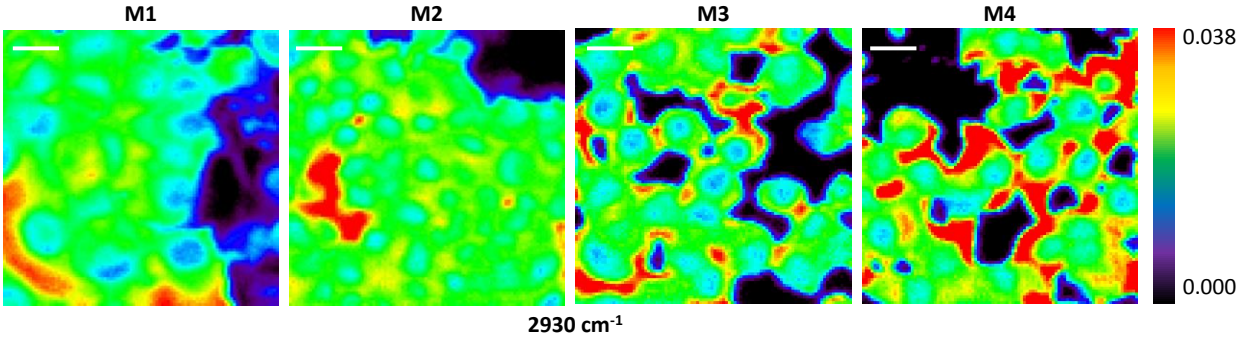


**Figure 4.7: Distribution of the 2930 cm$^{-1}$ band, associated with fatty acids and metabolism, in M1, M2, M3, and M4 monolayer samples**. Scale bar represents 25 µm.

The MCF10A cells are widely used for their ability to form growth-arrested spheroids when grown in 3D culture. M1-M4 cells were grown in 3D culture, and the morphology of the cell types varies drastically and corresponds to disease state (Figure 4.8). M1 cells form polarized acinar structures. M2 also form spheroid structures with defined edges but are considerably larger than M1 acini. M2 also appear to have a larger hypoxic core. M3 cells are the most proliferative and invasive when grown on Matrigel. While they have the most metastatic phenotype in a xenograft model, M4 are the least robust when grown in 3D culture. Rather, they form multicellular structures that quickly become dissociated. It

has been previously shown that 3D breast cultures are more representative of human disease than monolayer cultures (38) and it is for this reason why we continued the FT-IR study using the M1-M4 in a 3D model.

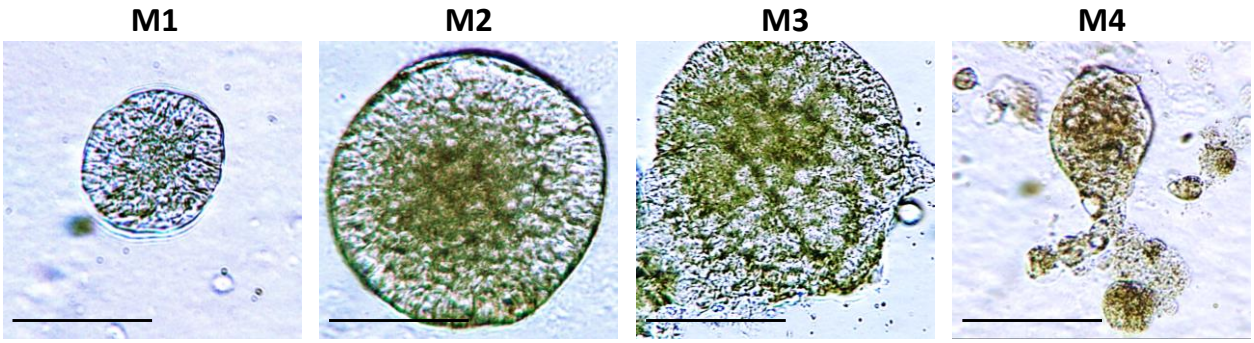


**Figure 4.8: Phase contrast microscope images show differences in size and morphology of M1, M2, M3, and M4 cell spheroids after 7 days of growth.** Scale bar represents 50 µm.

First, we compared the spectroscopic signatures of M1-M4 cells grown in 2D versus those grown in 3D. The second derivative of the normalized average spectra are depicted in Figure 4.9. The second derivative was used to identify differences between samples and can be used to display more subtle differences compared to looking at the raw spectra alone. All multivariate analyses were done using second derivative spectra. It is clear from the spectra that the M3 and M4 cells are very similar in 2D and 3D and are distinct from M1 and M2 cells. To compare the second derivative spectra in an unbiased manner, unsupervised hierarchical clustering (Figure 4.10) was performed on the complete spectral range (4000 – 750 $cm^{-1}$). In agreement with visual inspection of the spectra, the 2D and 3D comparisons for M3 and M4 cell lines clustered together. Different culture conditions of M1 and M2, however, did not cluster together. These results indicate that the chemical nature of M3 and M4 cells may be less sensitive to culture conditions, relating to their invasive properties. The mechanical properties of tissue culture plastic may provide an additional stimulus to drive tumor progression, corresponding to the increased stiffness seen *in vivo* surrounding tumors (39, 40).

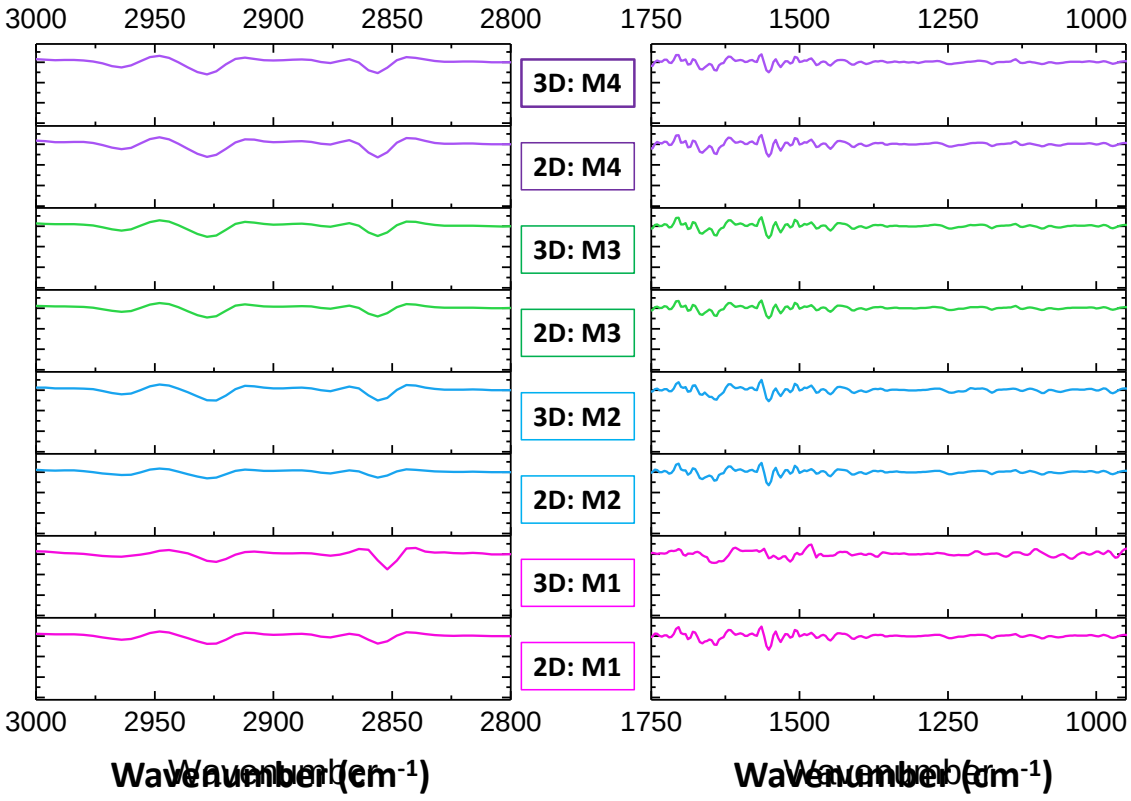


**Figure 4.9: Analysis of second derivative spectra for M1-M4 cells grown in monolayer and 3D culture.**

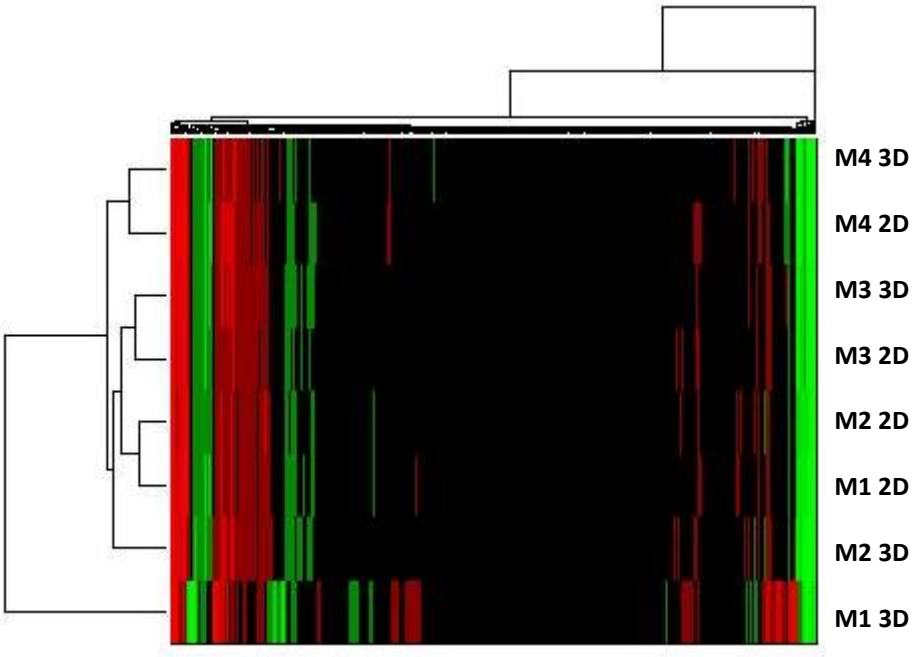


**Figure 4.10: Unsupervised hierarchical clustering of average second derivative spectra shows that spectroscopic differences are maintained when the cells are grown in 3D culture.**

Previously, we had determined that M1 cells (MCF10A) show an activated phenotype upon co-culture with cancer-activated fibroblasts (Chapter 2). This activation profile could be distinguished using FT-IR imaging and showed differences in the C-H stretching region as well as at the 1080 $cm^{-1}$ peak, associated with phosphate stretching of nucleic acids. We have previously shown that the method used to activate fibroblasts, either through treatment with the growth factor TGF-β1 or through co-culture with MCF-7 breast cancer cells, alters the spectroscopic signature of activated fibroblasts (41). We aimed to compare the spectroscopic signatures of fibroblast-activated M1 based on the method by which the fibroblasts were activated. This study will improve the understanding of the interaction between activated fibroblasts and breast epithelium.

Human mammary fibroblasts grown in 3D collagen gels (41) were activated by treating with 1.5 ng/ml TGF-β1 or co-culturing with MCF-7 for one week. Activated fibroblasts were subsequently co-cultured with M1 cells for 24 or 48h before fixation and paraffin embedding. ATR FT-IR images were taken and cell spectra were extracted from the images using the Bayesian classifier described previously. We find clear distinctions between the M1 co-cultured with the differently-activated fibroblasts (Figure 4.11). In the C-H stretching region, the different fibroblast treatments were most similar to one another (Figure 4.12). However, it appears that a longer co-culture time decreases absorbance in the peaks in this region. When the fingerprint region is analyzed, however, absorbance at the peak associated with nucleic acids is increased the most after co-culture for 48 hours with TGF-β activated fibroblasts (Figure 4.13). Our results indicate that the treatment conditions of the fibroblasts impact the spectroscopic signatures of M1 after co-culture.

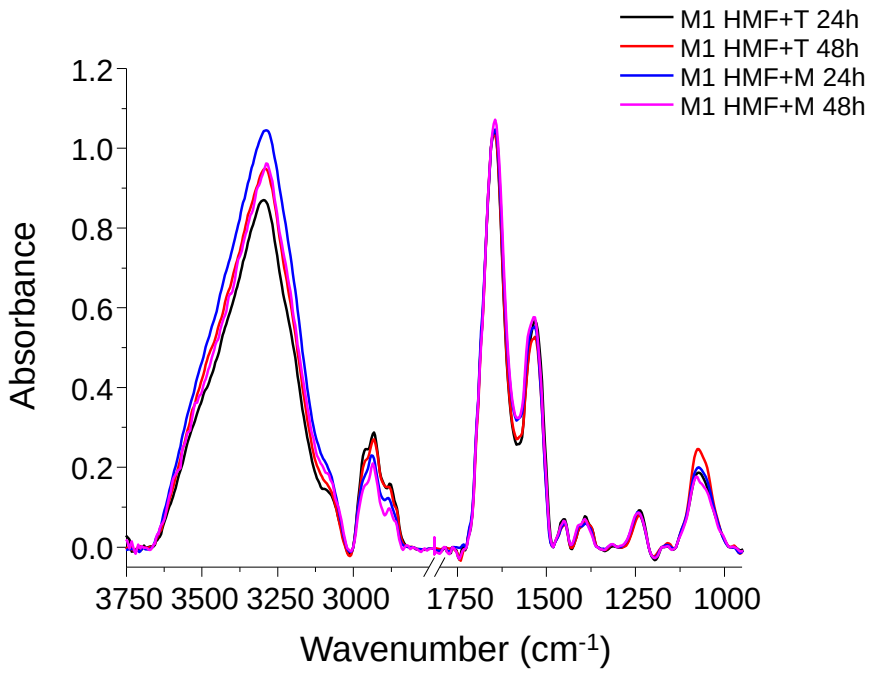


**Figure 4.11: Comparison of spectral signatures for M1 acini co-cultured with HMF activated with TGF-β (+T) and those co-cultured with HMF activated by MCF-7 co-culture (+M).**

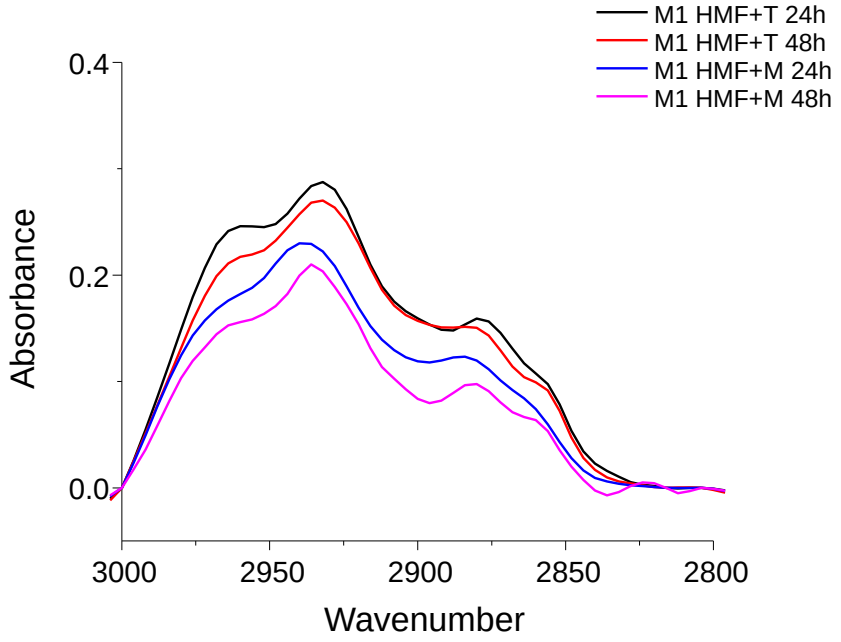


**Figure 4.12: There are clear differences both in the two activation strategies that can be seen in the M1 response to HMF+.** Increasing the length of co-culture time in both conditions decreases overall absorbance at these peaks.

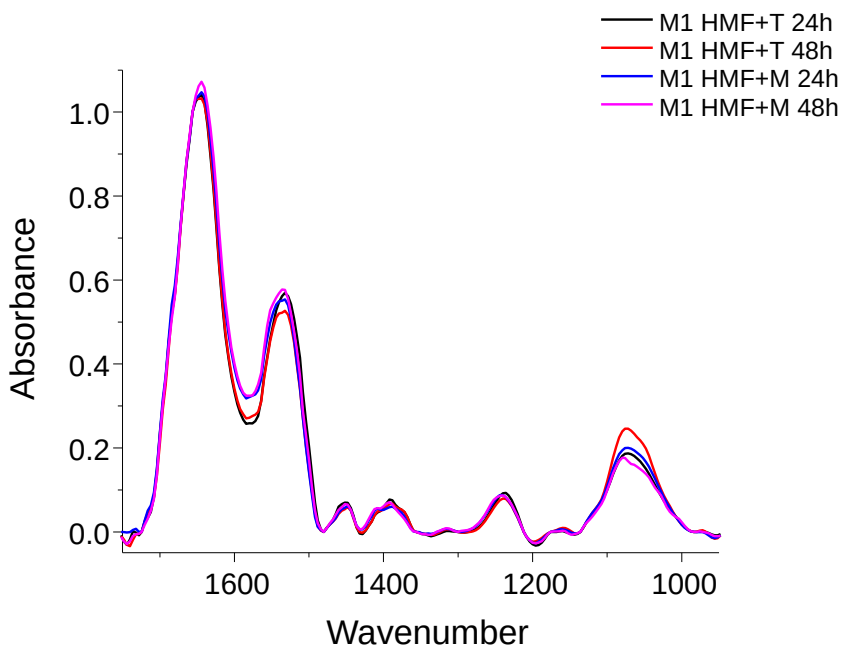


**Figure 4.13: M1 acini co-cultured with TGF-B activated HMF have increased absorbance in the 1080 $cm^{-1}$ peak associated with nucleic acids.**

*Tamoxifen resistant cells and induced tamoxifen resistance in $ER^+$ cells can be correlated to spectroscopic signatures*

We previously demonstrated that FT-IR can be used to determine response to hormones in 3D breast cancer cells (37). One of the targeted therapies given to patients with estrogen receptor-positive ($ER^+$) breast cancer is tamoxifen, but up to 30% of patients experience therapeutic resistance within five years (42, 43). Having found a signature of hormone response, we aimed to determine a label-free spectroscopic signature of tamoxifen resistance. A tamoxifen resistant cell line ($Tam^R$) was derived from MCF-7 cells through the long-term treatment with trans-hydroxytamoxifen (previously described in Reference 44). These cells were grown in 3D culture and imaged in the ATR mode of FT-IR. Their spectral signatures are compared to those of MCF-7 cells in Figure 4.14. $Tam^R$ cells have a distinct spectroscopic signature, but when the signature is compared across samples, there is significant heterogeneity seen in the $Tam^R$ cells compared to MCF-7, particularly in the C-H stretching region (Figure 4.15). The fingerprint region of the spectrum is unremarkable. Cancer cells have heterogeneous phenotypes, and it is likely that not all $Tam^R$ cells are identical. The spectra displayed are an average of hundreds of cells. When the spectra are compared across independent biological replicates, heterogeneous populations may appear different.

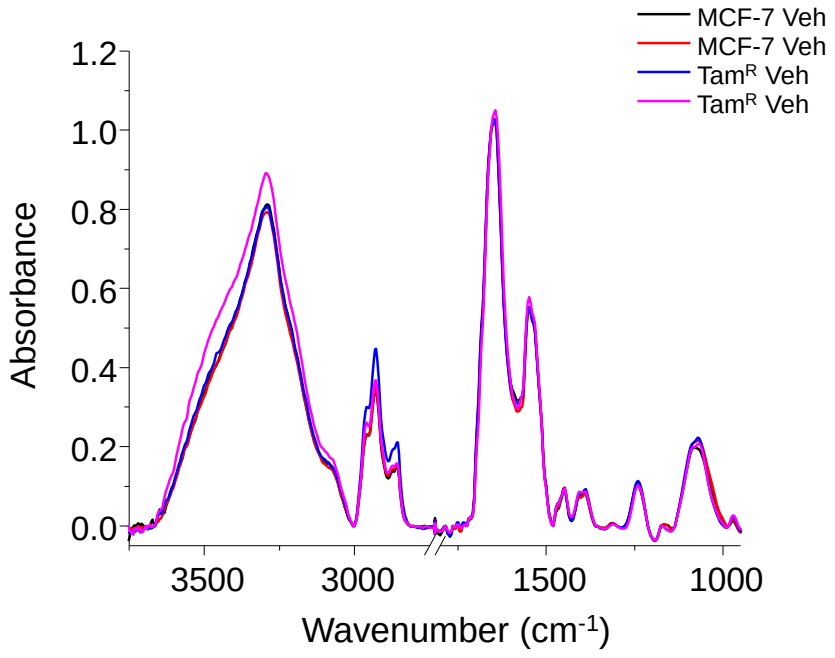


**Figure 4.14: MCF-7 and Tam$^R$ have unique spectroscopic signatures.**

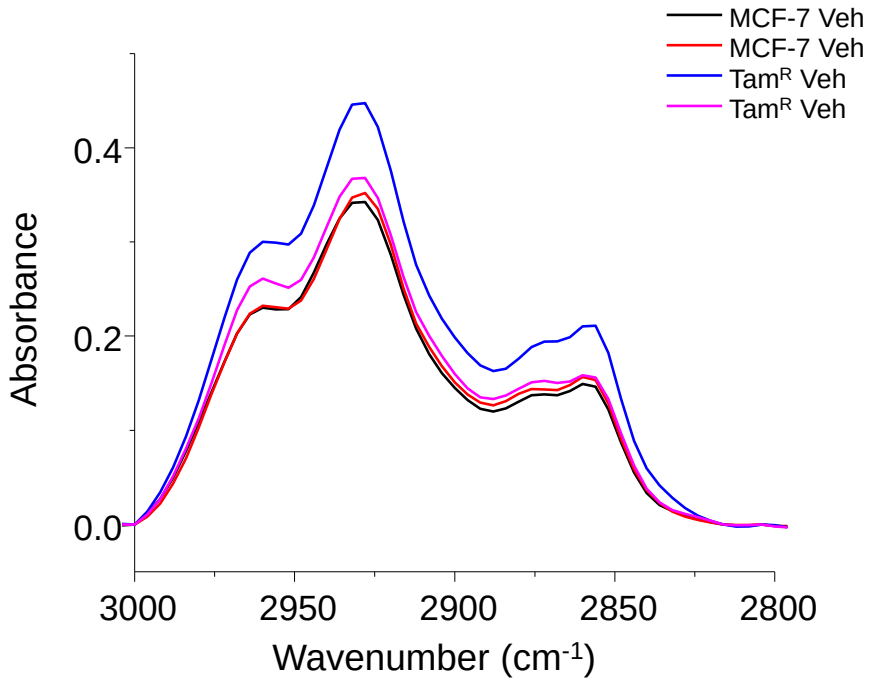


**Figure 4.15: C-H stretching region comparison of two MCF-7 samples and two Tam$^R$ samples.**

Next, both MCF-7 and Tam$^R$ cells were treated with $10^{-8}$ M tamoxifen (Tam) for 24 hours. This is known to be antiproliferative to MCF-7 cells in 3D culture (44). Normalized spectra and second derivative spectra from the C-H stretching (left) and fingerprint (right) regions were compared across conditions (Figure 4.16). Two independent biological replicates are displayed. While the MCF-7 samples are very similar in the response to Tam treatment, the Tam$^R$ cells respond differently. Upon treatment with Tam, Tam$^R$ cells show reduced absorbance in the C-H stretching region and relatively little change in the fingerprint region. These results are inconclusive in studying the effects of tamoxifen resistance using FT-IR imaging.

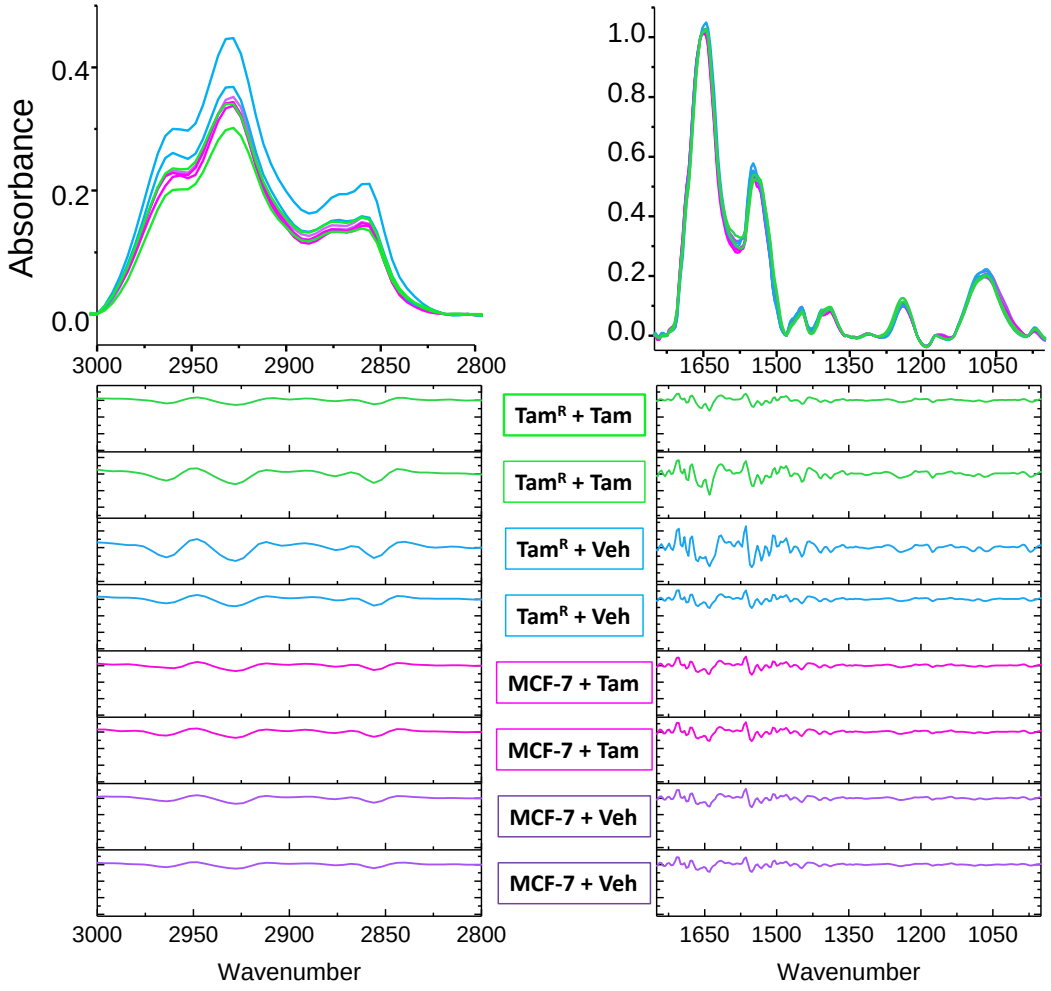


**Figure 4.16: Spectroscopic (top) and second derivative (bottom) analysis for C-H stretching and fingerprint spectral regions upon treatment with Vehicle (Veh) or Tamoxifen (Tam) in MCF-7 or Tam$^R$ cells.** Spectra from biological replicates are displayed.

Because we had previously shown that co-culture with HMF drastically alters spectroscopic signatures of breast cancer cells (37), we compared $Tam^R$ cells with and without co-culture using the same 3D model system. Briefly, $Tam^R$ cells were seeded at low density on Matrigel and grown for 6 days to form cancer spheroids. Normal primary human mammary fibroblasts were added on day 3 of culture for a total co-culture time of 3 days. The cells were in a 'mixed' type co-culture, and fibroblasts were localized to the edge of the spheroids. Co-cultures were grown in hormone-depleted medium as previously described (37). On the third day of co-culture, cells were treated with $10^{-8}$ M $E_2$, $10^{-8}$ M Tam, or vehicle control (ethanol). Cultures were fixed with 4% paraformaldehyde after 24 hours before paraffin embedding. Samples were imaged as described previously. We found that co-culture with HMF significantly impacts the spectral signatures of $Tam^R$ cells (Figure 4.17). Further, HMF alter the response of $Tam^R$ cells to treatment with $E_2$ or Tam. While the basal level of absorbance in peaks in the C-H stretching region is higher in co-cultured $Tam^R$, treatment with tamoxifen is enhanced by the presence of HMF. Not surprisingly, treatment with $E_2$ reduces the absorbance in these peaks. Changes in the fingerprint region are less substantial (Figure 4.18). These results give us an insight into how stromal cells may influence tamoxifen resistance, possibly even enhancing cancerous phenotypes upon treatment with Tam.

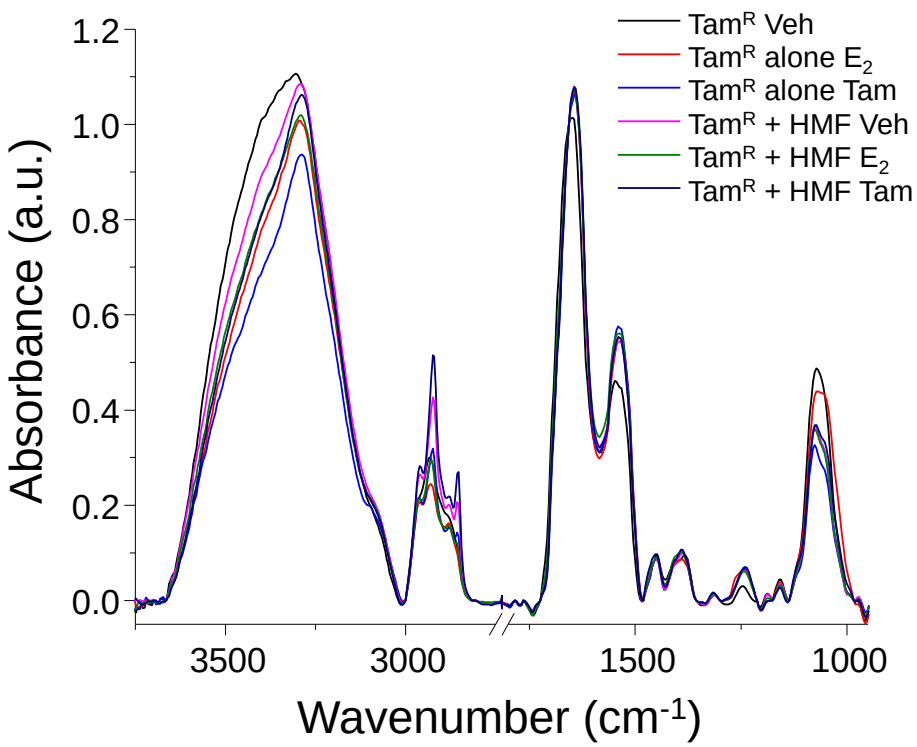


**Figure 4.17: Co-culture with HMF alters spectroscopic signatures of Tam$^R$ cells**. Profiles of cells before and after treatment are also changed upon co-culture.

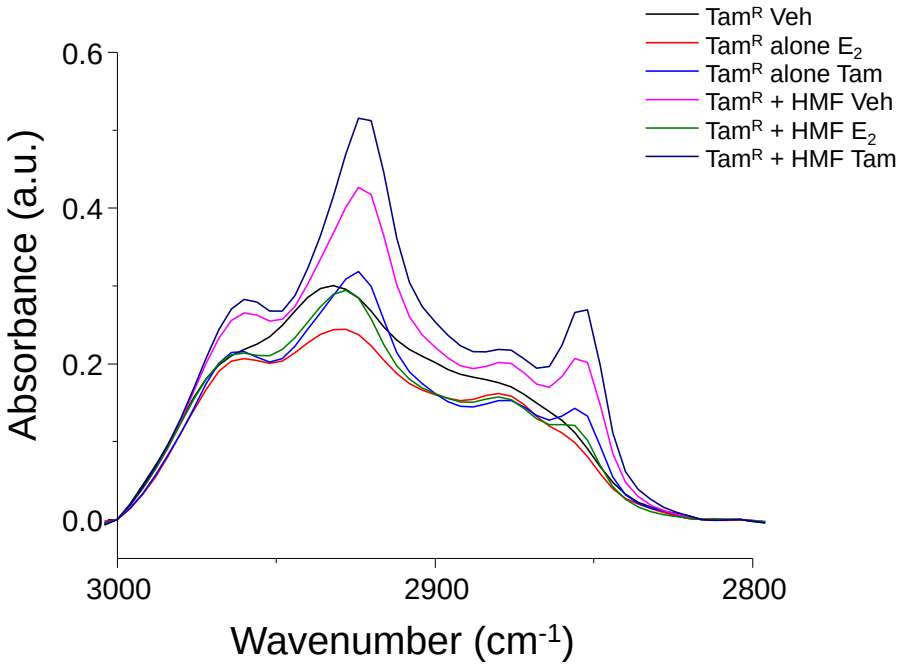


**Figure 4.18: Co-culture with HMF induces changes in the response of Tam$^R$ cells to $E_2$ and Tam in the C-H stretching region.**

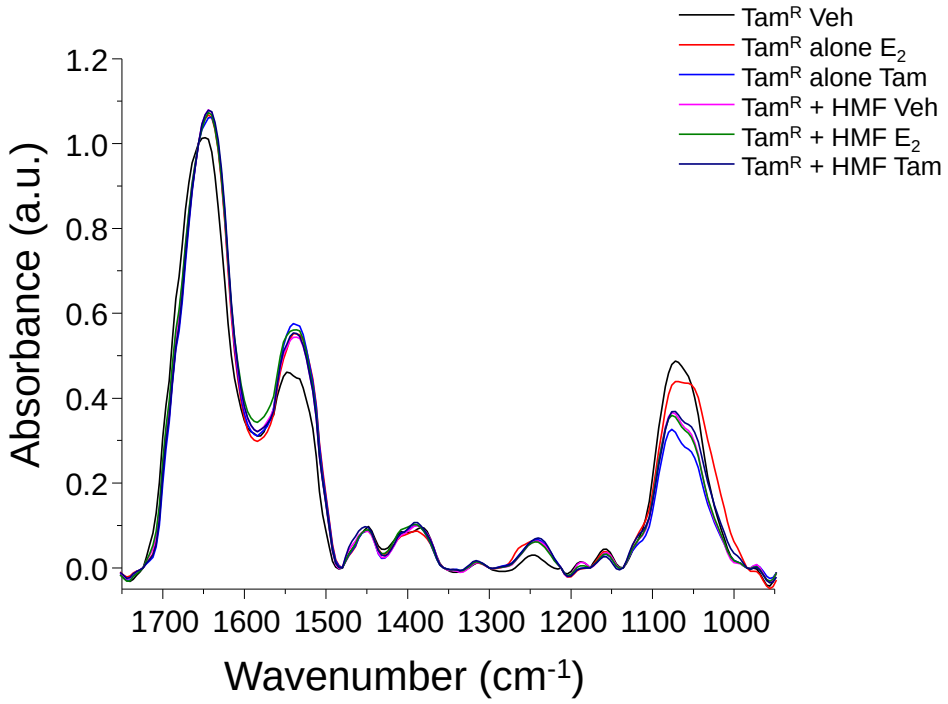


**Figure 4.19: Co-culture with HMF induces changes in the response of Tam$^R$ to $E_2$ and Tam in the fingerprint region.**

*Analysis of FT-IR images can be used to determine cellular heterogeneity within 3D spheroids*

It is understood that cells in tumors have heterogeneous phenotypes. Cells grown as spheroids in 3D culture are also heterogeneous, and it has recently been shown that even within the same spheroid there are phenotypic differences between cells (45). These principles have implications for the study of drug efficacy and treatment in patients, but they highlight the importance of using appropriate experimental models for initial drug studies. While cells grown in 3D as spheroids are more representative of cells in the human body than cells grown on tissue culture plastic, the kinetics of drug delivery are different. Cells will respond differently both as a function of their phenotypic expression and also the concentration of the drug that reaches the cell membrane. Both of these variables are dependent on the cell's location within the spheroid.

We have previously determined a spectroscopic signature of hormone response in MCF-7 spheroids. Next, we analyzed the IR images to determine which cells had the most robust response to treatment with $E_2$. While the cells on the outside of the spheroid should have the largest response, we wanted to map the signature across the diameter of the spheroid. This allowed us to determine the

penetration of $E_2$ into the cell mass and assess the phenotypic heterogeneity between MCF-7 cells grown in the same 3D culture conditions.

Images were first analyzed by drawing a series of boxes across the diameter of the spheroid, both lengthwise and widthwise. Each box had a length of 7.8 µm and contained 20 pixels for consistency. These boxes were labeled as regions of interest (ROIs) and average spectra were calculated for each box. Areas from either side of the spheroid were compared first (Figure 4.20 and 4.21). The spectra do not significantly change across the spheroid in either direction. In the center of the spheroid, the spectra do not change significantly (Figures 4.22 and 4.23).

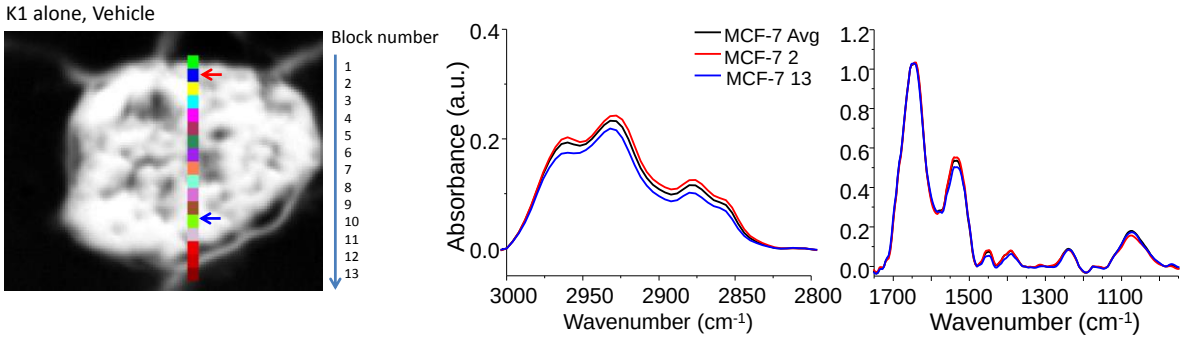


**Figure 4.20: Spectral changes across MCF-7 spheroid.**

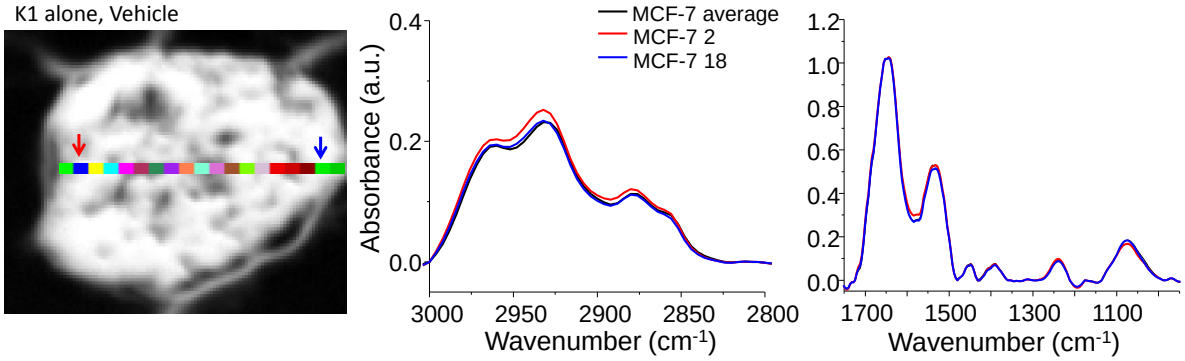


**Figure 4.21: Spectral changes across MCF-7 spheroid.**

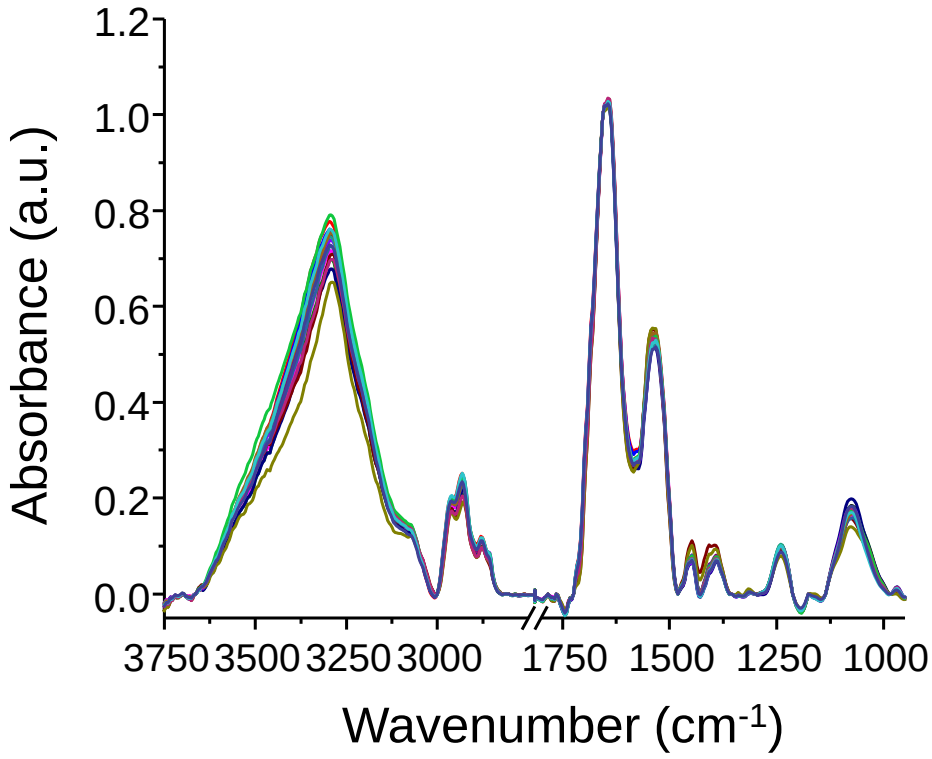


**Figure 4.22: Spectral changes within an MCF-7 spheroid.**

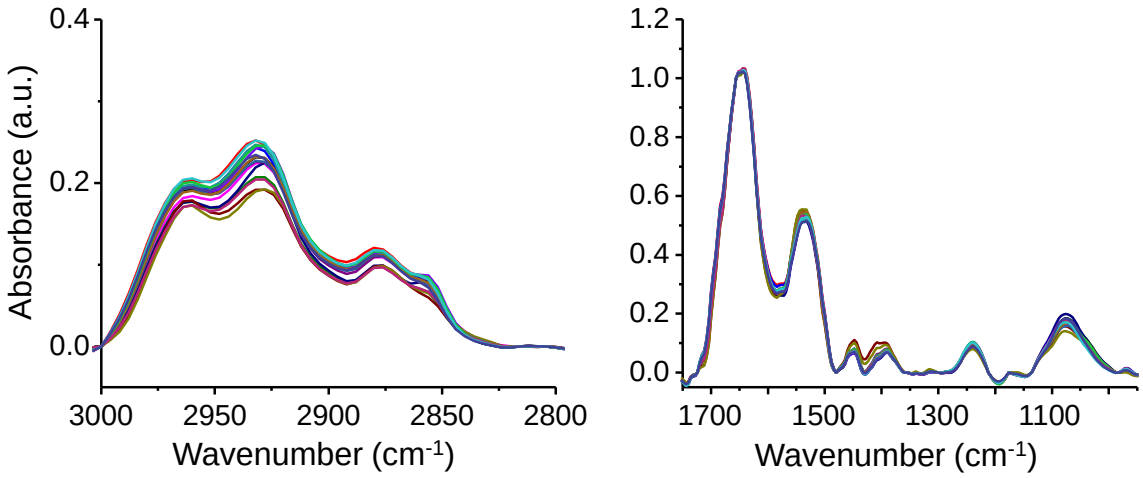


**Figure 4.23: There are very subtle spectral changes within MCF-7 spheroids.** In the very center of the spheroid (gold and crimson curves, left panel), there is a slight decrease in absorbance in the C-H stretching region.

While there are minimal differences across cells in a spheroid when treated with a vehicle control, treatment with $E_2$ elicits a significant increase in three prominent peaks found in the C-H stretching region (Figure 3.18). We hypothesized that the cells on the outside, being exposed to the highest concentration of $E_2$, should show the greatest response upon treatment. As shown in Figures 4.24 and 4.25, this is the case. Pixels from the outer region of the spheroid show increases in absorbance at 2960 $cm^{-1}$, 2930 $cm^{-1}$, and 2850 $cm^{-1}$. Surprisingly, this signature is lost at approximately 32 µm from the border of the spheroid (Figure 4.25). These results confirm cellular heterogeneity in response to $E_2$ in multicellular tumor-like spheroids.

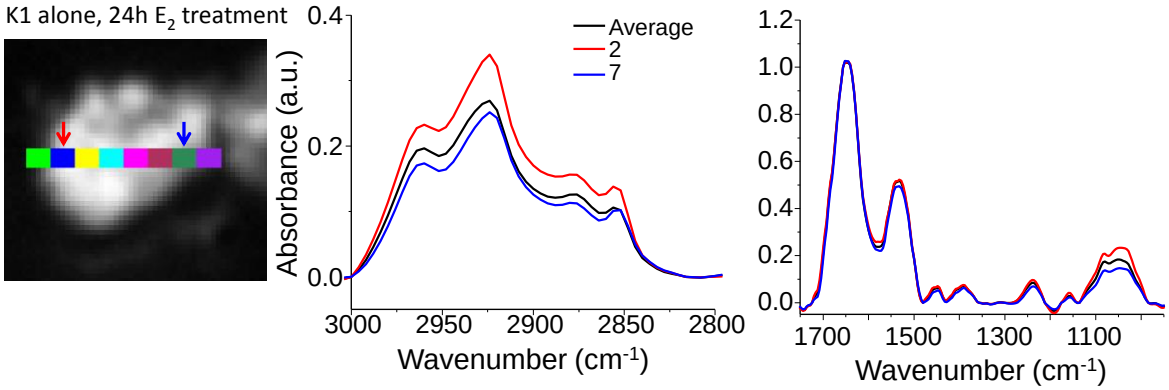


**Figure 4.24: Response of cells within an MCF-7 spheroid to $E_2$.** Comparison of cells from the border to the middle.

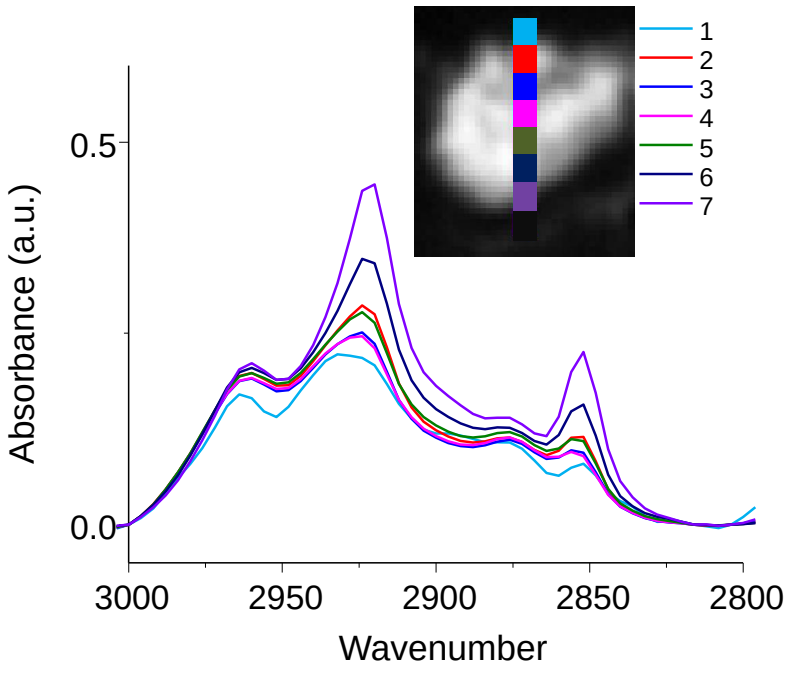


**Figure 4.25: Signature as a function of distance into the spheroid.**

The spectroscopic signature of hormone response is also diminished upon co-culture with human mammary fibroblasts. Fibroblasts secrete factors that downregulate ERα and switch the cells to hormone-independent growth (37). We used image analysis to determine whether all cells in the spheroid displayed this phenotype or if this was related to proximity to HMFs. We also aimed to determine how far the fibroblast influence extended into the spheroid. Surprisingly, we found that in the control, cells that were not in contact with fibroblasts had the same spectral signature as cells grown in monoculture (Figure 4.26). When MCF-7 were in contact with HMF, however, the spectral signature is lost. The effect of the fibroblasts was seen approximately 39 µm into the spheroid. These results confirm that fibroblasts are responsible for producing changes in the spectroscopic signature. Further, fibroblasts have a far-reaching and sustained effect on breast cancer spheroids. Upon treatment with $E_2$, the signature of response is lost when cells are in contact with HMF, and it is further diminished in the center of the spheroid (Figure 4.27). Taken together, these results show that FT-IR spectroscopic imaging can be used to determine drug delivery and efficacy in heterogeneous samples.

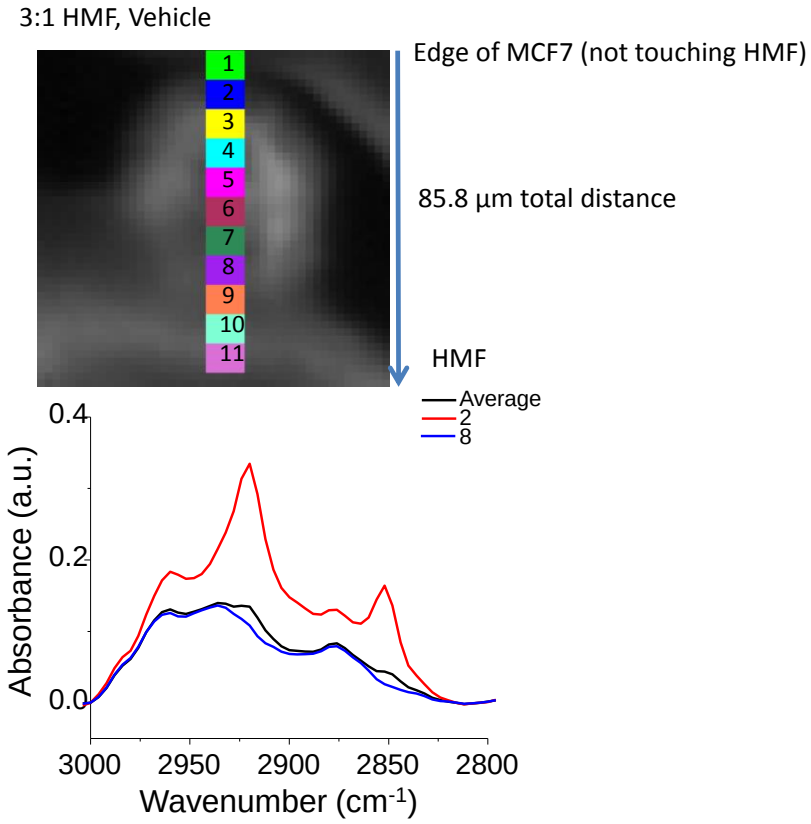


**Figure 4.26: Effect of fibroblast proximity on $E_2$ response across spheroid.**

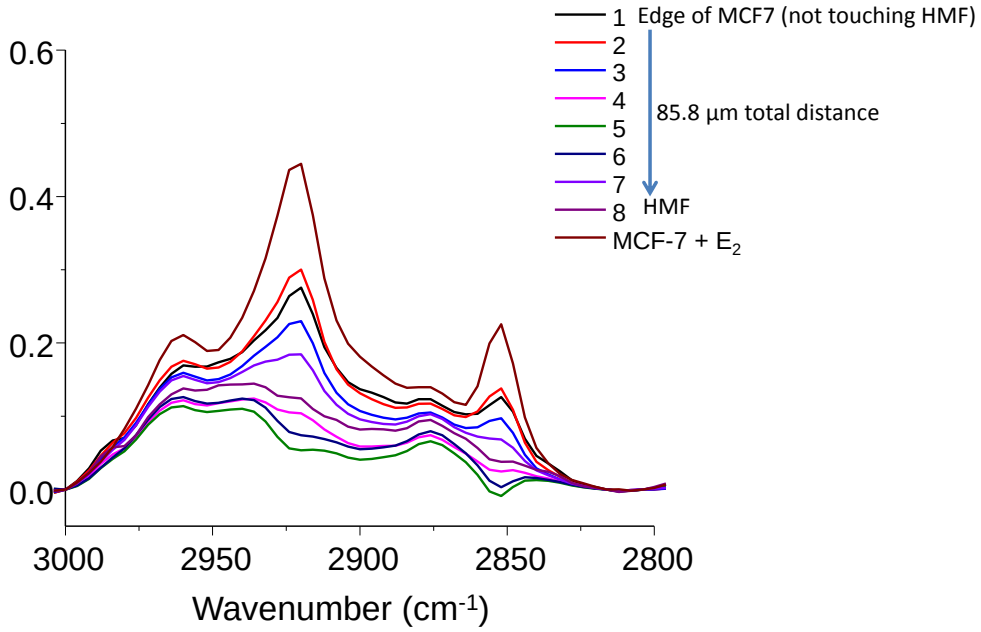


**Figure 4.27: The effect of fibroblasts extends approximately 39 µm into the cell spheroid, as measured by the response to treatment with $E_2$ as a function of distance.**

**Discussion**

We have shown that it is advantageous to use 3D models to study breast cancer cell phenotypes as disease progresses, how cell activities are altered by co-culture with fibroblasts or cancer-activated fibroblasts, and in response to hormone or therapies. Using a combination of FT-IR imaging and unbiased data analysis techniques, we have determined several spectroscopic signatures of cellular transformation.

Bayesian classifiers have been used by our lab and others to computationally segregate IR images of heterogeneous samples into pixels belonging to different 'classes'. This has enabled the development of a new field of digital pathology. Vibrational spectroscopy generates a large amount of information that can be used to train algorithms for the specific correlation of spectral signatures to cell types (13,19,22), the presence of histological markers (21), or disease states (10,11,20,23). Our group and others have shown that the state and dynamics of cellular transformations associated with cancer progression can be monitored using this technology (23,37,41). The use of classification and spectroscopic signatures is relatively unbiased and is less prone to the experimental error associated with using histologic stains. We showed that a Bayesian classifier could also distinguish between cells

and hydrogel constructs in a 3D cell culture model. The study of advanced cell culture models will benefit from an improved and unbiased method for analysis. As cultures become increasingly sophisticated with the addition of other cell types and additional extracellular matrix components, spectroscopic imaging can be used to identify contributions from these varied environmental factors.

While spectroscopic imaging generates very rich datasets and is highly sensitive to chemical changes, these benefits also create challenges in the analysis for biological understanding. Multivariate analysis or dimensional reduction techniques should be used to identify differences between and within samples. This is especially true for samples involving cells grown in *in vitro* systems. Cells are phenotypically diverse – both normal and cancerous cells are heterogeneous (12,45). Most molecular analyses are done in bulk; averages of the molecular contributions of hundreds or thousands of cells are taken. Imaging is the best way to identify heterogeneity across and between samples. We used two techniques to adjust for the sources of variance in IR images of biological specimens. First, we analyzed the second derivative of normalized average spectra of samples. Using the second derivative can aid in the identification of subtle changes in peak height or location (peak shift). Further, this can be used to identify small peaks that are overwhelmed by broader peaks with higher absorbance. We used second derivative spectra to analyze how tamoxifen resistant cells differ from other $ER^+$ breast cancer cells that are sensitive to tamoxifen. To further understand similarities and differences between samples, we used unsupervised hierarchical clustering of the second derivative. This technique can be used to determine how closely related two samples are, based on similarities in the spectroscopic signatures. We used it to determine the similarities between M1, M2, M3, and M4 cells grown in monolayer culture versus 3D culture. We found that M3 and M4 cells are less sensitive to their culture conditions with regard to their spectral signatures. M1 and M2 cells are phenotypically similar and while M2 are tumorigenic neither is invasive. Our results indicate that M2 may need an additional hit of a stiffened environment to display an invasive chemical signature.

Finally, analysis of IR images reveals that the distribution of chemical bonds within and across biological samples is varied and can be correlated with cellular phenotypes. When M1, M2, M3, and M4 cells were analyzed, an increased distribution of a peak associated with fatty acids/lipid metabolism was found at the edges of invasive cells. This trend increased as the cells became progressively more invasive. IR imaging has been used previously to monitor metabolically active cells, and we have correlated the spectroscopic signature of active metabolism with that of an enhanced cancerous

phenotype. IR images of spheroids were also analyzed to determine the heterogeneity across an individual spheroid of breast cancer cells. We found that hormone response in these cells was primarily found at the edges of the spheroids. Further, we found that fibroblasts affect the signature of hormone response and have a far-reaching effect on cells within the spheroid.

Our preliminary results have demonstrated the utility of FT-IR imaging in analysis of cancerous phenotypes in 2D and 3D cell culture. By combining classification schemes to perform an unbiased segregation of pixels in heterogeneous samples, multivariate analysis and dimensional reduction techniques, and rigorous image analysis, we have identified label-free spectroscopic signatures of phenotypes that correlate with disease progression and therapeutic resistance in human breast cancer cells. These studies highlight the need to use a combination of strategies for utilizing the rich datasets generated from FT-IR imaging in order to understand the molecular mechanisms driving cellular phenotypes in heterogeneous samples.

**Materials and methods**

*Cell Culture*

Cell culture protocols (maintenance in monolayer culture and assays in 3D culture) were done as described in Chapters 2 and 3. Additionally, the M1, M2, M3, and M4 cell lines are based on the MCF10A parental line (35). M1 and M2 are cultured the same as MCF10A, while the M3/M4 lines are grown in DMEM/F12 supplemented with 5% Horse Serum and 1% Pen/Strep without other additives. $Tam^R$ cells were grown as previously described (44).

*Sample Processing*

Cells grown as monolayers on MirrIR slides were fixed for one hour in 4% paraformaldehyde, washed twice in phosphate buffered saline (PBS), and then washed twice in sterile-filtered water twice to remove PBS. Samples were dried in a biosafety cabinet for at least 24 hours before imaging. Cells grown in 3D were processed as previously described. Briefly, samples were fixed in 4% paraformaldehyde, embedded in Histogel (Thermo Scientific), and then dehydrated and paraffin embedded. Samples were sectioned at 5 µm onto MirrIR slides for FT-IR imaging. Prior to imaging, slides were deparaffinized by soaking in hexane for 24 hours with gentle stirring. After deparaffinization, slides were left to dry before imaging.

*FT-IR Imaging and Data Analysis*

All imaging for this study was done in the Attenuated Total Reflectance mode using a PerkinElmer Spotlight 400. This instrument was described previously. Several 150 µm x 150 µm regions were imaged on each sample at a spectral resolution of 8 $cm^{-1}$ with 16 co-additions with a pixel size of 1.56 µm x 1.56 µm and an interferometer speed of 1.0 cm/s. Background spectra were collected at a spectral resolution of 8 $cm^{-1}$ and 120 co-additions.

After background and ATR corrections were done on the instrument, data was processed further using the ENVI-IDL software and in-house functions developed by our lab. First, a minimum noise fraction (MNF) reduction technique was used to minimize sources of noise in the data (46). The Bayesian classifier was run on MNF-corrected data to identify cell pixels. Data were baseline corrected and then average spectra of the cells from each sample were calculated and exported. When images were analyzed for spectral differences across the sample, regions of interest were drawn and baseline-corrected/classified average spectra of individual regions were calculated and exported. Average spectra were normalized to the Amide I peak (1656 $cm^{-1}$) and plotted in Origin Pro 8.5 (OriginLab, Northampton, Massachusetts, USA). Second derivatives were calculated and plotted in Origin Pro. Matlab (MathWorks, Natick, Massachusetts, USA) was used for unsupervised hierarchical clustering of normalized second derivative spectra.

**References**


1. Radinsky R. (1995) Modulation of tumor cell gene expression and phenotype by the organ-specific metastatic environment. *Cancer and Metastasis Rev* **14**(4): 323-328.
2. Hemminki K., Lorenzo Bermejo J., and Försti A. (2006) The balance between heritable and environmental etiology of human disease. *Nat Rev Genet* **7**(12): 958-965.
3. Merlo L.M.F., *et al*. (2006) Cancer as an evolutionary and ecological process. *Nat Rev Cancer* **6**(12): 924-935.
4. Kenny P.A. and Bissell M.J. (2003) Tumor reversion: Correction of malignant behavior by microenvironmental cues. *Int J Cancer* **107**(5): 688-695.
5. MacDougall J.R. and Matrisian L.M. (1995) Contributions of tumor and stromal matrix metalloproteinases to tumor progression, invasion, and metastasis. *Cancer and Metastasis Rev* **14**(4): 351-362.

6. Keller M.D., *et al*. (2008) Detecting temporal and spatial effects of epithelial cancers with Raman spectroscopy. *Disease Markers* **25**(6): 323-337.
7. Provenzano P.P., *et al*. (2006) Collagen reorganization at the tumor-stromal interface facilitates local invasion. *BMC Med* **4**(1): 38.
8. Burke K., Tang P., and Brown E. (2013) Second harmonic generation reveals matrix alterations during breast tumor progression. *J Biomed Opt* **18**(3): 031106.
9. Nijssen A., *et al*. (2002) Discriminating basal cell carcinoma from its surrounding tissue by raman spectroscopy. *J Invest Dermatol* **119**(1): 64-69.
10. Argov S., *et al*. (2002) Diagnostic potential of Fourier-transform infrared microspectroscopy and advanced computational methods in colon cancer patients. *J Biomed Opt* **7**(2): 248-254.
11. Bhargava R. (2007) Towards a practical Fourier transform infrared chemical imaging protocol for cancer histopathology. *Anal Bioanal Chem* **389**(4): 1155-1169.
12. Wood, L.D., *et al.* (2007) The genomic landscapes of human breast and colorectal cancers. *Science* **318**(5853): 1108-1113.
13. Tobin M.J., *et al*. (2004) Infrared microscopy of epithelial cancer cells in whole tissues and in tissue culture, using synchrotron radiation. *Faraday Discuss* **126**: 27-39.
14. Gazi E., *et al*. (2004) Fixation protocols for subcellular imaging by synchrotron-based Fourier transform infrared microspectroscopy. *Biopolymers* **77**(1): 18-30.
15. Susi H. and Byler D.M. (1986) Resolution-enhanced Fourier transform infrared spectroscopy of enzymes. *Methods Enzymol* **130**: 290-311.
16. Byler D.M. and Sushi H. (1986) Examination of the secondary structure of proteins by deconvolved FTIR spectra. *Biopolymers* **25**(3): 469-487.
17. Peticolas W.L. (1995) Raman spectroscopy of DNA and proteins. *Methods Enzymol* **246**: 389-416.
18. Wong P.T.T., Papavassiliou E.D., and Rigas B. (1991) Phosphodiester stretching bands in the infrared spectra of human tissues and cultured cells. *Appl Spectrosc* **45**(9): 1563-1567.
19. Jamin N., *et al*. (1998) Highly resolved chemical imaging of living cells by using synchrotron infrared microspectroscopy. *Proc Natl Acad Sci USA* **95**: 4837-4840.
20. Fernandez D.C., *et al.* (2005) Infrared spectroscopic imaging for histopathologic recognition. *Nat Biotechnol* **23**(4): 469-474.
21. Bhargava R., Fernandez D.C., Hewitt S.M., and Levin I.W. (2006) High throughput assessment of cells and tissues: Bayesian classification of spectral metrics from infrared vibrational spectroscopic imaging data. *Biochim Biophys Acta* **1758**: 830-845.

22. German M.J., *et al*. (2006) Infrared spectroscopy with multivariate analysis potentially facilitates the segregation of different types of prostate cell. *Biophys J* **90**(10): 3783-3795.
23. Bellisola G., *et al*. (2013) Rapid recognition of drug-resistance/sensitivity in leukemic cells by Fourier transform infrared microspectroscopy and unsupervised hierarchical cluster analysis. *Analyst* **138**(14): 3934-3945.
24. Orkin R.W., *et al.* (1977) A murine tumor producing a matrix of basement membrane. *J Exp Med* **145**: 204-220.
25. Timpl R., *et al.* (1979) Laminin—a glycoprotein from basement membrane. *J Biol Chem* **254:** 9933-9937.
26. Hassell J.R., *et al*. (1980) Isolation of a heparin sulfate-containing proteoglycan from basement membrane. *Proc Natl Acad Sci USA* **77**: 4494-4498.
27. Kleinman H.K., *et al*. (1982) Isolation and characterization of type IV procollagen, laminin, and heparin sulfate proteoglycan from the EHS sarcoma. *Biochemistry* **21**: 6188-6193.
28. Timpl R., *et al.* (1983) Nidogen: A new, self-aggregating basement membrane protein. *Eur J Biochem* **137**: 455-465.
29. Grant D.S., *et al*. (1985) The basement-membrane-like matrix of the mouse EHS tumor: II. Immunohistochemical quantitation of six of its components. *Am J Anat* **174**: 387-398.
30. Pinto M.P., Jacobsen B.M., and Horwitz K.B. (2011) An immunohistochemical method to study breast cancer cell subpopulations and their growth regulation by hormones in three-dimensional cultures. *Front Endocrinol (Lausanne)* **2**: 15-24.
31. Walsh M.J. Expanded Bayesian Classifier for automated breast histopathology. *Unpublished Data*.
32. Debnath J., Muthuswamy S.K., and Brugge J.S. (2003) Morphogenesis and oncogenesis of MCF-10A mammary epithelial acini grown in three-dimensional basement membrane cultures. *Methods* **30**(3): 256-268.
33. Muthuswamy S.K., Li, D., Lelièvre S., Bissell M.J., and Brugge J.S. (2001) ErbB2, but not ErbB1, reinitiates proliferation and induces luminal repopulation in epithelial acini. *Nat Cell Biol* **3**(9): 785-792.
34. Weaver V.M., *et al*. (1997) Reversion of the malignant phenotype of human breast cells in three-dimensional culture and in vivo by integrin blocking antibodies. *J Cell Biol* **137**(1): 231-245.
35. Santner S.J., *et al.* (2001) Malignant MCF10CA1 cell lines derived from premalignant human breast epithelial MCF10AT cells. *Breast Cancer Res Treat* **65**(2): 101-110.

36. Gazi E., *et al*. (2009) A FTIR microspectroscopic study of the uptake and metabolism of isotopically labeled fatty acids by metastatic prostate cancer. *Vib Spectrosc* **50**(1): 99-105.
37. Holton S.E., Bergamaschi A., Katzenellenbogen B.S., and Bhargava R. (2013) Integrating molecular profiling and chemical imaging to elucidate fibroblast-epithelial interactions and therapy resistance in breast cancer. *Submitted to Integrative Biology July 2013*.
38. Martin K.J., Patrick D.R., Bissell M.J., and Fournier M.V. (2008) Prognostic breast cancer signature identified from 3D culture model accurately predicts clinical outcome across independent datasets. *PLoS ONE* **3**(8): e2994.
39. Levental K.R., *et al*. (2009) Matrix crosslinking forces tumor progression by enhancing integrin signaling. *Cell* **139**(5): 891-906.
40. Schedin P. and Keely P.J. (2010) Mammary gland ECM remodeling, stiffness, and mechanosignaling in normal development and tumor progression. *Cold Spring Harb Perspect Biol* **3:** a003228.
41. Holton S.E., Walsh M.J., Kajdaçsy-Balla A., and Bhargava R. (2010) Label-free characterization of cancer-activated fibroblasts using infrared spectroscopic imaging. *Biophysical Journal* **101**(6): 1513-1521.
42. Collaborative EBCT. (1998) Tamoxifen for early breast cancer: an overview of the randomized trials. *Lancet* **351**(9114): 1451-1467.
43. Collaborative EBCT. (2005) Effects of chemotherapy and hormonal therapy for early breast cancer on recurrence and 15-year survival: an overview of the randomized trials. *Lancet* **365**(9472): 1687-1717.
44. Herman M.E. and Katzenellenbogen B.S. (1996) Response-specific antiestrogen resistance in a newly characterized MCF-7 human breast cancer cell line resulting from long-term exposure to trans-hydroxytamoxifen. *J Steroid Biochem Mol Biol* **59**: 121-134.
45. Smart C.E., *et al*. (2013) In vitro analysis of breast cancer cell line tumourspheres and primary human breast epithelia mammospheres demonstrates inter- and intrasphere heterogeneity. *PLoS One* **8**(6): e64388.
46. Reddy R.K. and Bhargava R. (2010) Accurate histopathology from low signal-to-noise ratio spectroscopic imaging data. *Analyst* **135**(11): 2818-2825.

# CHAPTER FIVE: A SPECTROSCOPIC SIGNATURE OF ERα PRESENCE, LOCALIZATION, AND FUNCTION IN BREAST CANCER CELLS


## Abstract

Estrogen receptor-α (ERα) is an important biomarker for the prognosis and therapeutic prediction of breast cancer. Patients who are ERα positive may benefit from targeted endocrine therapies. However, up to 30% of patients will become resistant to endocrine therapy within five years of treatment, while others fail to respond at all. The current gold standard for the detection of ERα is the use of immunohistochemistry to detect nuclear localization of the protein. While this describes the presence of the protein, it does not allow the pathologist to determine its function. This is a critical distinction to make with regards to choosing the appropriate therapeutic intervention. We recently reported that when breast cancer cells interact with mammary fibroblasts, ERα protein is downregulated and growth of the cancer cells becomes hormone-independent and resistant to the endocrine therapy tamoxifen. We also showed that a label-free imaging technique, Fourier transform infrared (FT-IR) spectroscopic imaging, can be used to monitor hormone response in 3D culture. Here, we expand on our previous results and describe a spectroscopic signature of ERα protein in MCF-7 cells through a knockdown study. Further, we also examine breast invasive ductal carcinoma biopsies with varying levels of ERα expression to monitor this signature in patient samples.

**Introduction**

Estrogen receptor breast cancers are the most commonly diagnosed cancers in the United States, with approximately 75% of the 232,340 new cases in the US being diagnosed as $ER^+$ each year (1). Presence of estrogen receptor alpha (ERα) was described as an important biomarker for the prediction of outcome and response to endocrine therapies over thirty years ago (2). Estradiol- and progesterone-receptor assays were used to assess the patient's receptor status on the basis of the interaction between radioactive-labeled hormone and the patient's tissue (3). It was not until the late 1990s that using immunohistochemistry to assess the patient's ER status became standard in pathology labs. It was reported in a large study that immunohistochemistry was superior to the ligand binding assay in terms of ease, safety, cost, and ability to predict response to adjuvant endocrine therapy (4). Use of immunohistochemistry to determine ERα status is the current gold standard in pathology.

While the use of immunohistochemistry to determine hormone status is significant for the prognosis and assignment of therapies for breast cancer, approximately 30% of patients who receive endocrine therapy will become resistant within five years, while others fail to respond at all (5-7). We have previously shown that the function of ERα is dynamic (Chapter 3 and Reference 8) and may still be present and identified using immunohistochemistry while its role in promoting tumor progression is minimized. We generated $ER^+$ breast cancer cells whose growth was controlled through a growth factor-mediated pathway. These cells were resistant to treatment with tamoxifen. Thus, it would be advantageous to develop an assay to determine a patient's receptor status that couples the localization of immunohistochemistry with a measurement of the receptor activity.

Recent reports have shown the efficacy of using PET-based challenges to determine ERα function *in vivo* (9,10). However, we aimed to develop a label-free microscopy-based method of determining ERα presence and function in human breast cancer cells and then paraffin-embedded (FFPE) human breast cancer tissue specimens due to the high spatial localization (on the order of micrometers) and ease of utility in the current clinical pathology workflow. Previously, we reported a signature of hormone response in MCF-7 breast cancer cells using Fourier transform infrared (FT-IR) spectroscopic imaging (Chapter 3). FT-IR is highly sensitive to chemical changes and has been used to determine label-free signatures of disease progression in cells (11-14) and tissues (15-17). Another benefit is the use of computational approaches to classify samples based on spectroscopic signatures (Discussed in Chapter 4). Thus, we propose the use of FT-IR to study estrogen receptor presence and

function because it is label-free, can monitor dynamics in protein function, and information can be used along with computational algorithms in the new field of digital pathology.

**Results**

*Establishing a gradient of ERα expression*

We aimed to determine a label-free spectroscopic signature of ERα expression. To obtain samples with a large range of ERα expression, a gradient was established. To do this, MCF-7 cells were transfected using an siRNA against the F domain of ERα (18). Because this is not a stable transfection, the siRNA will lose its effect as the cells begin to proliferate. Cells were transfected for 72 hours with siRNA and then the media was changed back to a hormone-depleted growth medium. Samples were harvested 24, 48, or 72 hours later. A sample was also taken immediately after knockdown (timepoint 0). A western blot was used to confirm knockdown (Figure 5.1).

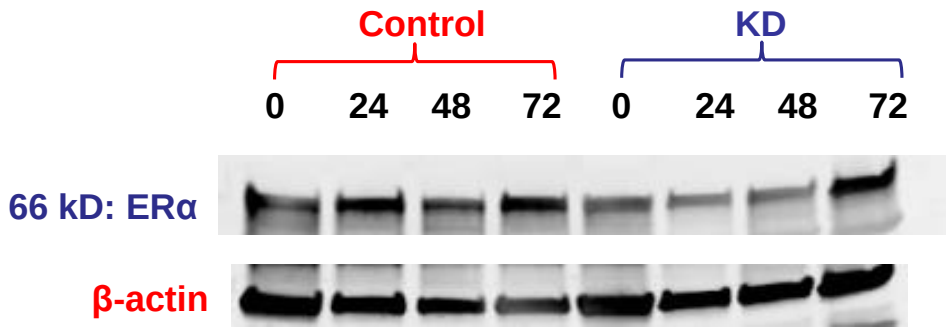


**Figure 5.1: A gradient of ERα expression is established after knockdown and recovery.**

IR spectra across each sample were averaged and compared for the control and knockdown samples (0h timepoint) first in order to establish a baseline of the presence of ERα in the IR spectrum. Upon knockdown, changes were induced across the spectrum and this was consistent for multiple independent biological replicates (Figure 5.2). Notably, absorbance of peaks in the C-H stretching region was reduced (Figure 5.3). We had previously shown that when ERα is downregulated in MCF-7 cells through the interaction with mammary fibroblasts; a loss in the hormone response signature was seen using FT-IR (Chapter 3). This signature was primarily seen in the C-H stretching region. Further, reduction in peaks associated with nucleic acids (Figure 5.4) was also observed, highlighting the role of ERα in providing a proliferative stimulus in MCF-7 cells.

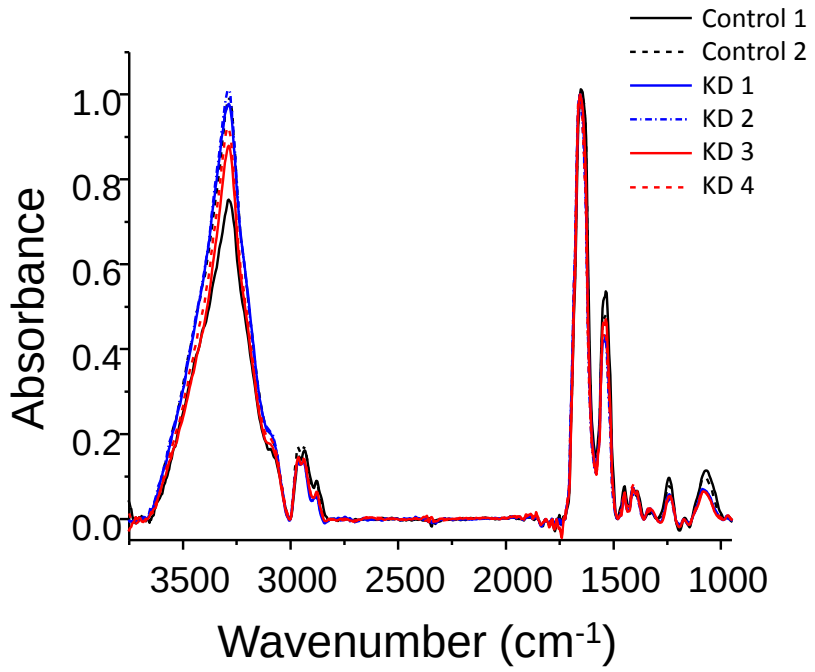


**Figure 5.2: Spectroscopic differences between control and knockdown samples.**

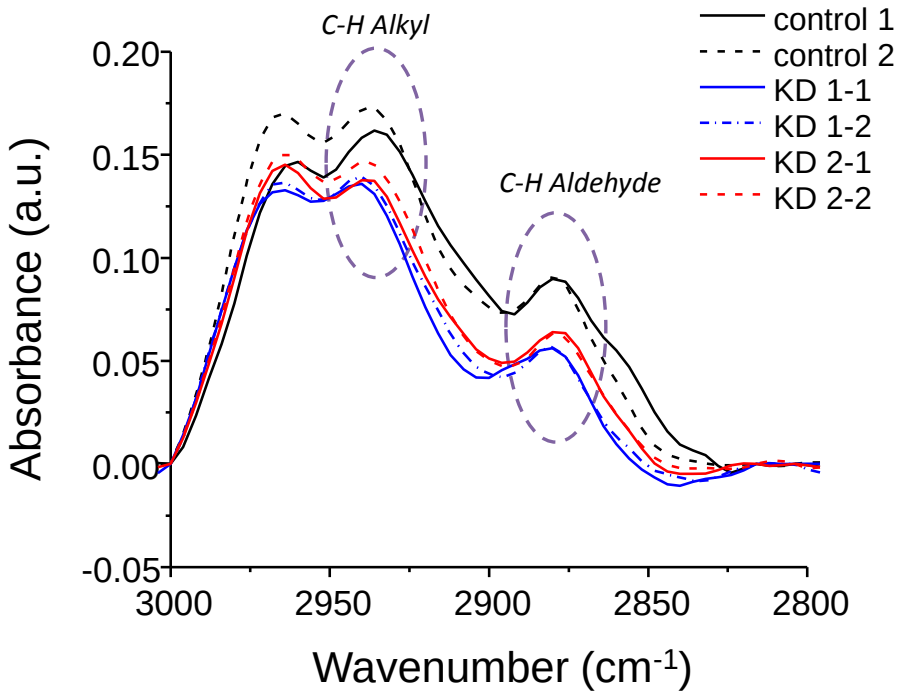


**Figure 5.3: Reduction in absorbance at peaks in the C-H stretching region was observed.** This is consistent with previous results (Chapter 3).

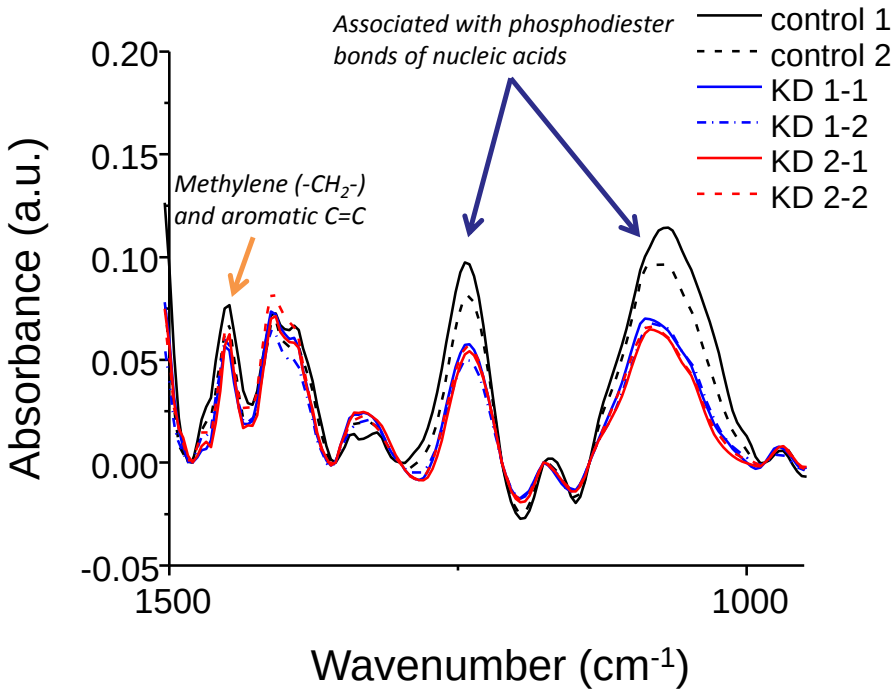


**Figure 5.4: Reduction in the absorbance of peaks associated with nucleic acids was observed after knockdown.**

*Identifying a label-free spectroscopic signature of nuclear ERα expression*

Upon treatment with estradiol ($E_2$), ERα is localized to the nucleus (Figure 5.5, Adapted from a study described in Chapter 3) (19). We aimed to strengthen the IR signature of ERα expression by monitoring it in its active form. The same knockdown gradient was repeated, but the samples were treated with either $E_2$ or a vehicle control (Veh) for 24 hours before fixation. We have previously used ATR FT-IR to discriminate between nuclear and cytoplasmic activity (11). In IR images of MCF-7 cells, the nucleus can be easily discerned using the symmetric phosphate stretching (1224 - 1236 $cm^{-1}$) peak associated with nucleic acids (Figure 5.6).

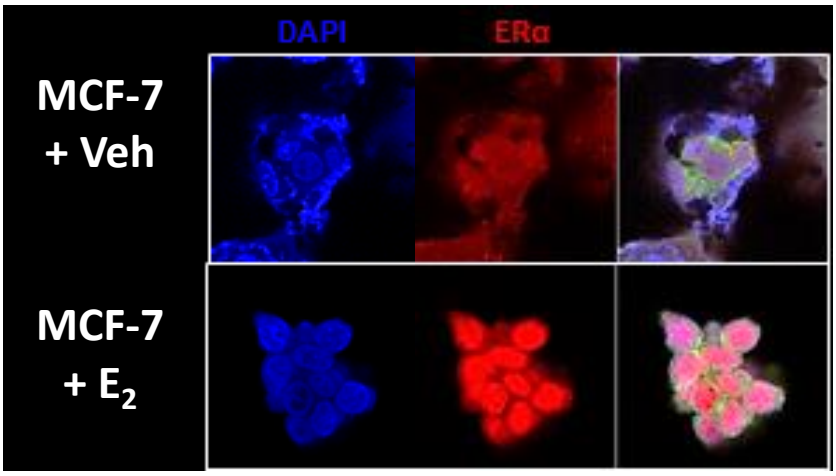


**Figure 5.5: ERα is localized to the nucleus upon treatment with $E_2$ in MCF-7 cells.**

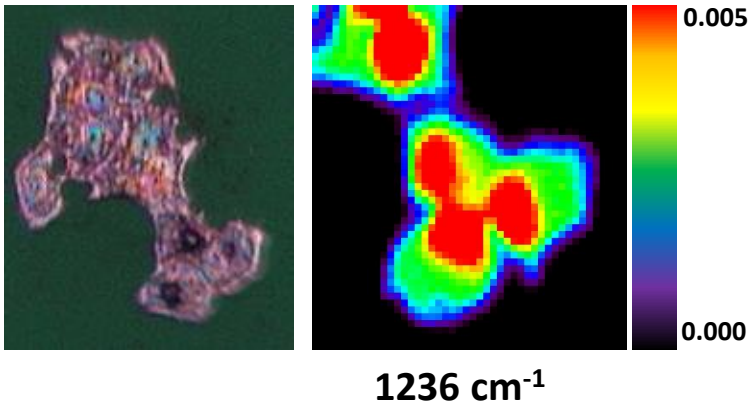


**Figure 5.6: The nucleus can easily be identified using the 1236 $cm^{-1}$ peak (symmetric phosphate stretching).**

First, images for the knockdown and control samples were analyzed to determine if the peaks used for normalization and labeling of the nucleus were altered upon stimulation with $E_2$. We found that the Amide I peak was unaffected by treatment in both control and knockdown samples (Figure 5.7). This confirmed our use of this peak for normalization, as absorbance would be uniform across the sample and between treatments. Then, the 1236 $cm^{-1}$ peak, used for labeling the nucleus, was analyzed. It is relatively unchanged in the control sample, but is affected in the knockdown sample (Figure 5.8). This result confirmed that we would be able to use IR to investigate spectroscopic signatures of ERα activity in the nucleus of MCF-7 cells.

Nuclear pixels were labeled by thresholding of the 1236 $cm^{-1}$ peak. While ATR measurements will include not only the nucleus but also the part of the cell that lies directly above it, the primary contribution to the spectra will come from the nucleus itself. Cell nuclei for each sample were analyzed individually in each condition. We confirmed that in the control samples, there is a signature of hormone response to $E_2$ treatment in peaks in the C-H stretching region (Figure 5.9, right) and in peaks associated with nucleic acids (Figure 5.9, left). This is similar to what we have previously reported (Chapter 3) and highlights the proliferative activities of $E_2$ on MCF-7 cells (20). However, in the samples that had ERα knocked down, this signature is lost and there is no clear distinction between $E_2$ and vehicle treatment (Figure 5.10). There are two cells with higher absorbance in the C-H stretching region (Figure 5.10, left), and this could be a result of the low knockdown efficiency. The overall trend in this region, however, is similar to what was seen in the bulk IR measurement (Figure 5.3). After 72h of recovery from knockdown, the signature has returned in the MCF-7 cells, due to the reestablished level of ERα at this time which was confirmed by western blot (Figure 5.1).

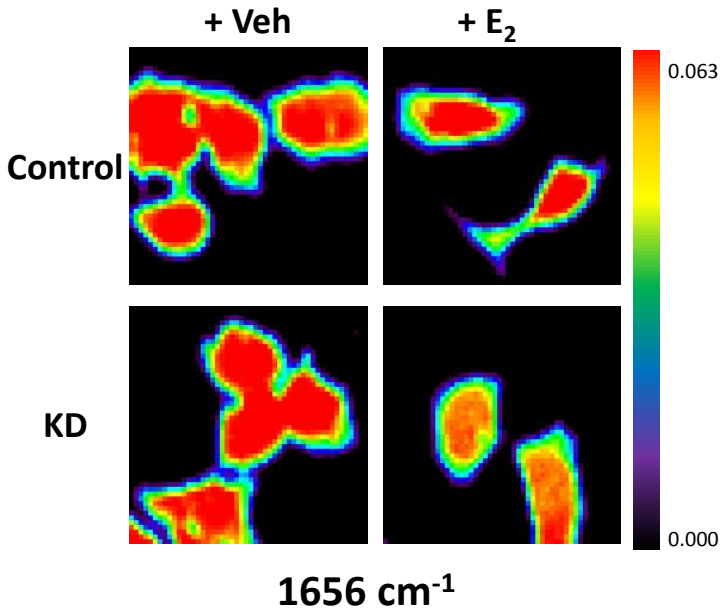


**Figure 5.7: The Amide I peak can be used to distinguish the cell body of MCF-7.** It is not affected by knockdown or treatment.

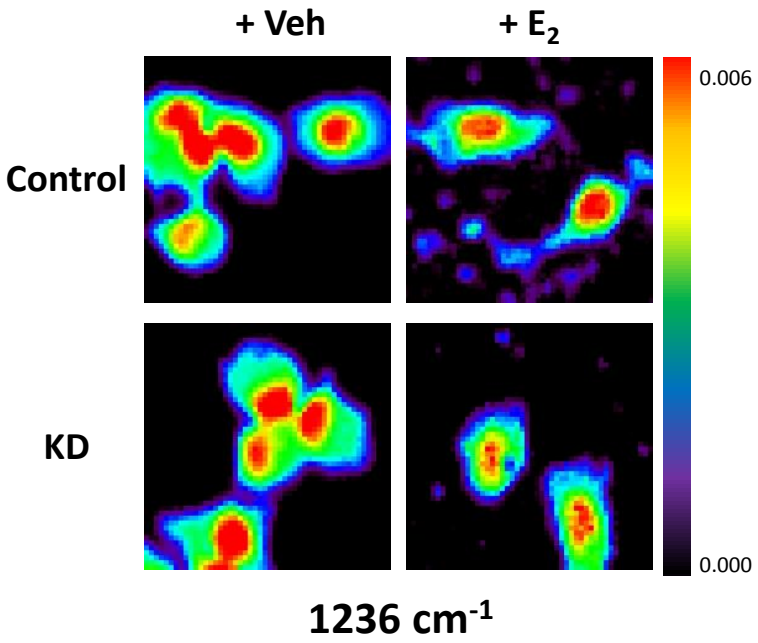


**Figure 5.8: The peak at 1236 $cm^{-1}$ is not affected by knockdown, but it is changed in cells treated with $E_2$.**

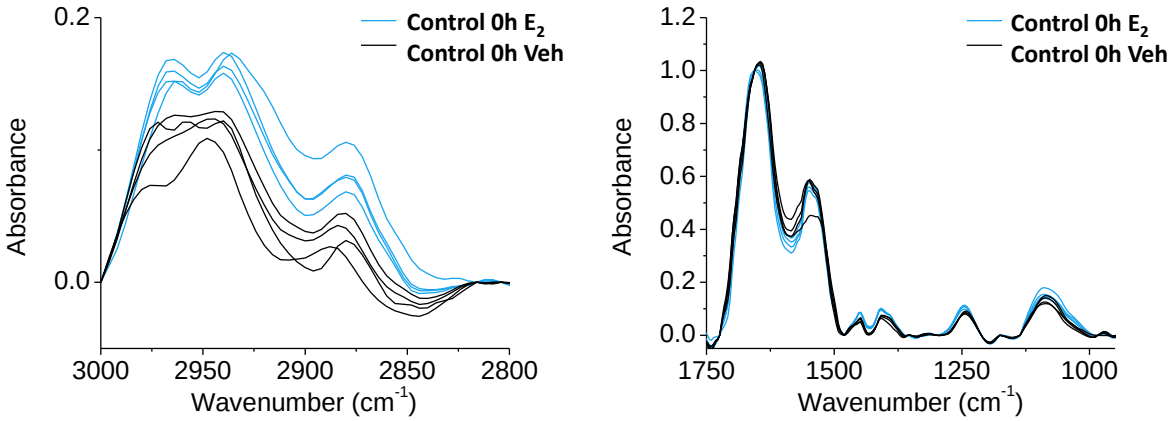


**Figure 5.9: In control samples, $E_2$ induces an increase in peak height in the C-H stretching region (right) and in peaks associated with nucleic acids (left) in the nucleus of MCF-7 cells.** These results confirm what we have previously reported.

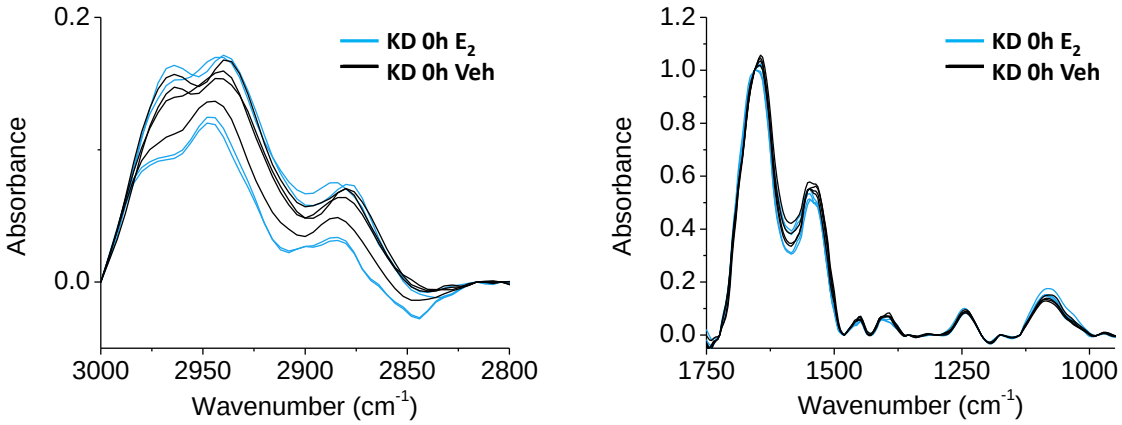


**Figure 5.10: In knockdown samples, however, there is no distinct separation of samples after $E_2$ stimulation.**

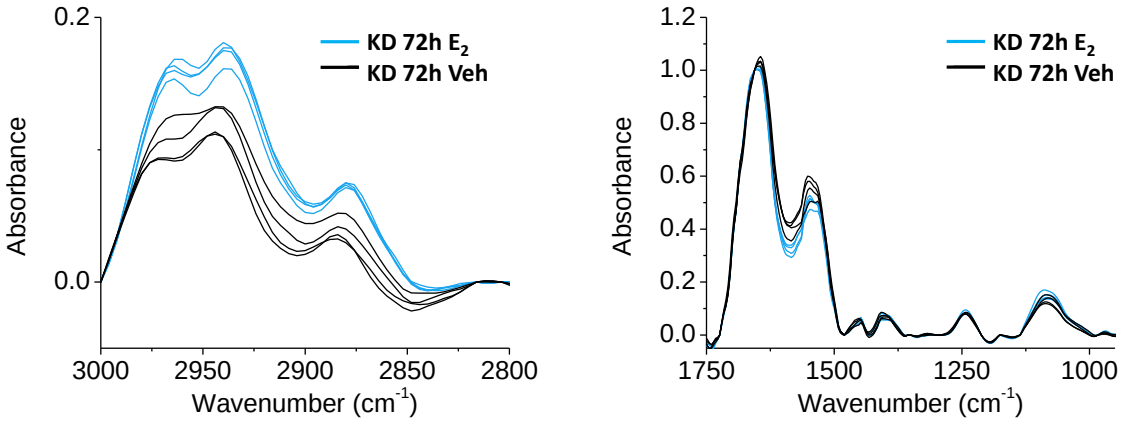


**Figure 5.11: After 72h of recovery from the knockdown, the signature has returned.**

*ERα expression correlates with IR data in patient samples*

Next, we wished to determine if there were differences in the spectra of breast tumor tissues with different levels of ERα expression. We chose twenty cores from patients with stage II/III invasive ductal carcinoma from a breast tissue microarray containing several different stages and levels of ERα expression (8,21). Ten cores were from patients with low (<20%) ERα expression and ten cores were from patients with high (<80%) ERα expression, as determined by immunohistochemical staining and the pathology report. Each set of ten cores came from 5 patients. Patient characteristics are summarized in Table 5.1. The cores were scanned as previously described in Chapter 3 and a Bayesian classifier was used to extract pixels from the epithelial cells only. When the spectra were compared for the cumulative average of each core set, only subtle differences were observed (Figures 5.12 and 5.13). There is a slight

increase in absorbance at the 1080 $cm^{-1}$ peak in cores with high ERα expression (Figure 5.14). Analysis of the second derivative spectra in the 1500 – 950 $cm^{-1}$ region reveals that there are more substantial differences than upon visual inspection of the raw averages, particularly in peaks associated with the methylene ($-CH_2-$) of fatty acids and aromatic C=C, perhaps indicating a snapshot of altered metabolism in these tissues.

While the results from the average across all ten samples were discouraging, upon inspection of the individual cores we observed striking heterogeneity between the samples (Figure 5.15). The tumors were matched for breast cancer subtype, grade, lymph node status, and receptor status to the best of our ability, all tumors were grade II or III and were not regionally invasive or metastatic (Table 5.1). Using IR, we detected significant changes in the global biochemical picture of the epithelial cells in these tissues. There is heterogeneity in all regions of the spectrum across cores and even between cores from the same patient (Figures 5.16 and 5.17). To determine if IR can detect any similarity between the tissues, the second derivative was taken for the average spectrum of each core and these data were subjected to an unsupervised clustering analysis (Figure 5.18). Samples were clustered using a correlation metric for both rows and columns and four patient clusters were observed. Surprisingly, not all cores from the same patient were clustered together (Low 1/2, Low 3/4, and High 9/10 were in different clusters). Samples Low 2 and Low 3 were clustered with cores expressing high ERα levels. The matched cores come from different regions of the same tumor, so this heterogeneity may be due to differences in the tissue characteristics in these cores. It is possible that one core captures a tumor margin while the other does not. The histology of these cores should be investigated further and another tissue dataset should be used to confirm these preliminary results.

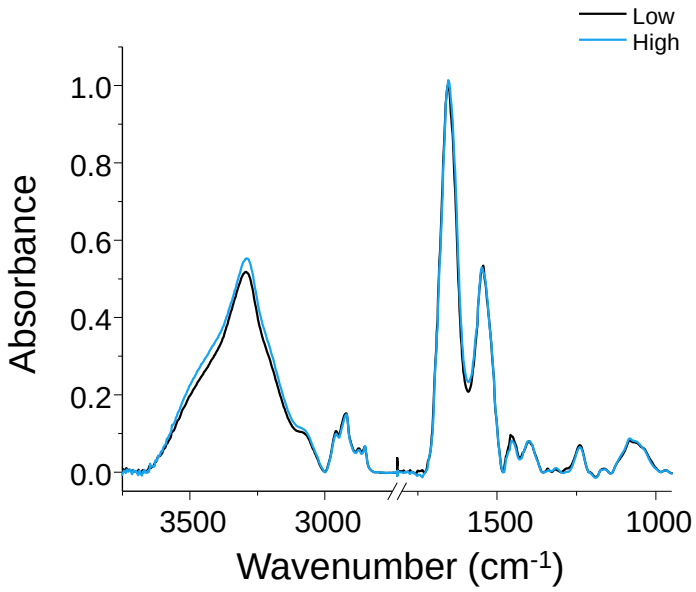


**Figure 5.12: Average spectra for 10 IDC cores with high ERα expression and 10 IDC cores with low ERα expression.** There is very little difference between the two sets.

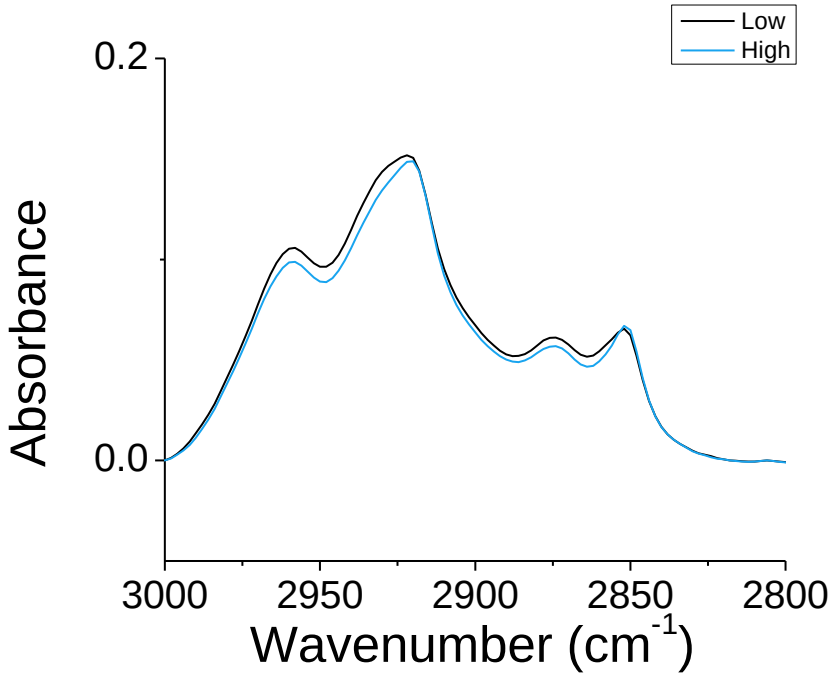


**Figure 5.13: In the C-H stretching region, there are peak shifts observed between high and low expression.**

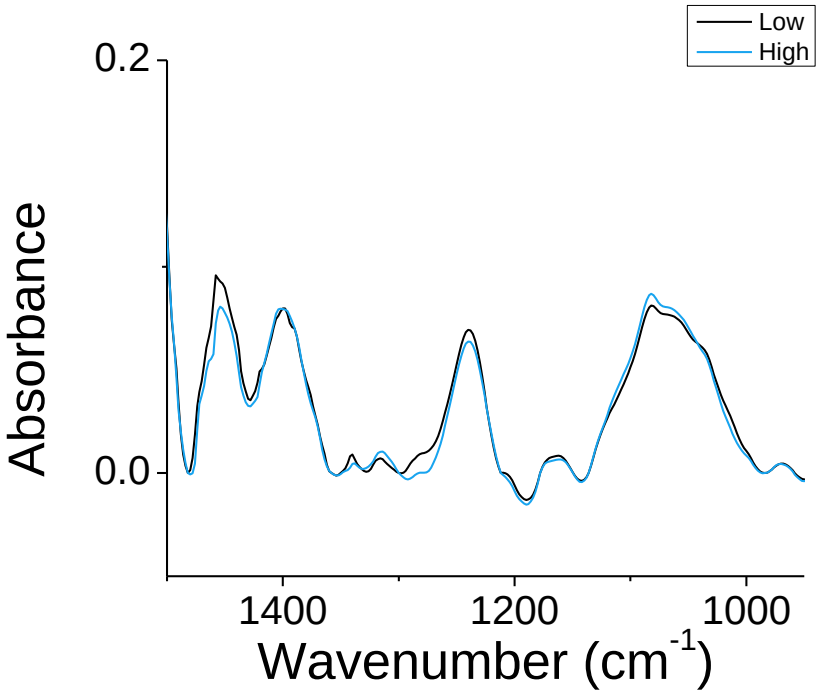


**Figure 5.14: The most apparent differences are in the peaks associated with nucleic acids as well as at 1450 $cm^{-1}$ (methylene $–CH_2-$ and aromatic C=C).**

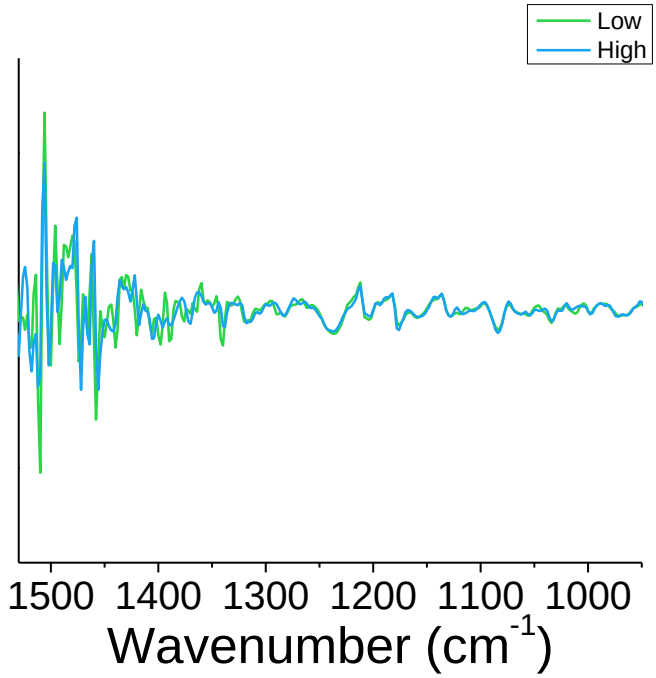


**Figure 5.15: Average second derivative spectra of the two classes reveals significant differences in the 1450, 1400, and 1350 $cm^{-1}$ peaks.**

**Table 5.1: Summary of patient characteristics.**

| Sample ID | Age | Grade | ER | PR | Her2 | TNM |
|---|---|---|---|---|---|---|
| Low 1/Low 2 | 59 | II/III | +, 5% | ++, 50% | borderline | T2N0M0 |
| Low 3/Low 4 | 40 | II | +, 5% | +, 5% | moderate | T2N0M0 |
| Low 5/Low 6 | 76 | II | ++, 5% | none | weak | T2N0M0 |
| Low 7/Low 8 | 39 | II/III | +, 5% | weak | positive | T2N0M0 |
| Low 9/Low 10 | 53 | II/III | ++, 15% | none | none | T3N0M0 |
| High 1/High 2 | 32 | II | ++~+++, 80% | ++, 50% | weak - moderate | T2N0M0 |
| High 3/High 4 | 48 | II/III | ++~+++, 80% | ++, 15% | moderate | T2N0M0 |
| High 5/High 6 | 53 | II | ++~+++, 80% | none | positive | T2N0M0 |
| High 7/High 8 | 70 | II | +++, 90% | ++~+++, 95% | weak | T2N0M0 |
| High 9/High 10 | 68 | II/III | ++~+++, 80% | none | none | T3N0M0 |

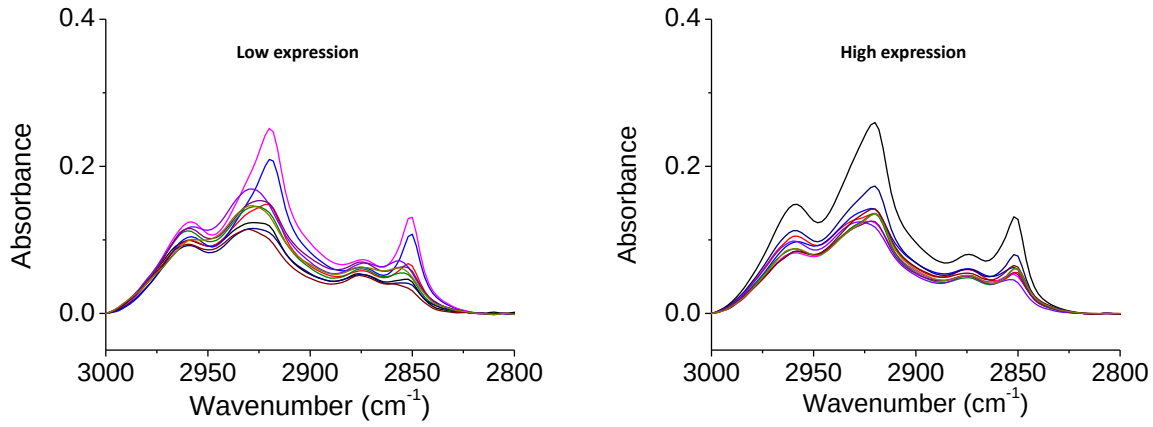


**Figure 5.16: There is a significant degree of variability even within the individual classes in the C-H stretching region.**

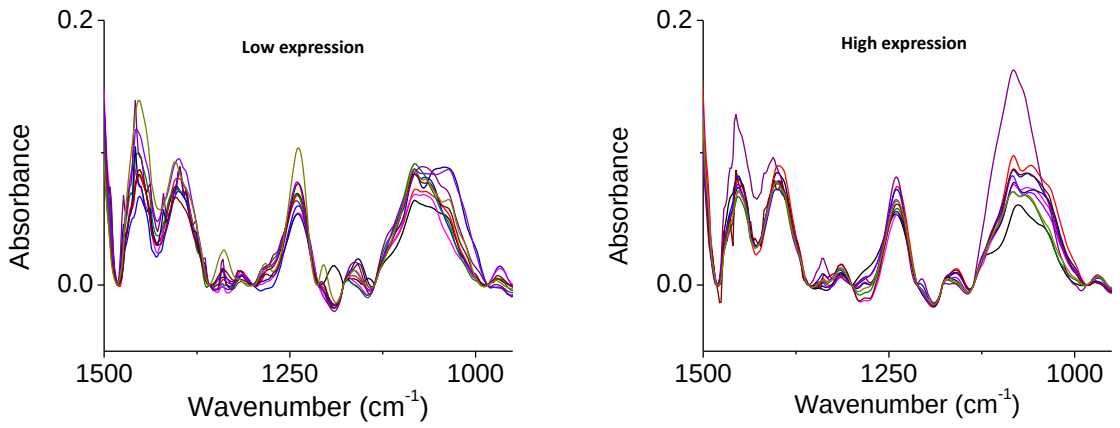


**Figure 5.17: There is a considerable degree of heterogeneity between samples.**

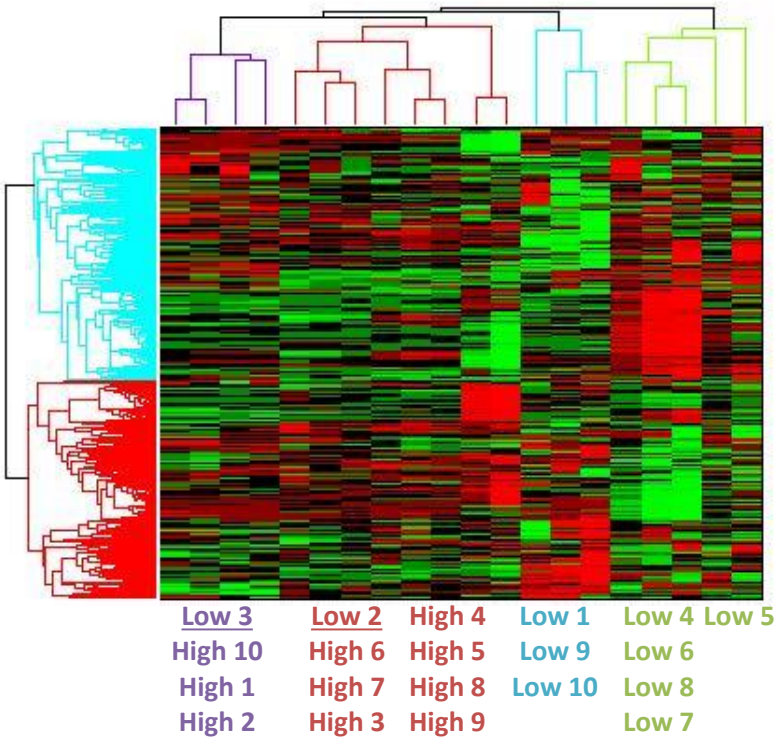


**Figure 5.18: Cluster analysis of the second derivative reveals four clusters of samples, with only two samples misclassified based on ERα expression.**

## Discussion

We aimed to develop a label-free chemical imaging based signature of ERα presence, localization, and function using FT-IR spectroscopic imaging. We used MCF-7 cells, a tumorigenic $ER^+$

human breast cancer cell line as a model system for this study. A recent report has used FT-IR to discriminate between $ER^+$ (MCF-7) and ER- (SKBR3) cell lines (22). However, we aimed to directly compare cells with differing levels of ERα from the same parental line. Thus, we compared wild-type MCF-7 with those that had been transfected with siRNA against the ERα protein. We also analyzed the spectra of human tumor biopsies expressing different levels of ER, as determined through immunohistochemistry.

We found that in bulk measurements, absorbance in the peaks of the C-H stretching region and in peaks associated with nucleic acids was decreased, confirming our previous results (Chapter 3). These results highlight the nature of ERα activity in $ER^+$ breast cancer cells. ERα promotes metabolic activity and proliferation; the anti-estrogen tamoxifen has been used to therapeutically block this activity (23,24). There are challenges associated with gleaning diagnostic information from bulk measurements, however. Any result obtained from these studies is the average of a collection of hundreds or thousands of cells. Cells endogenously express different levels of protein, and knockdown efficiency is not 100%. Hence, in this experiment we aimed to further describe a spectroscopic signature at the level of individual cells.

It is known that upon treatment with estradiol ($E_2$), ERα is translocated to the nucleus (19). Therefore, we used FT-IR image analysis to look for a signal of ERα in the nucleus of MCF-7 cells upon $E_2$ treatment. We compared these signals to MCF-7 that had been transfected with siRNA against ERα and then treated with $E_2$. We described a signature of ERα activity that is consistent with our previous result of the bulk knockdown measurements. Further, we find that after 72h of recovery from knockdown, the signature is restored. These observations confirm that this signature is the result of ERα activation and its downstream metabolic and proliferative effects.

While these findings from *in vitro* studies are important for understanding the correlations between expression of an active receptor and a label-free signature, $E_2$ challenges are not done with patients to determine hormone response. To move towards a diagnostically-relevant finding, we examined the IR spectra of patient breast tumor samples. We compared tissues from patients with invasive ductal carcinoma with low ERα expression to those with high ERα expression. We found that when samples from patients were averaged, there were no apparent differences in raw absorbance spectra between the two groups; however, second derivative analysis revealed differences in several peaks in the 1500 – 1300 $cm^{-1}$ region. When samples were looked at individually, the spectra were very heterogeneous, even between samples from the same tumor. Samples were classified based on the

second derivative of normalized average spectra with fair concurrence to ERα expression level; only two samples were clustered outside of their hormone status classification. These results indicate that FT-IR image analysis can be used to detect heterogeneity that may not be apparent with histology and highlight the necessity for an expanded study of additional patients with treatment and outcome information.

In conclusion, we show that estrogen receptor-α, a potent biomarker and prognostic factor for the majority of breast cancers can be detected using FT-IR imaging. These exciting results demonstrate that FT-IR could be used to show the function of estrogen receptor in fixed samples as a complement to immunohistochemical staining in the future.

**Materials and Methods**

*Cell Culture*

MCF-7 were grown as previously described (25) in MEM (Signal-Aldrich Corp., St Louis, Missouri, USA) supplemented with 5% calf serum (HyClone, Logan, Utah, USA), 100 µg/ml penicillin/streptomycin (Invitrogen, Carlsbad, California), and 25 µg/ml gentamycin (Invitrogen). Cells were either grown in 10 cm tissue culture plates or directly on IR-transmissive $CaF_2$ windows (International Crystal Laboratories, Garfield, New Jersey) or IR-reflective MirrIR slides (Kevley Technologies, Chesterland, Ohio, USA). Cells were seeded in a hormone-depleted medium consisting of phenol red-free MEM containing 5% charcoal-dextran-treated calf serum. Cells were grown in this medium for five days prior to knockdown, and medium was changed on the second and fourth days of culture.

*Knockdown and Treatment*

Endogenous ERα was knocked down using an siRNA duplex against the F-domain of ERα as previously described (18). siRNA was transfected at a final concentration of 50 nM using the DharmaFECT transfection reagent (Dharmacon, Lafayette, Colorado, USA) as per the manufacturer's recommendations at 72h before ligand treatment. The siERα forward sequence is UCAUCGCAUUCCUUGCAAAdTdT and the reverse sequence is UUUGCAAGGAAUGCGAUGAdTdT. After 72h of knockdown, some samples were treated with ligand. To establish a gradient of ERα expression, the media was changed on the remaining samples and after 24, 48, or 72h of growth to re-establish ERα protein, these samples were treated with ligand. Cells were treated with 10 nM estradiol ($E_2$) or the same volume of ethanol (Veh) for 24 hours prior to fixation or protein isolation.

*Western Blot Analysis*

Whole-cell extracts were prepared using ChIP buffer (10 mM EDTA, 50 mM Tris buffer, 0.5% Empigen BB, and 1% SDS) supplemented with 1 x complete protease inhibitor (Roche, Basel, Switzerland). Proteins were separated on a 4-20% SDS-PAGE gel and transferred to a nitrocellulose membrane. The primary antibody used was mouse anti-ERα (clone F-10, Santa Cruz Biotechnology, Dallas, Texas) diluted 1:100 in Odyssey blocking buffer (Li-Cor, Lincoln, Nebraska). The secondary antibodies used were goat anti-mouse 800CW (Li-Cor) and goat anti-mouse 680 IRDye (Li-Cor) at a dilution of 1:10,000 in Odyssey blocking buffer. Load control was mouse β-actin (Signa-Aldrich Corp).

*FT-IR imaging*

For cell fixation for IR imaging, the medium was removed and samples were washed three times in 1X PBS followed by washing three times in MilliQ water. Cells were fixed in 70% ethanol for 20 minutes. Samples were washed again 3 times in MilliQ water and then dried completely in a biosafety cabinet.

Imaging was done in ATR mode using a PerkinElmer Spotlight 400 FT-IR Imaging System as previously described (8). Briefly, three independent 150 µm x 150 µm regions of each sample were measured using 8 $cm^{-1}$ spectral resolution with 16 co-additions. A background was taken with 8 $cm^{-1}$ spectral resolution and 120 co-additions. The pixel size was approximately 1.56 µm x 1.56 µm. Images were atmospheric corrected and an ATR correction was done on the instrument. Data was processed using ENVI-IDL. First, a minimum noise fraction (MNF) reduction technique was used to minimize sources of noise. Then, the images were baseline corrected and regions of interest were drawn around each individual cell. Average spectra of the nuclei were taken by thresholding the 1236 $cm^{-1}$ peak.

*Breast cancer biopsy tissue*

A breast cancer microarray (BR961, US Biomax Inc., Rockville, Maryland, USA) containing normal, non-malignant, and invasive carcinoma samples with varying levels of ERα expression was mounted on an IR-transmissive $BaF_2$ window and imaged as previously described (8). The corresponding immunohistochemistry stained sections were marked for ERα expression by a pathologist and cores were divided into high expression (>80% of cells with nuclear ERα) or low expression (1-20% of cells with nuclear ERα). A Bayesian classifier was used to extract pixels from the epithelial cells only (21), and average spectra were taken of individual cores for comparison.

**References**


1. National Cancer Institute Breast Cancer Statistics 2013.
2. DeSombre E.R., *et al*. (1979) Steroid receptors in breast cancer. *N Engl J Med* **301**: 1011-1012.
3. Knight W.A.I., *et al*. (1977) Estrogen receptor as an independent prognostic factor for early recurrence in breast cancer. *Cancer Res* **37**: 4669-4671.
4. Harvey J.M., Clark G.M., Osborne C.K., and Allred D.C. (1999) Estrogen receptor status by immunohistochemistry is superior to the ligand-binding assay for predicting response to adjuvant endocrine therapy in breast cancer. *J Clin Oncol* **17**(5): 1474-1481.
5. Collaborative EBCT (1998) Tamoxifen for early breast cancer: an overview of the randomized trials. *Lancet* **351**(9114): 1451-1467.
6. Collaborative EBCT (2005) Effects of chemotherapy and hormonal therapy for early breast cancer on recurrence and 15-year survival: an overview of the randomized trials. *Lancet* **365**(9472): 1687-1717.
7. Gonzalez-Angulo A.M., Morales-Vasquez F., and Hortobagyi G.N. (2007) Overview of resistance to systemic therapy in patients with breast cancer. *Adv Exp Med Biol* **608**: 1-22.
8. Holton S.E., Bergamaschi A., Katzenellenbogen B.S., and Bhargava R. (2013) Integrating molecular profiling and chemical imaging to elucidate fibroblast-epithelial interactions and therapy resistance in breast cancer. *Submitted to Integrative Biology July 2013*.
9. Fowler A.M., *et al*. (2012) Small-animal PET of steroid hormone receptors predicts tumor response to endocrine therapy using a preclinical model of breast cancer. *J Nucl Med* **53**(7): 1119-1126.
10. Dehdashti F., *et al*. (2009) PET-based estradiol challenge as a predictive biomarker of response to endocrine therapy in women with estrogen-receptor-positive breast cancer. *Breast Cancer Res Treat* **113**(3): 509-517.
11. Holton S.E., Walsh M.J., and Bhargava R. (2011) Subcellular localization of early biochemical transformations in cancer-activated fibroblasts using infrared spectroscopic imaging. *Analyst* **136**: 2953-2958
12. Holton S.E., Walsh M.J., Kajdaçsy-Balla A., and Bhargava R. (2010) Label-free characterization of cancer-activated fibroblasts using infrared spectroscopic imaging. *Biophysical Journal* **101**(6): 1513-1521.
13. German M.J., *et al*. (2006) Infrared spectroscopy with multivariate analysis potentially facilitates the segregation of different types of prostate cell. *Biophys J* **90**(10): 3783-3795.

14. Bellisola G., *et al*. (2013) Rapid recognition of drug-resistance/sensitivity in leukemic cells by Fourier transform infrared microspectroscopy and unsupervised hierarchical cluster analysis. *Analyst* **138**: 3934-3945.
15. Argov S., *et al*. (2002) Diagnostic potential of Fourier-transform infrared microspectroscopy and advanced computational methods in colon cancer patients. *J Biomed Opt* **7**(2): 248-254.
16. Bhargava R. (2007) Towards a practical Fourier transform infrared chemical imaging protocol for cancer histopathology. *Anal Bioanal Chem* **389**(4): 1155-1169.
17. Fernandez D.C., *et al.* (2005) Infrared spectroscopic imaging for histopathologic recognition. *Nat Biotechnol* **23**(4): 469-474.
18. Chang E.C., *et al*. (2008) Estrogen receptors α and β as determinants of gene expression: Influence of ligand, dose, and chromatin binding. *Mol Endocrinol* **22**(5): 1032-1043.
19. Katzenellenbogen B.S. (1980) Dynamics of steroid hormone receptor action. *Ann Rev Physiol* **42**: 17-35.
20. Katzenellenbogen B.S., Kendra K.L., Norman M.J., and Berthois Y. (1987) Proliferation, hormonal responsiveness, and estrogen receptor content of MCF-7 human breast cancer cells grown in short-term and long-term absence of estrogens. *Cancer Res* **47**: 4355-4360.
21. Walsh M.J. and Bhargava R. Expanded Bayesian Classifier for automated breast histopathology. *Unpublished data*.
22. Büttner Mostaço-Guidolin L., *et al*. (2010) Molecular and chemical characterization by Fourier transform infrared spectroscopy of human breast cancer cells with estrogen receptor expressed and not expressed. *Spectroscopy* **24**(5): 501-510.
23. Heuson J.C. (1976) Current overview of EORTC clinical trials with tamoxifen. *Cancer Treatment Reports* **60**(10): 1463-1466.
24. Ward H.W.C. (1973) Anti-oestrogen therapy for breast cancer: A trial of tamoxifen at two dose levels. *Br Med J* **1**: 13-14.
25. Bergamaschi A. and Katzenellenbogen B.S. (2012) Tamoxifen downregulation of miR-451 increases 14-3-3ζ and promotes breast cancer cell survival and endocrine resistance. *Oncogene* **31**: 39-47.

## CHAPTER SIX: SUMMARY, IMPLICATIONS, AND FUTURE DIRECTIONS

We have demonstrated a new systems pathology approach for studying early breast cancer progression by combining three-dimensional cell culture models, molecular profiling, and chemical imaging. We investigated how fibroblasts affect breast cancer cell phenotypes, in particular the induction of an epithelial-to-mesenchymal transition (EMT) and hormone-independent/endocrine resistant growth. We characterized the soluble factors that govern cross-talk between cancer cells and fibroblasts using protein array profiling, and found that this secreted protein signature can be used to classify breast cancer patients based on the corresponding gene expression profile (iSig). Further, we have defined label-free chemical signatures of cellular transformations using Fourier transform infrared (FT-IR) spectroscopic imaging. Our approach incorporates the fields of cell biology, molecular biology, chemistry, and engineering with applications to medicine. These exciting results highlight the necessity for novel approaches in studying cancer progression, and we propose the use of emerging imaging technologies and proteomics to translate results from cell culture to patient samples for a more direct and lasting impact. To continue with the work discussed here, we will optimize our approach to continue the translational activities described herein.

*Future Directions*

This work has direct implications in the following areas:

1. Development of three-dimensional co-cultures for high throughput analysis and drug testing.

While we and others have demonstrated the utility of three-dimensional cell cultures for studying cancer phenotypes and mimicking human disease states, our work highlights the importance of including additional cell types. We have shown that fibroblasts significantly alter the activities and drug responsiveness of breast cancer cells. Additional cell types to add in the future for studying breast cancer are macrophages, myoepithelial cells, adipocytes, and lymphocytes. We propose to take the static cultures developed in this work and engineer environments to parallelize experiments. Two technologies that will enable this have recently been described for use in the cancer field. Microfluidic devices can be used to study living cells and run parallel experiments and assays on one device. Three-dimensional printers can be used to print hydrogels containing different cell types in any type of designed environment. These three-dimensional cultures and devices can be used to study cell-cell

interactions and also to screen small molecule libraries and test drugs. In the future, a patient's own cells could be printed in an environment that exactly recapitulates the patient's own histology and these constructs could be used for drug testing.

2. Using protein profiling for early prognostics.

We have shown that the interaction between cancer cells and fibroblasts can be characterized by the profile of secreted proteins. We took this signature and derived a corresponding gene signature, termed iSig. Using this approach, we were able to classify breast cancer patients based on their expression of iSig. An important next step in determining key factors that differentiate patients will be to use bioinformatics approaches to narrow down the signature from a 46-protein signature to a smaller subset of proteins. Gene set enrichment analysis (GSEA) is a tool used in bioinformatics for the assessment of gene signatures and how they relate to different populations using publicly-available microarray data. By performing hierarchical clustering of both the iSig and patients, we may be able to determine which genes/proteins may play a role in early disease progression. By identifying those early factors, we can design inhibitor studies to reverse the phenotype in cell culture for potential therapies. Perhaps more importantly, the proteins we identified are secreted and there is the potential for them to be detected in the bloodstream. There is the potential to prune the secreted protein signature and develop a biomarker or set of biomarkers to monitor disease status. A so-called liquid biopsy could be used to detect disease progression or treatment failure in patients. Eventually, a blood test could be developed as a screening tool based on the same principles.

3. Using FT-IR to determine breast cancer phenotypes and improve histology for modernized pathology.

FT-IR is a powerful imaging technique that can detect subtle chemical changes in heterogeneous samples. We identified a label-free spectroscopic signature associated with response to hormones and used this signature to translate results from cell culture to patient samples. In order to develop IR as a diagnostic tool, an expanded study should be done that correlates the information from an initial biopsy with treatment and outcome. An expanded study will determine whether IR imaging can be used to predict long-term endocrine sensitivity. This information could provide the pathologist with an additional layer of information and improve histology-based diagnosis and prognosis for cancer.